University of Trento
University of Brescia
University of Padova
University of Trieste
University of Udine
University IUAV of Venezia

Ph.D. Candidate:
Giordano Miori

LA MODELLAZIONE DI SISTEMI MECCANICI, APPLICAZIONI PER IL CONTROLLO E LA MISURA

MECHANICAL SYSTEM MODELLING, APPLICATIONS FOR MEASUREMENT AND CONTROL

Advisors:
Prof. Ing. Mariolino De Cecco
Prof. Ing. Lorenzo Battisti

March, 2011

UNIVERSITY OF TRENTO
Graduate School in Structural Engineering
Modelling, Preservation and Controls of Materials and Structures
XXIII Cycle

Ph.D. Program Head: Prof. D. Bigoni

Final Examination: 25th March 2011

Board of Examiners:
Prof. Roberto Oboe, Università degli Studi di Padova
Prof. Robert Mc Meeking, University of California
Prof. Ettore Penestrì, Università degli Studi di Roma Tor Vergata
Prof. Antonio De Simone, SISSA

To my friends, to me

and definitely to my family.

ACKNOWLEDGEMENTS

First, I would like to thank my tutor prof. Mariolino De Cecco for giving me the opportunity of this PhD and for teaching me the methods for problem solving. Then, I would like to thank Mario, once again, for always understanding and supporting me and for giving me the chances to follow my way, thank you kindly. I thank prof. Lorenzo Battisti for involving me in the interesting field of wind energy and for feeding and supervising my research activities in this field, thank you so much. A special thanks to prof. Filippo Trivellato who kindly help me in these last months of work, really thank you.

I would like to thank the DIMS of the University of Trento, in the persons who supported me and my activity and who taught me something.

I thank my all my colleagues, starting from the first year when Francesco Setti, Luca Baglivo and Giorgio Parzianello were the best team not only for scientific purposes. Then I thank who, in that years, were with me in the MeccaLab; especially Fabrizio Zendri, Matteo Grott and Omar Daud.

And finally a would like thank, one by one, my colleagues in turbomachinery Lab. who welcomed me two years ago teaching me day by day the secrets of wind energy. Thanks to Sergio Dell'Anna for all his work on the experimental test field, and naturally for his contributions on my research. I thank Luca Zanne for his special suggestions and Filippo Degasperi for his technical support. A special thanks to Alessandra Brighenti for hers constant and kindly support and for all the words spent with me. For all these people, once again, thank you for became my friends...

There are other people who I would like to thank, Roberto Fedrizzi, Salvatore Decarlo, Serena Negrente, Alan Schenal and Enrico Benini for their contribution on my research on wind energy. I thanks Pomini Tenova group for the activities on cylinder measurement.

This last raw are dedicated to my beautiful friends and to my family who always encouraged me and made me happy. Thank you Mamma & Papà. Thank you Linda. Thank you Aldo. Thank you Sebastian and, definitely, thank you Valerio.

SUMMARY

The research activity of this thesis deals with the modelling of mechanical systems and two applications are analyzed by means of the same approach to modelling process.

The first application is about the wind energy conversion systems. The modelling activity aimed at representing the behaviour of wind turbines operating in turbulent wind in terms of power conversion performances. The characterization of the test site has been thoroughly presented. Firstly, the concepts and the state of the art of both power curve and turbulence have been examined in detail. Secondly, a model based on a steady instantaneous power curve has been developed starting from the Reynolds approach at turbulence and a procedure to estimate the steady power curve from experimental data has been presented. The model proposed has been used on experimental data collected at the Trento test site to small wind turbines. Finally the model has been validated on experimental data through the comparison on energy capture forecasting.

The second application presented deals with the measurement of cylinder roundness by means of multi-point method. The purpose of the modelling activity was the representation of the measurement process of cylinders surface through multi sensor measurement systems. The model has been developed considering step by step the architecture of the measurement system. Firstly, the generic cylinder shape and axis has been modelled in a parametric way. Then the irregular motion during the measurement process has been modelled thanks to a few parameters and finally the sensor disposition and theirs error has been implemented in the model. The parametric model obtained has been used to demonstrate the importance of consider the positioning errors of the sensors and the motion of the cylinder in 3D domain. Finally a three point method for radius and motion reconstruction has been implemented in the model and same Monte Carlo simulation has been carried out to demonstrate the effect of 3D disturbances on shape reconstruction.

SOMMARIO

L'attività di ricerca di questa tesi riguarda la modellazione di sistemi meccanici. Con un approccio del tutto simile sono state modellate e studiate, in particolare, due diverse applicazioni.
La prima applicazione riguarda i sistemi di conversione dell'energia eolica. L'attività di modellazione è stata finalizzata alla modellazione del comportamento dell'aerogeneratore che opera in condizioni di vento turbolento in termini di prestazioni elettriche. Dopo un'attività preliminare di studio approfondito dello stato dell'arte, particolare attenzione è stata data ai concetti di curva di potenza e di turbolenza. In un secondo tempo è stato sviluppato un modello basato su una curva di potenza istantanea e stazionaria, partendo dall'approccio di Reynolds alla turbolenza. È inoltre stata implementata una procedura per stimare tale curva di potenza stazionaria da dati sperimentali. Infine, il modello proposto è stato validato con dati sperimentali raccolti nel sito di prova del Campo Eolico Sperimentale di Trento attraverso il confronto sulle previsioni di energia.

La seconda applicazione riguarda, invece, la misura della forma di cilindri. L'oggetto di questa modellazione è stato il sistema di misura della superficie del cilindro mediante sistemi multi sensore. Il modello è stato sviluppato considerando dell'architettura del sistema di misura. *In primis*, è stato sviluppato un modello parametrico in grado di simulare un cilindro generico. Dunque è stato modellato il moto del cilindro durante il processo di misura sempre avvalendosi dei principali parametri. Infine la disposizione dei sensori e i corrispondenti errori di posizionamento sono stati implementati. Il modello parametrico così ottenuto è stato sfruttato per dimostrare l'importanza di considerare gli errori di posizionamento dei sensori e il movimento del cilindro in 3D. Infine, è stato implementato il *Three Point Method* per la ricostruzione del raggio e sono state svolte alcune simulazioni Monte Carlo per dimostrare l'effetto degli aspetti modellati sulla ricostruzione della forma.

TABLE OF CONTENTS

1 Introduction ... - 1 -
  1.1 Thesis outline ... - 5 -
2 Power performance curves for wind turbines ... - 7 -
  2.1 The power curve of wind turbines ... - 7 -
  2.2 Standard power curve – The IEC guidelines ... - 13 -
  2.3 Influence factors in power performance tests ... - 16 -
3 The atmospheric wind ... - 27 -
  3.1 Wind in atmospheric boundary layer ... - 27 -
  3.2 Temporal variation of the wind speed ... - 29 -
  3.3 The turbulence ... - 30 -
  3.4 Turbulence spectra, length scale and coherence ... - 37 -
4 Wind turbines test site of Trento ... - 43 -
  4.1 Meteorological masts ... - 44 -
  4.2 Wind turbines ... - 47 -
  4.3 The wind regime on the test site ... - 49 -
  4.4 Spectral analysis on Trento test site ... - 55 -
5 Modelling the turbulence effect on power curves ... - 57 -
  5.1 Derivative Turbulence Correction Model – DTCm ... - 58 -
  5.2 Steady power curve estimation ... - 62 -
6 Experimental results ... - 67 -
  6.1 Standard power curve assessment at TN site ... - 68 -
  6.2 Turbulence modelling via DTCm at TN site ... - 73 -
7 Conclusions – part 1 ... - 83 -
8 Roundness measurement and shape reconstruction ... - 85 -
9 Parametric cylinder model ... - 88 -
  9.1 Surface and axis modelling ... - 89 -

10 Measurement system model - 95 -

10.1 Cylinder motion modelling - 95 -

10.2 Measurement system - 99 -

10.3 Measure computation - 102 -

11 Simulations of the measurement process - 105 -

11.1 Simulation 1: shape and axis deviation - 105 -

11.2 Simulation 2: support tool inclination - 107 -

11.3 Simulation 3: sensor’s position and alignment errors - 110 -

11.4 Simulation 4: irregular motion - 112 -

11.5 Simulation 5: complete simulation - 114 -

12 Multi-point reconstruction method - 117 -

12.1 Three point method - 117 -

13 Simulations of the measurement and reconstruction process - 123 -

13.1 Three point method simulations on the cross section – 2D - 123 -

13.2 Three point method on the cylinder simulations in 3D model - 133 -

14 Conclusions – part 2 - 141 -

15 Conclusions – general - 143 -

16 Bibliography - 144 -

1 INTRODUCTION

A physical system can be observed and studied in order to reach knowledge, as deep as possible, of the inner structure and of the behaviour of the system itself. For such a purpose, experiments and experimental devices was developed in the history of science trying to understand more and more sophisticated physical reality. When the information obtained through these experimental observations are collected and organized for advanced analysis, are developed into interpretation of the behaviour of the observed system then a model is produced. A clear and complete definition of a model can be found in (Avgoustinov, 2007):

"Model is a purpose-dependent, finite, simplified, but still adequate representation of whatever is modelled, allowing us to abstract from its unimportant properties and details and to concentrate only on the most specific and most important traits".

First of all a model is purpose-dependent, so to start modelling something, a purpose is necessary, a motivation. Simultaneously the confines of the "object to be modelled" have to be defined and hence the system has to be identified. Fortunately the system can be simplified, but how much can be simplified? The criteria is again dependent on the purpose and, obviously, on the complexity of the problem. As usual a compromise has to be reached; engineering applications are always aimed at achieving the best performance with limited resources. In order to accomplish this purpose the modelling activity has to follows an elementary sequence:

0. perceiving a need, a motivation, the purpose.
1. identifying the system to be modelled and its extension;
2. enumerating its essential traits, parts and properties;
3. localizing the problems and their formulations;
4. looking for available solutions, state of the art, previous approaches;
5. developing the model according to the purpose;
6. validating or verify the model;
7. and finally, use the model;

The use of the model is directly related to another key point, the aim of the model. Focusing the attention on mathematical and numerical models, they are suitable to simulate the behaviour of the investigated system in interesting condition. This is the case, for example, of weather forecasting where meteorological models are suited to foresee the behaviour of the atmosphere. The simulation of the behaviour of the system in particular condition (i.e. extreme loads, complex inputs conditions, operations far from nominal condition) can be of interest during the design process. Mathematical and numerical models are also suited for uncertainties estimation on measurement process/systems. In automatic control the mathematical model of the system to be controlled is essential to develop the controller. Many others utilization of mathematical and numerical models may be found because, obviously, the knowledge of the investigated system is fundamental to deal with it.

In the work discussed in this dissertation the application of the above explained sequence was strictly followed to model two different engineering research applications: the power curve of wind turbines operating in turbulent wind and the high precision measurement of cylinder roundness with multi-sensor systems. It is evident the great difference between these two applications but the modelling process is almost identical, and many points of contact can be easily found.

Starting from the point zero, the perceiving of a need, the reasons why these two modellation are carried out are explained. Please note that the cutting-edge aspect of the applications considered adds an important purpose that is the improvement of the knowledge, which is fundamental in research activities, on both turbulence effects on wind turbines power curves and uncertainties analysis on three-point measurement systems for cylinders.

Wind energy conversion in electrical energy by means of wind turbines has seen an exponential development due to the boost of green energy demand. In the recent years also the technology of these machines has seen great improvements which have brought to a continuous increment of wind power plant efficiency and reliability. At the same time the reduction of wind energy cost and effective policies attracted many investors leading to a wide diffusion of wind energy converters. The attractiveness of wind energy investments is obviously related to the productivity of electrical energy that depends both on the wind velocity present in the site and on the installed wind turbine. The power curve models the relationship between the power produced by the wind turbine and the reference wind velocity, hence, the accurate knowledge of the power curve is crucial to assess the energy production of wind turbines. Unfortunately, the power curve of wind turbines cannot be computed analytically because of the complexity of the whole system. Numerically simulated power curves can be used during the design process or for different architectures comparison but are not as accurate as required for energy production forecasting. For this reason the power curves of wind turbines are generally assessed by means of in field tests in which the wind speed and the power output of the turbine are collected. The presence of turbulent wind strongly influences the calculation of the power curves resulting in site-specific and not in machine-specific power curves. For these reason a model capable to capture the effect of the atmospheric turbulence on the power curves of wind turbines is of real concern. Moreover the understanding of the interaction turbine-turbulence allows investigating other aspects related to the infield measurement of wind turbine performances.

Particular attention has to be given to the diffusion of small size wind turbines. This class of wind turbine are frequently installed in industrial areas and at a low height from the ground and hence are more subjected to the turbulence effects.

Thinking about mechanical components, the most important fundamental form for engineering components is the circular cross-section and its extrusion, the cylindrical shape. The measurement of out-of-roundness of a mechanical part, usually referred to simply as roundness, is therefore an extremely important assessment (ISO/TS 12181-1:2003, 2003). The other important properties related to the circular and cylindrical shape are the cylindricity, the straightness of its axis (referred as axis deviation in what follow) and the concentricity and coaxiality of two features. These properties are rigorously defined in the (ISO 1101, 2004) along with the circular and total run-out that are fundamental for rotating parts. However the measurement of these properties is not so straightforward, or rather, not always. There are many applications like grinding machines for rolling mill cylinders, taper turning active spindle error compensation, high density recording media, to mention just a few, where the measurement is part of a control loop and therefore must be performed on-line. Finally, there are applications where the quasi-rotational motion of the cylindrical body is the main interesting object and the external shape is only a disturbance. For these applications, the component must be measured while rotating around an axis imposed by the motion system. The three-point method for roundness detection is commonly used to separate the influence of spindle axis motion in the cross section from shape circularity/roundness. It consists on an evolution of the calliper system that allow to measure simultaneously three radial displacement of the surface (instead of two) of, theoretically, the same cross section. One of its main requirements is also that each proximity sensor axis lies on the same cross section. Unfortunately this is not the case in reality. Cylinder's motion, shape, probes positioning have a general 3D structure.

This in turn can have a strong effect on the roundness estimation affecting its accuracy and therefore placing strong requirements of geometric precision to the whole mechanical setup. In order to assess the estimation accuracy, the error budget for the design or performance analysis a model of the whole measurement system considering 3D structure is necessary.

As a result the aim of both the application under investigation is a performance analysis. For the wind turbine this performance is regarded to the forecasting of the energy production of a WT placed in a site with a turbulence condition different than the ones registered during the power curve assessment. For cylinders measurement this performance is the reconstruction uncertainty of a three point method applied to a real measurement system that involves three dimensional effects.

1.1 Thesis outline

The thesis has been divided in two parts. The first parts concerns the modelling of the effect of the turbulence present in natural wind on the wind turbine power curves and the application of this model to experimental data from the Trento test site.
The second part is aimed at model the measurement process of the roundness of large cylinder by means of the three point method considering the real conformation of the system including irregular motion and sensor disturbances.

For both the applications, the identification of the system and its extension is carried out along with the preliminary analysis of the traits of the system:
In chapter 2 the power curve of wind turbines is defined and its particularity are outlined, then the standard procedure for the curve measurement is described and finally a list of aspects that affects the wind turbines power curve is reported and each factor of influence is discussed. In chapter 3 the characteristics of natural wind are treated and the turbulence is widely described along with the spectral analysis of the wind resource. Finally, in chapter 0 the test site for small wind turbines of Trento is described and the data regarding the resource are discussed.
In chapter 8 the problem of measuring the shape of rotating cylinders is investigated and the state of the art is explained. The architecture and traits of the three point method is also introduced.

Then the developments of the models are described:
In chapter 5 the turbulence effect on power curves is analytically described and then a procedure for estimating the parameters (steady power curve) from experimental data is reported.
In chapter 9 the parametric model of the cylinder surface and axis is explained and in chapter 0 the model of the whole measurement system that comprehends the motion sub-model and the sensors sub-model are developed considering the position and misalignment errors of the sensors.

Once the models are developed the validation, where possible, is carried out and the models are employed to fulfil the initial needs:
In chapter 6, the DTCmodel parameter estimation from the Trento site experimental data is reported, and then the validity of the model is checked by comparison on experimental data and on the energy forecasting.
In chapter 11 five simulation of the measurement process are carried out and discussed whereas in chapter 12 the three point method algorithm for radius and motion reconstruction is exposed and further developed. In chapter 0 simulation involving the measurement process model and the reconstruction algorithm are performed to show the effect of the position and alignment errors of the probes and the effect of irregular motion. Two campaign of Monte Carlo simulation (one in 2D and one in 3D) are carried out not only for performances estimation but also to demonstrate the suitability of the model in Monte Carlo simulation.

Finally the conclusions are drawn for both the applications and for the whole dissertation respectively in chapters [0 0 15].

2 POWER PERFORMANCE CURVES FOR WIND TURBINES

Wind energy is a significant and powerful resource and is safe, clean and abundant.

2.1 The power curve of wind turbines

In the field of fluid machines it is a common practice to synthesize by power curves the functional performances of the machinery. The power curve of a wind turbine relates the power output of the machine to the velocity of the wind speed that drives the rotor. The power output can either be the electrical power converted by the WECS or the mechanical power output. Usually, the electrical power fed in the grid is more relevant in wind energy applications because the whole system has to be analysed. In what follows we refer to power as the net active electrical power output, the same definition is found in the IEC guidelines for power performance measurement of wind turbines (IEC 61400-12-1, 2005).

The first difference between the classical machines (i.e. gas turbines, internal combustion engines, hydro turbines, etc...) power curves and the wind turbine power curve is the non-controllability of the input and its variability. In fact, only the smallest size wind turbines can be directly tested in wind tunnel, where the wind velocity and structure is controlled and the steady power curve can be assessed, without correction for tunnel blockage effects. Reduced scale model can be used in wind tunnel only when the size difference between the prototype and the real machine allows respecting the fluid dynamical similarity laws. Wind tunnel performance tests cannot represent the behaviour of the wind turbine in atmospheric wind (i.e. in real working situations). This fact gives the possibility to relate the power output with an homogeneous and stationary wind speed but preventing the observation of effects due to machine-atmospheric wind interaction. The steady power curve is the theoretical definition of power curve and it is not really useful without knowing how to correct it for atmospheric wind characteristics.

For these reasons, field tests are usually performed to evaluate the power curve of wind turbines. On the other hand, real conditions can be very complex involving various phenomena depending on the test site, and preventing the individuation of the univocal steady power curve of the WECS in real wind. Naturally, the understanding of the interaction between each phenomena and the turbine allows correction of the site-specific power curve to obtain the steady power curve or to asses another different site specific power curve. This work aims at a better understanding of the effect of atmospheric wind turbulence on the performance of wind turbines and to model these fundamental aspects, which are necessary to clarify some details on the wind speed measurement.

The representative wind speed is not easy to measure in nature. The representative velocity should be the free field velocity in the rotor plane that would be the "virtual" wind speed in the rotor plane without the machine. As it was evident in Figure 1 the turbine distorts the flow field, therefore the wind velocity in the rotor plane is not interesting as a reference in power curve measurement.

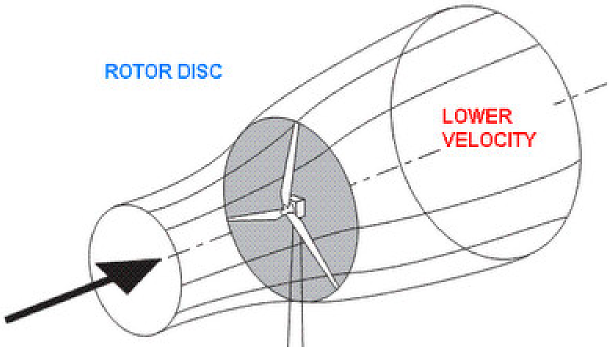

Figure 1: Energy extracting stream-tube of a wind turbine

In practice an upstream velocity is chosen as a good representation of this virtual velocity, leading to uncertainties related to the spatial and temporal non-homogeneity of the atmospheric wind field. Moreover, the wind speed is not constant over the rotor plane so it is necessary to define a "driving" wind speed that is some suitable average of the speed along the rotor axis over the rotor area. This driving wind speed is of course fictional but useful to understand the situation. In reality an anemometer is placed at a distance from the turbine and positioned in a manner that the measured wind speed *u* is a good representation of the driving wind speed *v*. The considerations on how representative this wind speed actually is for the wind speed that drives the rotor is a thorny issue that we discuss in chapter 5

The notion of a virtual wind speed that drive the rotor as the representative velocity for the power performance curve construction is related to the utilization of this curve for energy forecasting. In fact, the power curve above defined can be directly applied to wind speed data (or wind speed distribution) previously collected in wind resource measurement for a specific site giving a prevision of the energy productivity of the site.

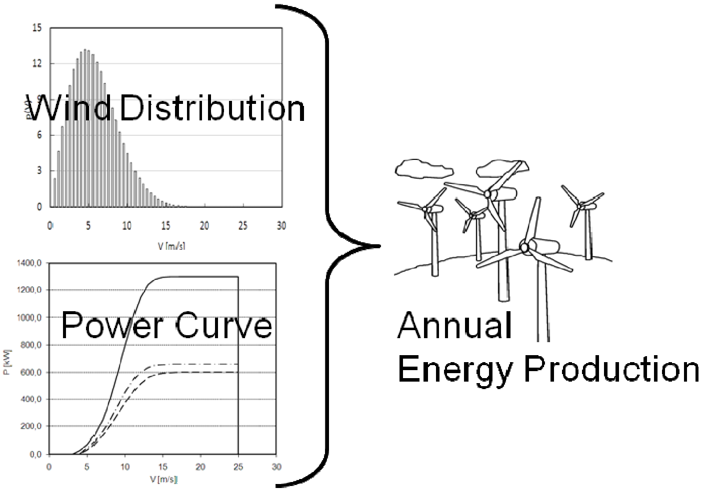

Figure 2: Annual energy production forecasting

The demand for accurate estimation of the energy production is directly related to the economic aspect of the wind turbine or wind farm project, therefore the commercial interest on accurate and site-adaptable power curve is high.

The power curve of the WECS is also a fundamental parameter to evaluate the effects of control strategies in unsteady wind on the performance during design process of the wind turbine. For the research on wind power conversion the power curve measurement and correction is always a challenging issue when effects of turbulence (Peinke et al., 2008) (Gottschall & Peinke, 2008), wind shear (Wharton & Lundquist, 2010), atmospheric stability and other site-specific aspects are investigated.

As depicted in Figure 3, three characteristic velocities are found in power curves: the cut-in wind speed, the rated wind speed and the cut-out wind speed. The cut-in wind speed, usually between 2.5 and 5 m/s for HAWT, is the minimum wind speed capable of producing energy. The starting behaviour of the machine depends on the architecture and the control strategy (D.Bianchi et al., 2006); some wind turbines need to be started by feeding power to the generator whereas others start rotating by themselves and when a certain rotating speed is reached the generator is connected.

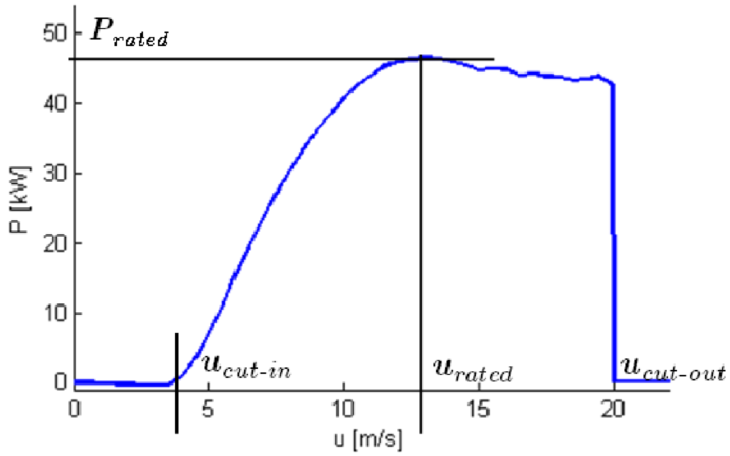

Figure 3: Power curve for stall regulated WT

The rated wind speed is the velocity by which the generator nominal or rated power is reached. Over this velocity the wind converter controls the power conversion in active or passive way. In passive-stall wind turbines the aerodynamics conditions on the blade profile over the rated speed determine a progressive stall that reduces the torque on the rotor. Active-pitch controlled wind turbines regulate the power conversion by rotating the blades around their longitudinal axis (i.e. pitching the blades) determining the stall (pitch to stall) or reducing the lift and consequently the torque at the rotor (pitch to feather). Other types of power control system would yaw the rotor with respect to the wind flow (furling) reducing both the efficiency and the swept area. At cut-out wind speed the rotor is slowed down to limit the structural loads on both the tower and the rotor avoiding structural damages.

The general shape of a wind turbine power curve is deduced from the relation:

$$P\left(u\right) = C_p\left(u\right)P_u\left(u\right) \text{ with } P_u\left(u\right) = \frac{1}{2}\rho_0 A_r u^3 \qquad [2.1.1]$$

where P_u is the power in the free wind passing with a speed u through the rotor area A_0 at a density ρ_0, and $P(u)$ is the extracted electrical power. The power coefficient C_P includes both the electro-mechanical behaviour of the WECS (e.g. control law, generator efficiency, etc…), aerodynamical effects (e.g. stall, sub-optimal conditions) and intrinsic physical limits.

The first physical limit for the maximum extractable power is known as the Betz limit:

$$Cp_{\max} = \frac{16}{27} \simeq 0.593 \qquad [2.1.2]$$

It was derived on the basis of the momentum theory on the actuator disc model of the wind turbine's rotor (Burton et al., 2002). Although it is based on a strongly simplified approach, the Betz limit is a widely used and accepted value. The power coefficients of modern commercial wind turbines are considerably below this theoretical limit and hardly reaching values of about 0.45. It is noted (see Figure 4) that the power coefficient is not constant over the whole range of wind speeds neither for active controlled nor for passive stall regulated wind turbine. This is due to the above mentioned effects (i.e. electro-mechanical behaviour and aero dynamical effects) that prevent the turbine to work at the maximum power coefficient at each wind speed. In variable speed WECS below the rated wind speed the control strategy regulates the generator velocity in order to follow the optimum power coefficient at each wind speed flattening the power coefficient curve.

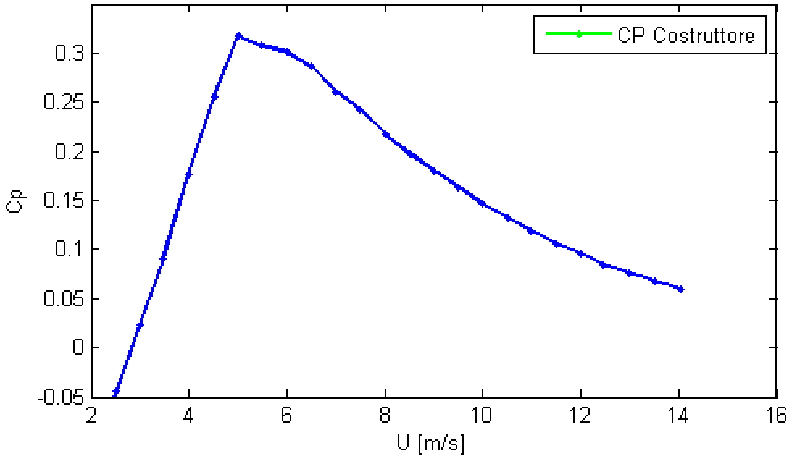

Figure 4: Example of power coefficient curve - fixed speed passive stall WT

Beside extracting as much energy as possible from the wind, the control objective for a WECS is to limit the generated power over the rated speed in order to avoid overloading under high wind conditions. In that region the power coefficient decreases rapidly with the wind speed.

2.2 **Standard power curve – The IEC guidelines**

Since the early 1980s, the need to provide uniform methodology ensuring consistency, accuracy and reproducibility in the measurement and analysis of the power performance of wind turbines, pushed several groups of experts to develop recommendations for defining the power performance of a wind turbine. Continuously developed, they were adopted in a guideline by the International Electrotechnical Commission (IEC) as the international standard IEC 61400-12 and the revised version IEC 61400-12-1 (IEC 61400-12-1, 2005).

Following these guidelines for power performance testing, the power performance characteristic of a wind turbine is defined by its measured power curve and the corresponding estimated annual energy production (AEP).

First of all the standard gives a detailed description of the necessary preparations for the performance test. This contains indications for wind mast positioning that is used to measure the wind speed and further meteorological parameters as the wind direction, the temperature, precipitation and air pressure. It also defines rules for the selection of the measurement sector, i.e. the range of wind directions that are considered to be valid for a representative measurement of wind speed. Thereby, wind directions that cause the mast to be in the wake of the turbine, are excluded.

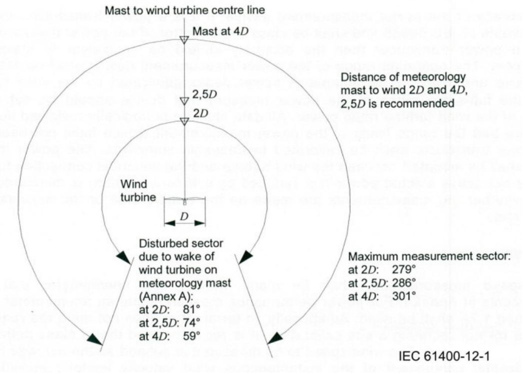

Figure 5: Disturbed sector due to WT wake on meteorology mast

An assessment of the terrain at the test site is described on the optional site calibration procedure that accounts for further significant obstacles in the test site. If a first investigation of the terrain yields that an enlarged site calibration is necessary, a table of flow correction factors is determined in an additional measurement and these factors are applied to the measured wind speed to reduce the effect of terrain complexities on the power curve measurement.

After the site preparation, the requirements for test equipment are listed along with data acquisition system specifications. In section 7 of the (IEC 61400-12-1, 2005) guideline the measurement procedure is defined. The actual measurement procedure consists in collecting the data for the different variables that should meet a set of further clearly defined criteria to ensure that the data are of sufficient quantity and quality to determine the power performance characteristics of the wind turbine accurately. The acquired data at a frequency of at least 1 Hz are averaged over periods of 10 min (1 min for small wind turbines) and these mean values together with the corresponding standard deviations are used for the following analysis.

Whether on the type of power control strategy, either the power averages P_{ave} (for passive stall-regulated turbines) or the mean values of wind speed U_{ave} (for turbines with active power control) are normalized to a reference air density ρ_0 considering the effect of density variation on available power flow on undisturbed wind. The corrections are respectively:

$$P_n = P_{ave}\frac{\rho_0}{\rho_{ave}} \qquad \text{and} \qquad U_n = U_{ave}\sqrt[3]{\frac{\rho_{ave}}{\rho_0}} \qquad [2.2.1]$$

The measured power curve is determined on the basis of the normalized values (P_n, U_n) by applying the so-called method of bins. The wind speed values are divided into intervals of 0.5 m/s each, and for each interval bin averages of wind speed and power output are calculated.

The power curve is assumed to be complete or reliable if each bin includes a minimum of 30 min of sampled data and the entire database covers a minimum period of 180 h of data sampling. The covered wind speed range shall at least extend from 1 m/s below cut-in wind speed to 1.5 times the wind speed at 85 % of the rated power of the wind turbine.

Subsequently, the AEP (annual energy production) is estimated by applying the measured power curve to a reference wind speed distribution for different annual average wind speed at hub height according to:

$$AEP = N_h \sum_{i=1}^{N} \left[F\left(U_i\right) - F\left(U_{i-1}\right) \right] \left(\frac{P_{i-1} + P_i}{2} \right) \qquad [2.2.2]$$

N_h is the number of hours in one year, U_i and P_i are the points of the measured power curve for all N_h bins and $F(U)$ is the theoretical wind speed distribution. The guidelines indicate that the Rayleigh distribution shall be used whereas the Weibull distribution is widely used in wind power forecasting.

The wind speed and power values of the measured power curve shall be used in order to evaluate the power coefficient.

$$C_{p,i} = \frac{P_i}{\frac{1}{2} \rho_0 A U_i^3} \qquad [2.2.3]$$

The IEC 61400-12-1 provides also a description of the evaluation of uncertainty in the power performance measurement. Single uncertainty components are divided into category A and category B uncertainties in compliance with the (ISO - GUM, 1995). In appendixes the assessment and the calibration of anemometer are discussed.

Particular attention on wind turbines with a rotor area less than 200 m^2 is paid in the last revision of the guideline inserting particular provisions in appendix H (power performance testing of small wind turbines). A non-trivial variation is the 1 min average instead of 10 min average of data that is due to the smaller inertia of the machine and shorter distances between turbine and anemometer.

2.3 **Influence factors in power performance tests**

Power performance tests assessed in natural sites are influenced by several ways; most of the causes of these effects are related to the atmospheric wind variability interacting with the turbine, the anemometer or both. Some of these effects determine a performance variation of the WECS whereas others determine only an error on the power curve construction. In the following sections, the most important influence factors on power curve assessment of wind turbines are briefly discussed with particular attention on small wind turbines applications.

2.3.1 Atmospheric turbulence

The atmospheric turbulence in the planetary boundary layer is an important issue in wind power converter for both performance and structural aspects.

Rapid wind speed fluctuation with frequencies less than several minutes are referred as turbulence. In the chapter 5the turbulence and its effects in wind turbine power curves are extensively discussed, therefore at this point, only a brief list of these effects is reported.

The turbulent flow over the rotor determines different aerodynamic forces on the blades compared to laminar flow condition. In particular the high frequency turbulence influences the stall behaviour over the airfoil (Sicot et al., 2006) whereas rapid variations of the wind velocity at the leading edge determines rapid fluctuations in aerodynamic condition forcing the blade to work in transitory condition (i.e. not passing through steady state). These aero dynamical effects seem to be secondary in wind turbines performance and are not investigated in this work. The turbulence introduces several disturbances on the measurement of the correlation between driving wind and power output. Firstly the spatial and temporal variability of the turbulent wind determines lack of correlation between measured speeds at the anemometer and speeds at the rotor plane. Moreover small turbulent fluctuations measured by the anemometer may hit only part of the rotor or may fade out before reaching the rotor. The location of the anemometer and procedure for wind and power measurement along with the averaging time adopted suggested by the guidelines are aimed at improving the representativeness of wind measurements.

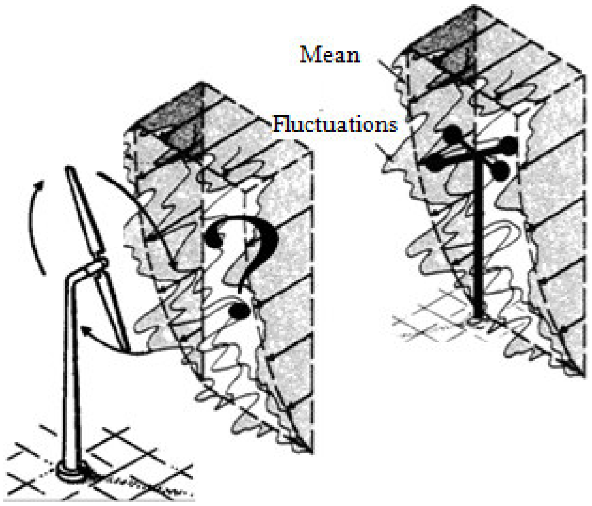

Figure 6: Wind turbine and anemometer in turbulent wind

Another effect of the turbulence is related to the time average operation and the non linearity of the power curves give rise to incorrect assessment of the power curve. These aspect are of real concern in power performance and are deeply investigated in this work (Alberts et al., 2007) (Antoniou et al., 2007) (Battisti et al., 2009) (Christensen et al., 1986) (Kaiser et al., 2007) (van Radecke, 2004) (Rosen & Sheinman, 1994). An analytical model for the correction of this effect is developed and applied on the experimental data harvested in the test site of Trento.

2.3.2 Vertical wind gradient

The vertical gradient of the wind speed characteristic of the planetary boundary layer causes the non uniformity of the wind speed over the rotor area. The shape of the vertical wind profile mainly depends on the surface roughness, on the site morphology and on the atmospheric stability condition. In literature many studies modelled the wind shear (Battisti et al., 2009) (Elliot et al., 1990) (Rozenn et al., 2010) (Tindal et al., 2008) (Wagner et al., 2009) the most common models are based on the logarithmic and the exponential laws.

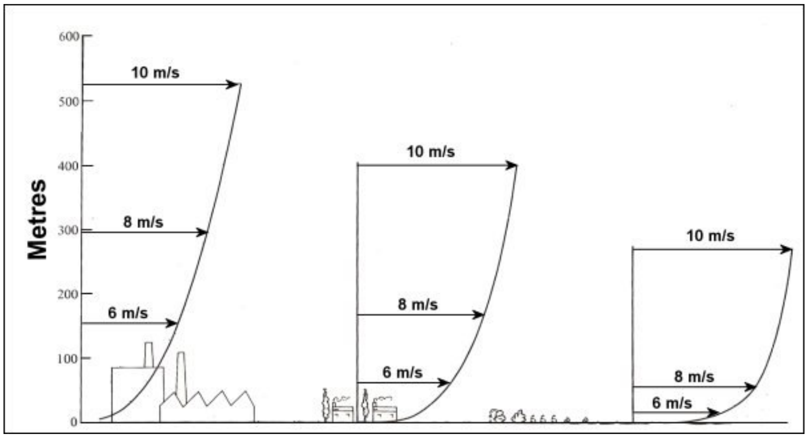

Figure 7: Vertical wind speed profile for different terrain textures

The effect of this wind speed changes within the swept rotor area on power performance testing is a lost of representativeness of the hub height wind speed. In fact, the non-linearity of the wind speed profile determines the difference between the wind speed averaged on the rotor area and the wind speed measured at hub height. Moreover, considering that the wind power is a cubic function of the velocity this lost of representativeness is also present with linear vertical profile. In tall wind turbines, where the diameter of the rotor reaches 120 m, several studies on the influence of wind shear in power performance testing (Wagner, 2010) (Antoniou et al., 2007) were compared to numerical models. The proposed corrections are based on multiple measures of the wind speed at different height and weighted average on the rotor area. On small wind turbines, where rotors diameter are less than 16 m, the representativeness of the wind speed at hub height is usually acceptable. The analysis carried out in the test site of Trento for a 11kW wind turbine (Battisti et al., 2009) confirmed this assumption.

2.3.3 Power train dynamics and wind velocity fluctuations

The dynamics of the turbine power strongly interacts with wind speed fluctuations in relation to the frequency response of the WT in the range of characteristic frequencies of the wind. In particular, considering the range of response frequencies of commercial WECS, we are interested on the effect of speed fluctuation due to the turbulence that may be filtered by the wind turbine dynamics.

The wind energy converter system is composed by the rotor, possibly a gear box and the generator connected by low speed and high speed shafts, the power control and a possible pitch regulation. This is the mechanical system to be modelled to characterize the transfer function between the wind speed (or directly the aerodynamic torque) and the electrical power output. (Miller et al., 2003)

Depending on whether the wind turbine will work at fixed or variable speed, on the control strategy and naturally on the turbine size (i.e. on the inertia of each component) the frequency response of the system is a low-pass filter with higher or lower cut-off frequency (e.g. variable speed and higher inertia determines lower cut-off frequency). Fluctuations in wind speed faster than the cut-off frequency are not converted (or only partially converted) in electrical power determining a lack of coherence between the instantaneous wind speed and the power output. The time averaging operation over 10 minutes imposed by IEC guidelines avoid this lack of coherence but for shorter averaging time this dynamical effect must be taken into account.

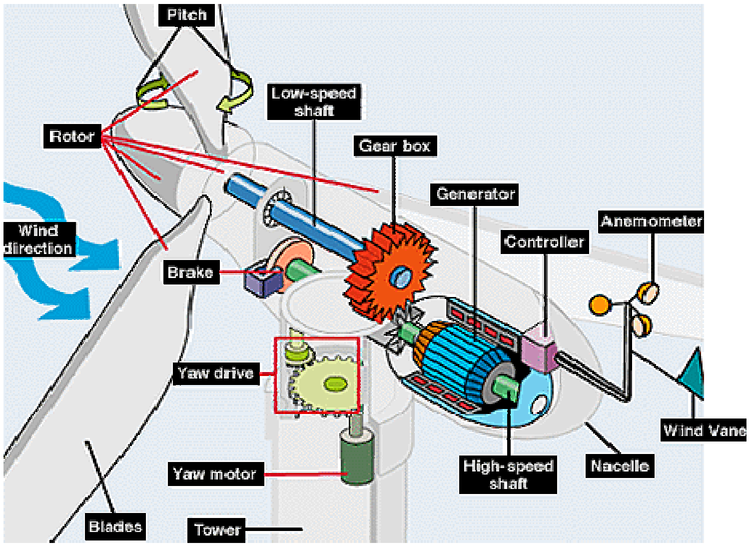

Figure 8: Power train and control system of a WECS

Small wind turbines have typically a faster dynamics that allows the conversion of a part of the turbulent fluctuations. These faster dynamics are the main reason of the averaging times (1 minute) suggested by the (IEC 61400-12-1, 2005) for SWT power performance tests. The effect of dynamics is as important as the turbulence of the wind is high like for small wind turbine located at low height from the ground and in urban or sub-urban areas.

2.3.4 Yaw dynamics and variable wind direction

As the power train dynamics prevents the rotor to follow rapid wind speed fluctuations, the yaw dynamics response influences the ability of the WT to follow changes in wind direction (i.e. to keep the rotor headed into the wind). The yaw dynamic of the wind converter can be very different depending on the solution adopted. In fact there can be an active yaw regulation that rotates the nacelle by means of electrical or pneumatics actuators according to a control law based on the nacelle-wind misalignment measured by a wind vane. Passive yawing system (i.e. free yaw) are almost used in SWT on downwind turbines or on upwind machines equipped with aerodynamic tail.

The application of the momentum theory at the rotor in steady yaw, commonly used for power assessment in yawed flow (Burton et al., 2002, pp.96-98) show that in steady state the maximum extractable power decreases with the cube of the cosine but little is known about the performances on unsteady yaw conditions.

The effect of yawed flow in tall wind turbines is of real concern for structural issues whereas, because of the active yaw regulation and the spatial averaging effect of the rotor on the wind direction variation (induced by the atmospheric turbulence), are negligible for power performance assessment.

In small wind turbines the dimension of the turbulence gusts can be of order the rotor dimensions involving the whole turbine in the direction fluctuations (i.e. the rotor do not average out the turbulent wind direction fluctuations) and so determining a decrease of the power output. Moreover, in small wind turbines where free yaw system are diffused, the dynamics of the yaw can lead to frequent and excessive corrections which force the turbine to work frequently in yawed configuration. It is important to note that at lower hub height typical of SWT (10 - 30 m) the higher turbulence determines an higher variability on flow direction.

2.3.5 Vertical components of wind velocity

The vertical wind components cause an aerodynamic situation similar to the condition of yawed rotor but there are no regulations (neither active nor passive) that hollow to tilt the rotor perpendicular to the wind flow. This vertical wind component can be caused by thermal effect or by the terrain morphology (Hannah, 1997).

In complex terrain the effect of upflow (more frequent than downflow because of the need to install the WT in exposed zone) in the energy production can be of real concern as it was evidenced in (Yoshida, 2006) where the average vertical flow inclination is about 7 degrees.

Furthermore, the tilt angle of the rotor, needed for avoiding flexible blade-tower collisions, forces the wind turbine to work in misaligned condition even if the wind flow is horizontal; this performance reduction do not depends neither on the site nor on the wind characteristics but is an intrinsic characteristic of the machine (i.e. do not introduce dispersion on power curve assessment).

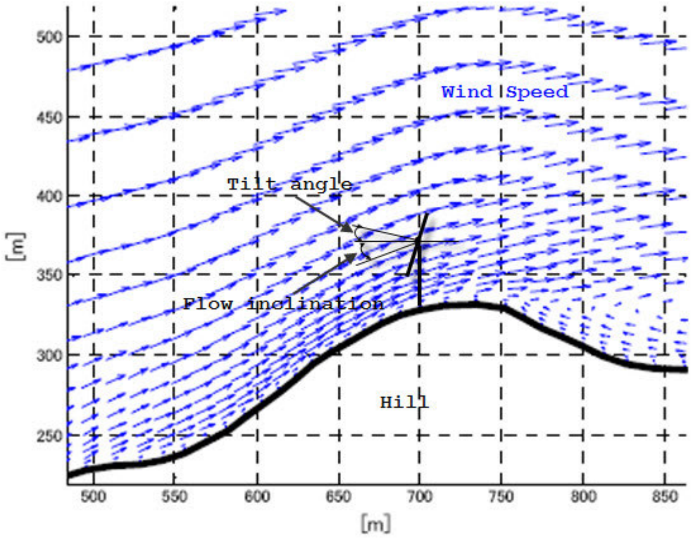

Figure 9: Vertical wind speed components over hill

2.3.6 Cup Anemometer Overspeeding

It is well known in literature that cup anemometers used in a turbulent wind get slightly non-linear. In (Busch & Kristensen, 1976) anemometer overspeeding has been treated extensively. The basic reason for this effect is the following: when the wind speed fluctuates, the cups have to accelerate and decelerate under the influence of the moment induced by the difference between the present wind speed and the wind speed corresponding to the present speed of rotation. This induced moment is non-linear around zero moment. If the cup anemometer is very heavy and therefore reacts slowly to wind speed changes, rather large speed correcting moments must come into play and the non-linearity will therefore induce errors.

The best way to avoid this error is to use small, light weight cup systems (or even better anemometers like ultrasonic or lidar systems). The cup response to wind is traditionally described by a distance constant *L*. The response time of the cup is then *L/u*, i.e. the response is faster if u is high. For this reason the (IEC 61400-12-1, 2005) recommended the anemometer class to use depending on the site complexity.

2.3.7 Blade and instrumentation icing

Turbine operating in cold climates or on mountains environments can be subjected to blade icing. Several studies show that (Tammelin, 2000) wind turbine performance changes in response to ice accretion on the blades. Turbines of different sizes or operating parameters will have different behaviour on the same site. Non-dimensional analysis (Battisti, 2008) indicates that for relatively small droplets $(d/D)^2 << 1$ the icing will be not an important issue, while for small bodies or for smaller parts of larger bodies, icing will be important. Small wind turbines, due to the large rotational velocities and smaller chords are more prone to icing than larger turbines (Battisti, 2005).

Figure 10: Wind farm in the Alps – Tauernwind (Negrente, 2009/2010)

The aerodynamic penalties due to icing depend on the airfoil shape: thicker airfoils with blunt leading edge would be less prone to drag reduction with ice, and any correlation among ice shape, angle of attack, and change in drag is more progressive.

In Figure 11 the level of contamination in terms of mass distribution is denoted as very light (CL0), light (CL1), normal (CL2) and heavy (CL3) where normal is based on the Germanischer Lloyd trapezoidal rule (GL Wind, 2005). The power curves are seen to show little change in shape for the first three contamination levels. Rather they are simply offset to higher velocities with higher ice accretion. However, the fourth level, CL-3, produces a marked change in the power curve.

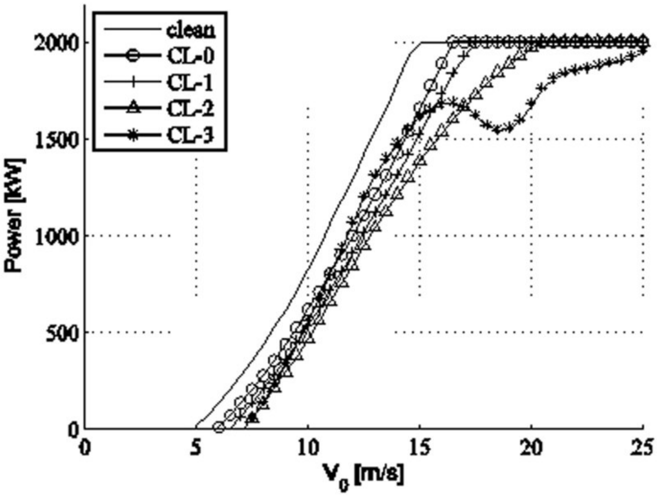

Figure 11: Calculated power curve for a 2MW WT with different ice contamination

Ice detection is a challenging task in wind energy. The analysis of the number of icing days during the wind resource evaluation phase often uses the combination of heated and unheated anemometers.

2.3.8 Blockage effects on the anemometer

The blockage effect due to the turbine work extraction on the wind flow may influence the anemometer measurement when it is upstream of the turbine. The location of the met mast is a compromise between mitigating the upwind reduction in wind speed due to the presence of the wind turbine (blockage effect) and achieving a strong correlation between measured and "driving" wind speeds. The IEC61400-12-1 guideline takes in account this problem:

"Care shall be taken in locating the meteorological mast. It shall not be located too close to the wind turbine, since the wind speed will be influenced/changed/ affected in front of the wind turbine. Also it shall not be located too far from the wind turbine, since the correlation between wind speed and electric power output will be reduced. The meteorological mast shall be positioned at a distance from the wind turbine of between 2 and 4 times the rotor diameter D of the wind turbine. A distance of 2.5 times the rotor diameter D is recommended."

A small speed deficit is still present at 2.5D upstream the turbine and this is discussed in (Tindal et al., June 2008) that pointed out that for more accurate AEP prevision some corrections has to be introduce.

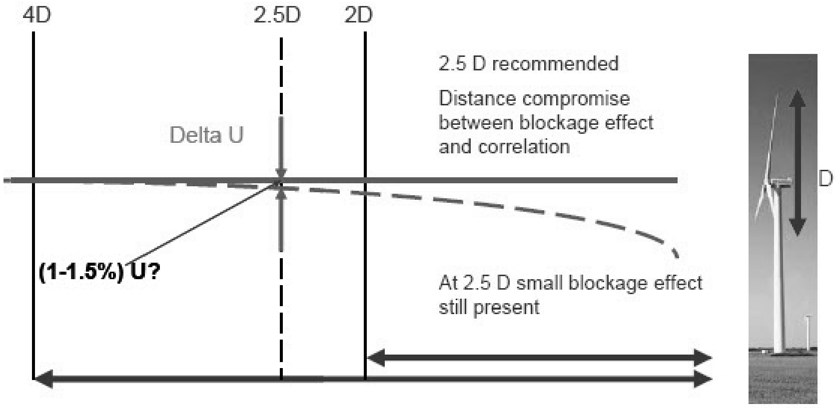

Figure 12: Upstream blockage effect of a wind turbine

However it seems to be negligible for single wind turbine testing and in presence of a wind speed that do not blows always from the blocked sector and, for small wind turbines in complex terrain, the need of a better correlation between measured wind and driving wind is stronger.

2.3.9 Instrumentation accuracy

Only for completeness the effect of measurement uncertainties are reported herein because it is not a particular issue of WT application and so, whereas is of primary importance, is not object of scientific studies. The principal effects on the power curves uncertainty of measurements uncertainties come from the anemometer, the site calibration and the measurement of power output. The IEC61400-12-1 provides several recommendations on the accuracy of the sensors employed and on the sensors location. Then, following the guide to the expression of uncertainty in measurement (ISO - GUM, 1995) , the procedure to evaluate the uncertainty on power curve and finally in AEP are described.

3 THE ATMOSPHERIC WIND

3.1 Wind in atmospheric boundary layer

The atmospheric boundary layer (ABL) is the lowest 1-2 km of the atmosphere where thermal effects due to the sun radiation and mechanical effects due to the surface morphology determine the high irregularity of the air motion ($Re = 10^8$-10^9).

Above the ABL is the free atmosphere, where flow is in near geostrophic balance and no longer influenced by surface friction.

Modern tall wind turbine can reach, with the blade tip, 150-200 m whereas small wind turbines work at about 10–50 m from the ground and hence the ABL properties are of great interest on wind energy harvesting, in particular the wind speed vertical gradient and the turbulence.

The ABL is changing continuously in response to the cyclic heating and cooling of earth's surface and three states are observed: stable, unstable or neutral stratification. Unstable stratification occurs in daytime when convectively mixed boundary layer takes place. The surface heating cause warm air near the ground to rise, while it rise, it expands due to reduced pressure and therefore cools adiabatically.

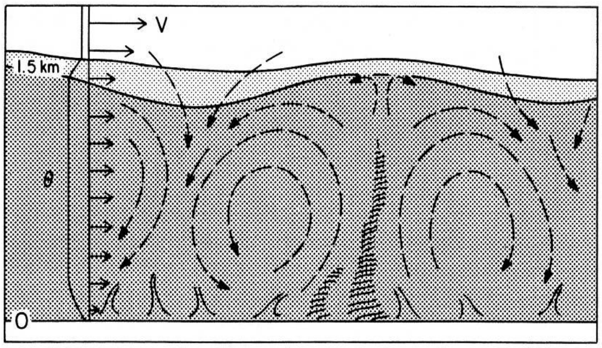

Figure 13: Unstable convective boundary layer circulation

If cooling is not sufficient to reach the thermal equilibrium air will continue to rise (thermals). This results in large-scale turbulent eddies. There is a lot of vertical mixing and transfer of momentum, resulting in a relatively small change of mean wind speed with height (low wind shear). Even in the lower 20-50 m surface layer the mechanical effect determines a steep vertical gradient of the wind speed and small eddies due to surface roughness.

If the adiabatic cooling effect causes the rising air to become colder than its surroundings, its vertical motion will be suppressed. This is known as stable stratification. It often occurs on cold nights when the ground surface is cold. In this situation, turbulence is dominated by friction with the ground, and wind shear can be large. The turbulence of this stable boundary layer is characterized by small eddies particularly in the surface layer.

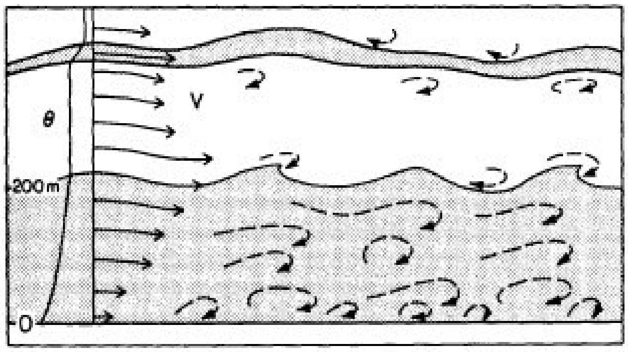

Figure 14: Stable boundary layer flow with small eddy structure.

In the neutrally stable boundary layer the air parcels are displaced up and down adiabatically and maintain exactly the same density as the surrounding air and thus experience no net buoyancy forces. This is often the case in strong winds, when turbulence caused by ground roughness causes sufficient mixing of the whole boundary layer.

These three states of the ABL well depict the chaotic behaviour of the air motion over the surface where the turbulent structure is composed both by thermal and friction effects leading to various scale eddies superposed each other that interact with the main wind flow (if present). In following a brief discussion on large and small scale variability clarify the different between turbulence and other wind fluctuations.

3.2 Temporal variation of the wind speed

From the point of view of wind energy, the most striking characteristic of the wind resource is its variability. The wind is highly variable, both geographically and temporally. Furthermore this variability persists over a very wide range of scales, both in space and time.

The wind speed variation in time can be seen as the consequences of cyclic variation with different time scale ranging from years to less than a second. The typical power spectral density of the wind speed signal weighted in frequency (rigorously defined in following) well depict this different-scale superposition.

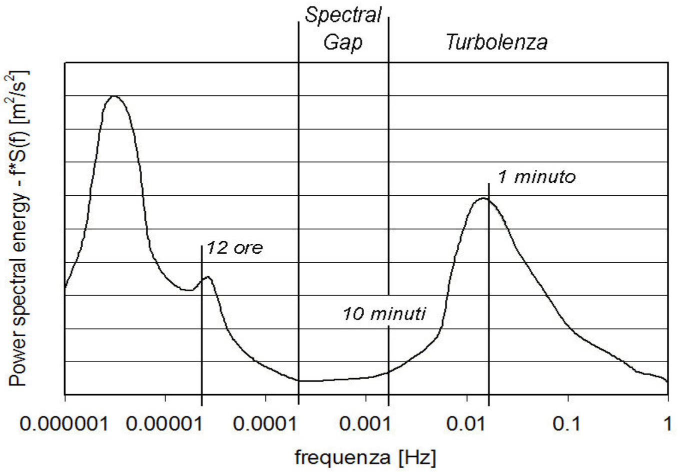

Figure 15: Power spectral density of the wind speed (log scale)

Long-term variations of the wind, in the scale of several years are not well understood and are uncertainty sources in energy production forecasting. Seasonal variations are much more predictable, although there are large variations on shorter time-scales still, which although reasonably well understood, are often not very predictable more than a few days ahead. These are the synoptic variations related to the passage of weather systems. How explained above, the thermal activity determines considerable daytime variations (diurnal variations) which again are usually almost predictable. On these time-scales, the predictability of the wind is important for integrating large amounts of wind power into the electricity grid, to allow the other generating plant supplying the grid to be organized appropriately.

The highest frequency peak is related to the turbulence that is characterized by chaotic small time and spatial scale fluctuations. Of particular interest, and very useful for the wind energy studies and meteorology, is the so-called ‘spectral gap’ occurring between the diurnal and turbulent peaks, showing that the synoptic and diurnal variations can be treated as quite distinct from the higher frequency fluctuations of turbulence. Typical, there is very little energy in the spectrum in the region between 2 hours and a few minutes so that the turbulent fluctuations can be well separated by lower wind speed variation and allow to treat the two phenomena (i.e. wind speed variation and turbulence) separately.

3.3 **The turbulence**

Turbulence generally refers to chaotic three-dimensional fluctuations in wind speed on a relatively short time-scale, typically less than about 10 min. It is useful to think of the wind as consisting of a mean wind speed determined by the seasonal, synoptic and diurnal effects described above, which varies on a time-scale of one to several hours, with turbulent fluctuations superimposed that can be distinguish because of the above mentioned spectral gap.

Although the turbulence is obviously governed by the physical law derived from the conservation of mass, momentum and energy it is generally described by its statistical properties and treated like a stochastic phenomena. This is due to the extreme complexity of this process that involves temperature, pressure, density and humidity interacting with three dimensional motion of the air and the earth's surface.

The Reynolds hypothesis for generic turbulent flows allows to describe a variable in a point of the space and time domain as a superposition of a turbulent fluctuation (with zero mean) and a certain ensemble mean.

$$U(x,y,z,t) = \left\langle U \right\rangle (x,y,z,t) + u'(x,y,z,t) \qquad [3.3.1]$$

Where u' is the fluctuation and <U> is the ensemble mean that is not very useful in practical application. The ensemble mean is commonly substituted by the simpler time average ū on a certain point in the space:

$$\left\langle U \right\rangle \cong \overline{U} = \frac{1}{T}\int_0^T U \ dt \qquad [3.3.2]$$

This assumption requests the validity of ergodicity hypothesis, i.e. the fluctuation must be stationary, in statistical sense, over the time period *T* chosen for the analysis. Although the atmospheric boundary layer is far from stationary (see 3.1) this assumption can be acceptable for short time scale in which the overall properties of the atmospheric boundary layer do not vary too much like in the spectral gap (between 1 hour and few minutes).

Another hypothesis utilized in turbulence analysis is the Taylor's frozen turbulence which assumes that the turbulent eddy does not vary its structure as it is convected by the mean wind past the sensor. Obviously, in the ABL, it is not generally true but can be accepted when the characteristic length scale of the turbulence observed divided by the mean velocity at which is transported (i.e. the crossing time) is small compared to the evolution time of the turbulence. This assumption allows to switch between time and length scales only by knowing the mean wind speed, and is widely used in spectral analysis. (Monin & Obukhov, 1954)

In Figure 16 a time series of wind speed data from the Trento test site at a sampling frequency of 0.5 Hz well depicts the amount of turbulence fluctuation with a time-period less then few minutes whereas 10 minute and lower fluctuations are small. In black and blue there are respectively the 10 minutes and the 1 minute averages.

For this reason it is common to average the wind speed over a time of 10 min period in wind energy application (30 min in meteorological studies). Naturally, in the practice, the wind speed is acquired discretely at a certain sampling frequency f_s and hence the time average is defined by the sum over the T/ f_s samples instead of the integral.

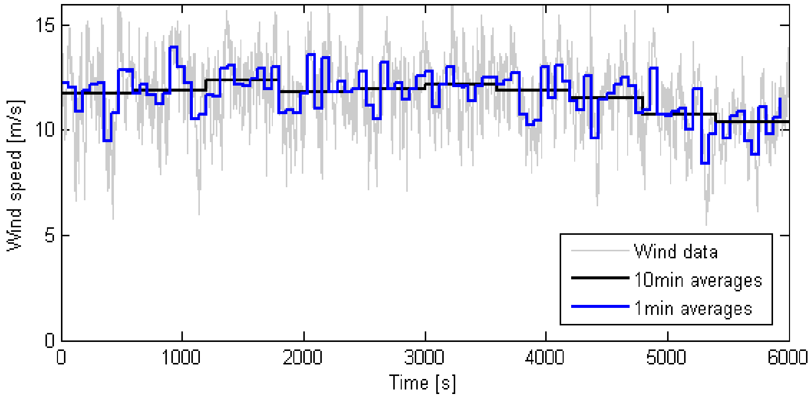

Figure 16: Wind speed time series and time averaged data from Trento test site.

Defined the time average is straight forward to define the variance σ_u^2 of the wind speed on the same time period that is the second order central moment of the statistic. The turbulence intensity is the most used statistical descriptor of the turbulence and is defined as:

$$I_u = \frac{\sigma_u}{\overline{U}} \qquad [3.3.3]$$

Turbulent wind speed variations can be roughly considered to be Gaussian distributed, with the standard deviation σ_u^2, about the mean wind speed U in the time period T.

In Figure 17 the probability density of the wind speed fluctuation over a 10 minutes sample is compared with a normal probability density function with the same variance, the skewness and kurtosis of the data set are also reported in order to demonstrate the validity of the Gaussian approximation in this data set. Unfortunately this is not always true depending on the stationarity of the time period and so on the consistency of the spectral gap. Generally speaking, for the aim of studying the effect of turbulence on power curves, this approximation can be accepted and the turbulence structure can be characterized by the turbulence intensity above defined. This approximation has to be kept in mind for problem understanding and further improvements.

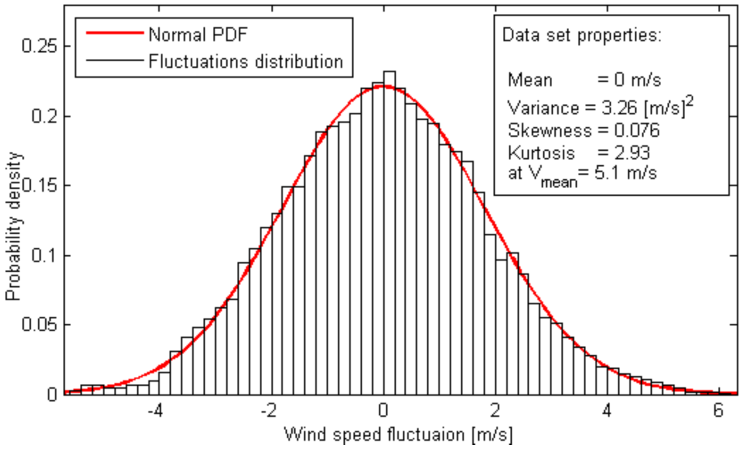

Figure 17: 10 minutes wind speed fluctuations distribution at 5.1m/s compared to normal PDF.

In Figure 18 the turbulence intensity, skewness and kurtosis for a time series of wind speed data of 15 days are reported as a function of the respective mean wind speed. Each point represents the statistical value (I, S or F) in a 10 minute period as a function of the mean velocity value over the respective period. Raw data were sampled at 0.5 Hz at 18m height in the Trento test site during February 2008. The decrease of turbulence intensity with increasing mean velocity is a typical behaviour because when a strong wind is blowing the thermal turbulence is slightly suppressed and a more neutral situation is achieved. This dependence of I on the mean value of U is utilized as a site specific characteristic specifying the design requirements for wind turbines, where this relation is used to define different wind turbine classes corresponding to respective categories of turbulence characteristics (IEC 61400-1, 2005). Observing skewness and kurtosis it is clear that the Gaussian distribution is not always applicable especially in low wind speed, at which the wind turbine probably does not operate.

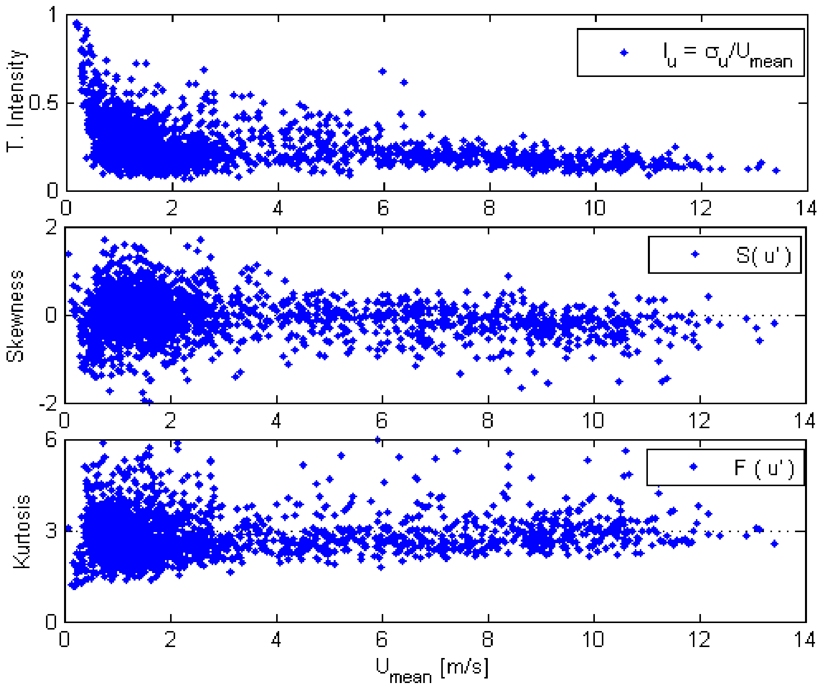

Figure 18: Turbulence intensity, skewness and kurtosis of 15 days of 0.5Hz wind speed data conditioned over 10 minute periods as function of respective mean wind speed.

Recent works (Bottcher et al., 2007) (Gottschall, 2009) (Peinke et al., 2004) relate to the Gaussian approximation as not acceptable for atmospheric wind speed that is highly unsteady and postulate that power correction based on the Gaussian distribution of the wind speed fluctuations over the averaging period suffers from this effect. They support this thesis by showing the 10 min average based speed fluctuation distribution over a long time series, hence treating all the 10 min set of almost Gaussian wind fluctuations as a single population. The result is a well known fat-tail distribution like the one of Figure 19, here the fluctuations based on 10 minute average for 15 days at 0.5 Hz (i.e. the same fluctuations used in Figure 18) are treated as a single set and the probability density of this fluctuations is compared to the normal PDF with the same standard deviation and zero mean.

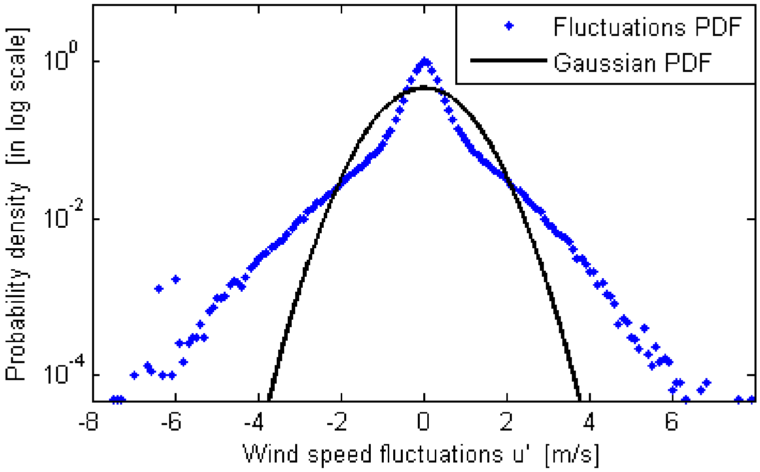

Figure 19: PDF of the fluctuations based on 10min averages over 15 days of data at 0.5 Hz

Thinking on the above description of the turbulence in ABL and on the stationarity hypothesis it is not surprising the strongly non-Gaussian distribution. In Figure 19 fluctuations representing very different situation are reported (i.e. different turbulence intensity and different U mean) and so it is a superposition of 2058 roughly Gaussian distribution with different standard deviation. However this does not affect the validity of the Gaussian approximation on each single 10 min average (that is important for our model) but proves that it is not possible to consider only the turbulence intensity when a long time data series (at less more than few hours) as to be characterized or predicted. The superposition model proposed by (Castaing) and refined by (Bottcher et al., 2007) well depict this statistic composed by several subset of Gaussian distribution with standard deviation distributed in a log-normal PDF and mean wind speed distributed like a Weibull distribution. In conclusion of this dissertation, in Figure 20 the PDF of the fluctuations normalized by the respective 10 minutes averaged wind speed over the same 15 days of data are reported but selecting only the 10 minute period with a turbulence intensity between 15% and 17%.

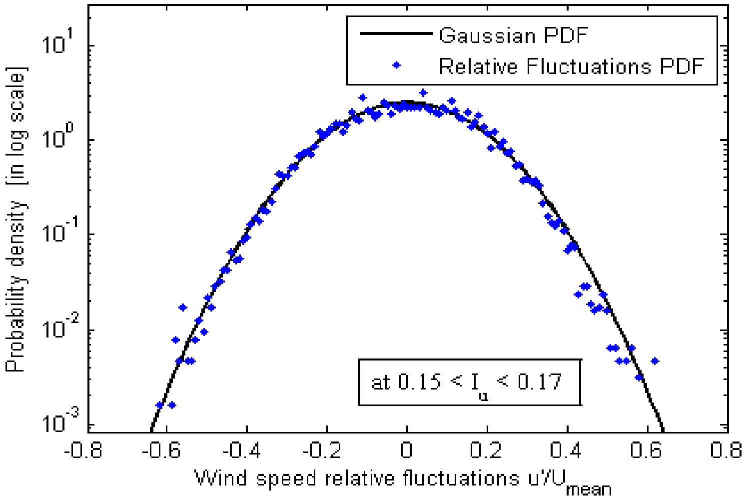

Figure 20: PDF of the normalized fluctuations based on 10min averages for data set with turbulence intensity between 15 % and 17% (213 sets)

The experimental data fits very well the Gaussian distribution proving that characterizing the turbulent data sets by their turbulence intensity (and normalizing the fluctuation by the respective mean value) is a good practice in order to isolate homogeneous period of data with similar fluctuation distribution. Anyhow, the fat-tail overall distribution is very important in particular for risk assessment of strong wind gusts on the design process (IEC 61400-1, 2005), but this is not the aim of this work.

3.4 **Turbulence spectra, length scale and coherence**

Turbulent eddies in boundary layer are spatially extensive structures and, ideally, their analysis requires measurements from many points in space. The Taylor's frozen turbulence hypothesis enables us to use the single point measurements as a function of time for spectral analysis. The Eulerian integral time length scale Λ_u, commonly referred to as the integral length scale, is an important indicator of the structure of the turbulent process. It roughly represents the size of the eddies that transport the most of energy and thus give an estimation of the typical spatial dimension of the relevant fluctuations. The definition of the integral length scale needs the autocorrelation function $\rho_u(r)$:

$$\Lambda_u = \int_0^\infty \rho_u\left(r\right) dr \qquad [3.4.1]$$

Typical values for Λ_u in the atmospheric boundary layer are from 10 to 300 m and are strongly dependent on the roughness of the ground and on the height above the ground. Applying the frozen turbulence hypothesis, Λ_u can be defined as the autocorrelation in time (applicable to a single point time series of data) instead of the spatial autocorrelation:

$$\Lambda_u = \overline{u}\mathcal{T}_u = \overline{u}\int_0^\infty \rho_u\left(\xi\right) d\xi = \overline{u}\int_0^\infty \frac{\overline{u'(t)u'(t+\xi)}}{\sigma_u^{\,2}}\, d\xi \qquad [3.4.2]$$

where $\mathcal{T}_u$ is the time integral length scale, u' are the fluctuations about the mean wind speed ū and σ_u is the variance of the wind speed data series. The time integral scale is actually the time in which the fluctuations remain correlated and can be used. Moreover, the autocorrelation of a discrete series of data is an indicator of the stationarity of the wind speed over the period as explained in (Kaimal, 1994).

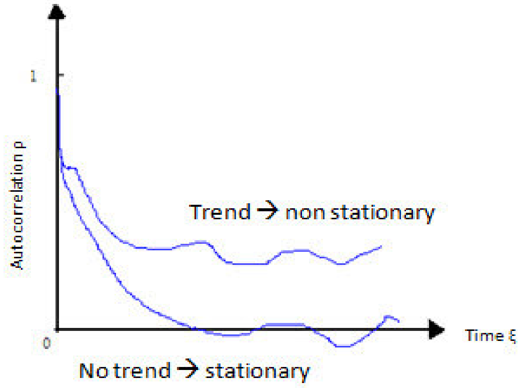

Figure 21: Typical autocorrelation for data set with trend (unsteady) and without (steady).

The one-side power spectral density of the wind speed, directly related to the autocorrelation function, shows the frequency content of the wind speed fluctuation and is formally defined as the Fourier transform of the autocorrelation of the signal.

$$S_u(f) = 2\,\sigma_u^{\;2}\int_0^{\infty} \rho_u\left(\xi\right)e^{-i2\pi f\xi}\; d\xi \qquad [3.4.3]$$

Where $S_u(f)$ is the power spectral density (evenly referred as power spectrum) in function of the frequency f in Hz. In the practice the power spectral density is calculated on discrete and limited time series using the Fast Fourier Transform in order to obtain the power spectrum. The $S_u(f)$ can be derived by dividing the power spectrum by the frequency interval Δf .

$$S_u(f) = \frac{PS}{\Delta f} \quad [3.4.4]$$

The power spectral density is commonly reported as the $f\ S_u(f)$, that is the power spectral density weighted in frequency in order to emphasize the peaks and valleys in the distribution of turbulent energy (Burton et al., 2002) (Kaimal, 1994).

The realization of the weighted power spectral density for turbulence investigations requires high sampled data and special attention on the stationarity of the time series used on the analysis. Moreover the dependence on the mean wind speed requests several time series at each different stationary wind speed that are not easy to realize during real in field tests.

For these reason a number of models of the weighted power spectral density were developed. The (IEC 61400-1, 2005) suggest some model of the spectra to be used in design process. The Kaimal spectrum in non-dimesional form is given by:

$$\frac{fS_u\left(f\right)}{{\sigma_u}^2} = \frac{4f\,\Lambda_u/\overline{u}}{\left(1+6f\,\Lambda_u/\overline{u}\right)^{5/3}} \quad [3.4.5]$$

Another fundamental instrument in turbulence investigation is the coherence. The coherence is an index of the spectral correlation of the turbulence at two separated points (generally on space or in time).

Theoretically the coherence is defined as the cross power spectrum of variations at the two points separated by a distance r normalized by the square root of the multiplication of the power spectrum in each point:

$$Coh_u(r,f) = \frac{\left|S_{u,12}(f)\right|}{\sqrt{S_{u,1}(f)S_{u,2}(f)}} \quad [3.4.6]$$

The principal coherence function that are of interest for wind energy engineering are the lateral and the longitudinal coherence of the longitudinal wind speed, i.e. the

coherence of the wind in the direction of the mean wind speed between two point separated by a distance respectively perpendicular to the wind direction (lateral) and parallel to it (longitudinal). The coherence is used in the structural design process for the load assessment on blades and tower. Studying the effect of turbulence on power curve the coherence and the correlation are important for evaluate the representativeness of the wind speed measurement at the anemometer and in order to estimate the averaging effect on the rotor swept area (Christensen et al., 1986)
For the lateral coherence the (IEC 61400-1, 2005) suggests a model based on the Kaimal spectrum (Kaimal, 1994):

$$Coh\left(r,f\right) = e^{-12\left[\left(\frac{f\cdot r}{\overline{u}}\right)^2 + \left(0.12\frac{r}{L_u}\right)^2\right]^{0.5}} \tag{3.4.7}$$

Other empirical model can be found based on the Karman model (Kàrmàn, 1948) or simplified formulations. In the Kaimal coherence model is plotted in function of the separation and the frequency for experimental parameters acquired on the Trento test site $\overline{u}$ = 6.2 m/s, I_u= 0.34 and L_u = 33.13 m.

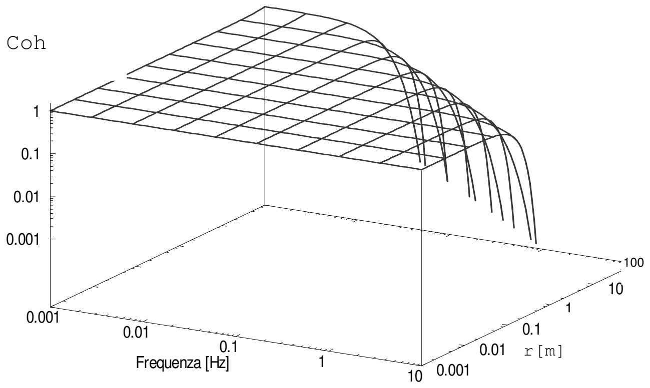

Figure 22: Coherence function from the Kaimal model

Starting from the exponential model of Davenport, (Schlez & Infield, 1998) proposed a simplified coherence model for large separation distance that combine lateral and longitudinal coherence.

$$Coh\left(r,f\right) = e^{-\frac{a_{rc} \cdot f \cdot r}{\overline{u}}}$$

$$a_{rc} = \sqrt{\left(a_x \cdot \cos\alpha\right)^2 + \left(a_y \cdot \sin\alpha\right)^2} \qquad [3.4.8]$$

Where a_x and a_y depend on the turbulence intensity and the mean velocity. This model is useful when the coherence between the anemometer mast and the wind turbine has to be assessed particularly for separation distance higher than 50 meters. In (de Vries, 1979) the minimum value of 0.25 is indicated to consider the wind signal correlated. Others model for the lateral and longitudinal coherence are available in literature (Hojstrup, 1999) (Saranyasoontorn & Manuel, 2004).

4 WIND TURBINES TEST SITE OF TRENTO

The experimental data were collected at the test site located in Trento (northern Italy). Trento is in the Adige valley which is aligned to the north-south direction in the middle of the Alps. The test site is north of the city, embedded in the industrial estate of the town; hence many buildings (maximum height = 20 m) are located all around the site apart from the south-east sector covered by apple trees and a few small houses. A famous and powerful thermal wind ("l'ora del Garda") is blowing transversal to the Adige valley (that is, in the West-East direction); the test site is located downwind a sudden enlargement due to a 600 m mountain.

These surface features coupled with the complex surrounding orography strongly affect the wind regimes of the valley leading to highly irregular winds. Hence, the present Trento test site is suitable to assess the structural and functional behaviour of wind turbines operating in complex wind regimes.

Figure 23: The test site of Trento

Two small-scale wind turbines (11 kW the Gaiawind Turbine, 20 kW the Jimp20 turbine) together with meteorological masts were installed and equipped with sensors to collect power and wind data. A micro-turbine (Zephyr Airdolphin) was also operating in stand-alone configuration.

Figure 24: Wind turbines at the test site of Trento

4.1 Meteorological masts

The meteorological masts are equipped with two cup-anemometers, one at hub height (18 m) and one at 9m height from the ground. A wind vane is mounted at 18 m height over each mast.

The location of anemometers and wind vanes at hub height is crucial to properly correlate measured winds actual driving winds. The lower anemometer is useful not only for measuring wind velocity, but also as a way to doublecheck the correctness of measurements. (MEASNET, 2009).

On the GaiaWind dedicated mast are mounted an hygrometer, a thermometer and a barometer at 17m height along with a tipping bucket rain gauge. An ultrasonic three-dimensional anemometer was installed for one month (June) at 18 m eight on Gaia-

Wind-Mast for high-frequency wind measurements useful for the spectral analysis of the turbulence.

The main technical specifications for the wind measuring equipment are:

Cup-Anemometers:

- Optoelectronic wind speed sensor Thies P6100H;
- Class 1.5A /2.9B in accordance with IEC61400-12-1;
- Delay distance <3 m.

Wind vanes:

- Potentiometric wind direction sensor Thies P6200H;
- Accuracy ±0.25 % ;
- Delay distance < 1 m.

Hygrothermal sensor:

- PT100 and capacitive integrated sensor Thies P6312H;
- Accuracy : ± 0.2 K (temperature), ± 0.2 % (Relative humidity);
- Response time 5 minutes.

Barometer:

- Absolute pressure sensor NRG BP20;
- Accuracy ± 1.5 kPa.

Pluviometer:

- Tipping bucket rain gauge Young 52203;
- Accuracy ± 2 % up to 25 mm /h.

Ultrasonic Anemometer:

- 3-axis ultrasonic anemometer Gill HS100;
- Accuracy ± 1 % RMS;
- Maximum sampling frequency 100 Hz.

Meteorological data were acquired by two data-loggers Ammonit Meteo-32, one for each meteorological mast, at 0.5 Hz. Short time series of data from the ultrasonic anemometer were acquired directly by serial communication on a PC at a sampling frequency of 100Hz for spectral analysis purposes.

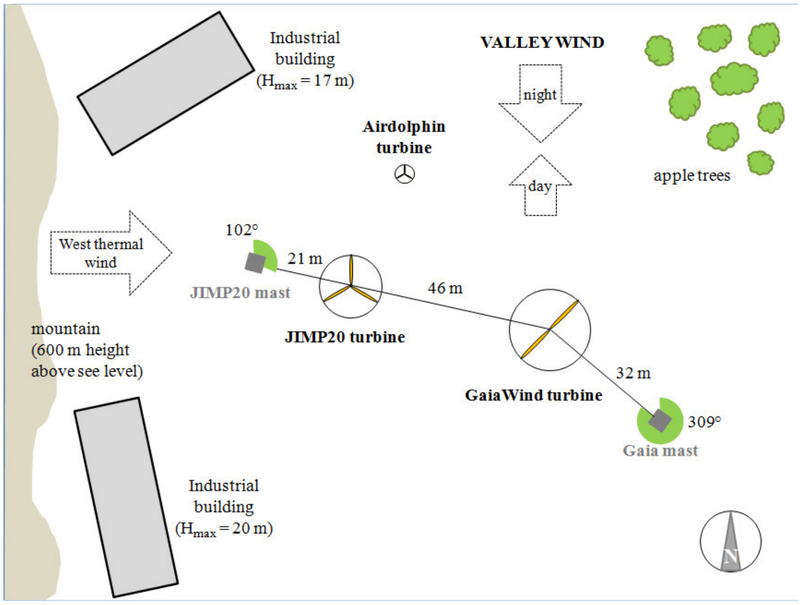

Figure 25: Layout of the Trento test site

Each wind turbine has its own dedicated meteorological mast located at a distance of 2.5 rotor diameter (Figure 25), in compliance with the IEC61400-12-1 guidelines. The layout of the test site was designed to reduce the wind sectors that produce mutual wake effects among the turbines and the masts. By inspecting the scheme of Figure 25, when the wind comes from a sector in which the Jimp20-Mast is downwind of Jimp20 it is also downstream of Gaia-Wind turbine, in roughly the same sector Jimp20 is in the wake of Gaia-Wind so this three configuration where data are influenced by shadowing effect are almost in the same sector. For the Gaia-Wind turbine is approximately the same for opposite wind direction.

4.2 **Wind turbines**

Three wind turbines are installed at Trento site. Gaia-Wind 11kW and Jimp20-20kW are two small wind turbine whereas Airdolphin-1kW is a micro-turbine.

Figure 26: Wind turbines installed at Trento test site

The main characteristics of the wind turbines are as follows:

Jonica - Jimp20:

- upwind three bladed wind turbine, grid connected;
- 20 kW rated power at 12 m/s;
- 8 m rotor diameter at 18 m hub height;
- regulated pitch power control;
- variable speed with synchronous generator.

GaiaWind 11 kW:

- downwind two bladed wind turbine, grid connected;
- 11 kW rated power at 9.5 m/s;

- 13 m rotor diameter at 18 m hub height;
- passive stall power limitation;
- fixed speed with asynchronous generator.

Zephyr - Airdolphin:

- upwind three bladed wind turbine, stand-alone;
- 1 kW rated power at 12.5 m/s;
- 1.8 m rotor diameter at 9 m hub height;
- variable speed with synchronous generator.

The Jimp20 and GaiaWind were equipped with sensors to monitor structural and functional parameters.

On the pitch actuator of Jimp20, an LVP transducer was installed to measure the pitch angle. Two encoders measure the rotor position and speed, along with the yaw angle of the nacelle. Two single-axis accelerometers were installed in the nacelle. The electrical output of the turbine is measured by the inverter, power data are acquisited by means of RS-485.

GaiaWind was equipped by two encoders for the rotor shaft rotational speed and the yaw angle. Accelerometers and strain-gauges were installed on the blade whereas another strain-gauge was applied at the rotor shaft for torque measurement. In the nacelle of Gaia turbine three single-axis accelerometers were installed. The electrical output of GaiaWind is analysed by a net analyser (MeetBox).

The characteristics of the above sensors:

- Encoders: 13bit absolute encoder, binary code;
- LVP: linear inductive displacement sensor, 200 mm range, ±1 mm linearity;
- Strain-gauge Blade: linear strain gauge, 350 Ω range;
- Strain-gauge Torque: torque rosette, 350 Ω range;
- MeetBox: three phase current & voltage measurement. Acc. 0.5 % I, 1 % V;
- Nacelle Accelerometers: single axis piezo 0.5-10 kHz, ± 1 % linearity;
- Blade Accelerometer GaiaWind: triaxial piezo 2-5 kHz, ± 1 % linearity.

4.2.1 Data Acquisition System

The data acquisition system was organised in three subsequent steps:

- Sensors and meteorological masts;
- Acquisition and transmission data system at Trento site;
- Receiving system and data-base at turbo-machinery Laboratory.

The first level was presented above. Data from the sensors installed on Jimp and Gaia turbines were acquired by two acquisition devices (NI-cRIO) installed in the two nacelles; Another NI-cRIO acquired grid data from MeetBox. Turbines data were sampled at 1 kHz by the NI-cRIO and sent to two personal computers, one for each wind turbine. Data from the grid analyser of Jimp20 were directly acquired on Jimp Pc through RS485 at 1 kHz. Meteorological data were collected in the two PC's at 0.5 Hz. The software developed with LabVIEW, acquires and synchronises the data from all devices, performs a data pre-elaboration and then send the data at the turbomachinery laboratory of the University of Trento through remote connection.
The third step is receiving and the storage of the data in the laboratory. All data acquired are organised in a database which is available.

4.3 The wind regime on the test site

The wind regime on the test site is characterised by the interaction between the typical valley wind and the wind blowing during the whole afternoon from the West called "Ora del Garda". The wind regime in the Adige valley, as reported in (De Franceschi, 2004), promotes a nocturnal down-valley drainage current from North and a breeze from South in the afternoon. This valley-wind regime starts from late spring to mid fall, i.e. when the thermal forcing is strong enough to produce a pressure imbalance which moves the air along the valley. The "Ora del Garda" flows regularly on sunny days, when thermal forcing is strong enough to produce an appreciable pressure gradient throughout the valley connecting the area North of the

Garda Lake to the Adige Valley. This wind jumps down in the Adige Valley during the afternoon from a saddle 600m higher than the bottom with a direction which is almost from west. In the test site, located about 800m East of that saddle, the interaction between this wind and the up-valley flow leads to a particular wind regimes with strong diurnal variability (measured diurnal pattern strength = 0.416).

Wind speed and direction data collected in the test site of Trento confirm this greatly variable in space and time wind regimes. The 10 minutes averaged wind data collected during two years (August 2007-July 2009) from Gaia-Mast were elaborated in Table 1.

The values of wind speeds, power and available energy are clearly representative of a low wind site. The low Weibull shape coefficient indicates an irregular wind resource whereas the high mean turbulence intensity highlights the small time-scale irregularity of the wind speed.

	V 18m	**V 9m**	
Height from the ground	18	9	m
V mean (m/s)	2.75	2.42	m/s
V max (10 min averaged)	13.48	11.68	m/s
Mean specific power density	38	25	W/m²
Available specific annual energy	330	220	kWh/m²/yr
Weibull k	1.337	1.408	
Weibull c	2.882	2.597	m/s
Mean turbulence Intensity	0.243	0.261	
Diurnal pattern strength	0.446	0.443	

Table 1: Representative wind data from GaiaMast in trento test site

The wind speed distribution of the 10 minutes averaged data is reported in Figure 27 with the best fit of the Weibull distribution. The two different wind regimes produce ticker tail due to the contribution of the Ora del Garda wind as compared to the Weibull fit.

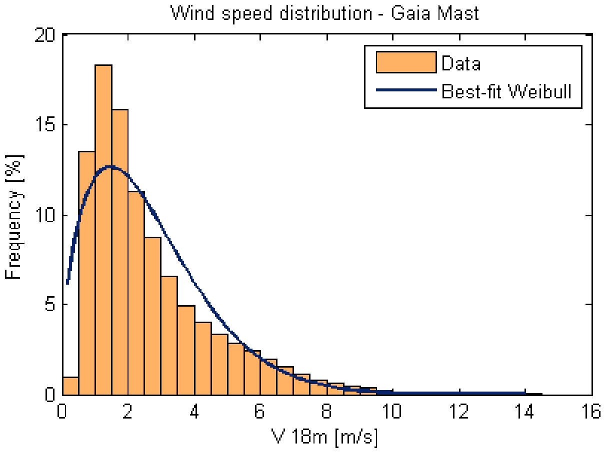

Figure 27: Wind speed distribution at GaiaMast 18m and Weibull best fit

Wind direction data were elaborated to know frequencies and energies in each sector. In the present site the prevailing wind directions were between North-West and North Figure 28. The WSW wind is the above cited "Ora del Garda" whereas from S-SSE the up-valley breeze totals less than 15 percent of the present data.

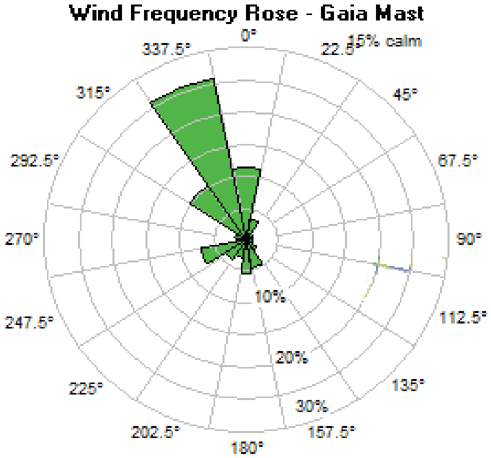

Figure 28: Wind frequency per sector at Gaia Mast 18m

The available energy rose (Figure 29) proves that the downvalley wind flowing from NNW is the most frequent, but some 40 percent of the available energy is contained in the "Ora del Garda" blowing from WSW.

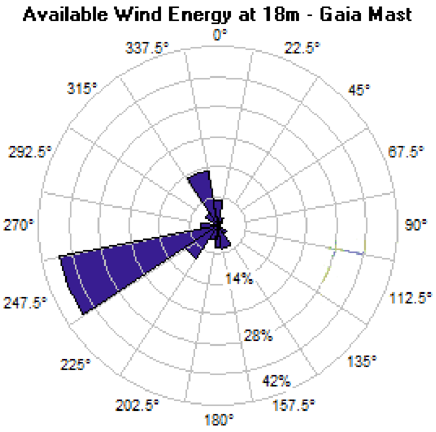

Figure 29: Available wind energy per sector at Gaia Mast

The mean diurnal profile of the wind speed is reported in Figure 30.

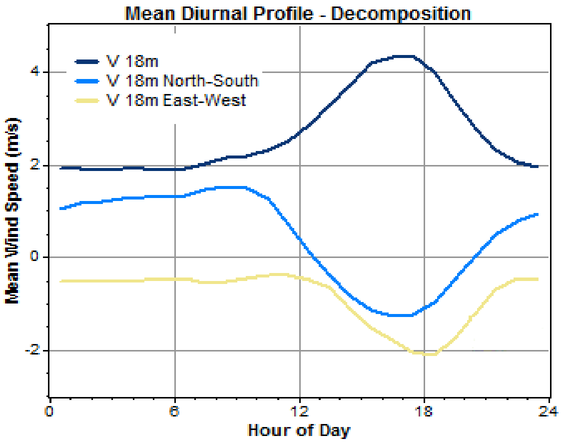

Figure 30: Mean diurnal wind speed decomposed in S-N and E-W components

The projections of the mean velocity on the two cardinal direction are also plotted in order to show the mean provenance of the wind during the day. As explained previously the most windy hours are in the late afternoon due to the "Ora del garda" wind that blows from WSW.

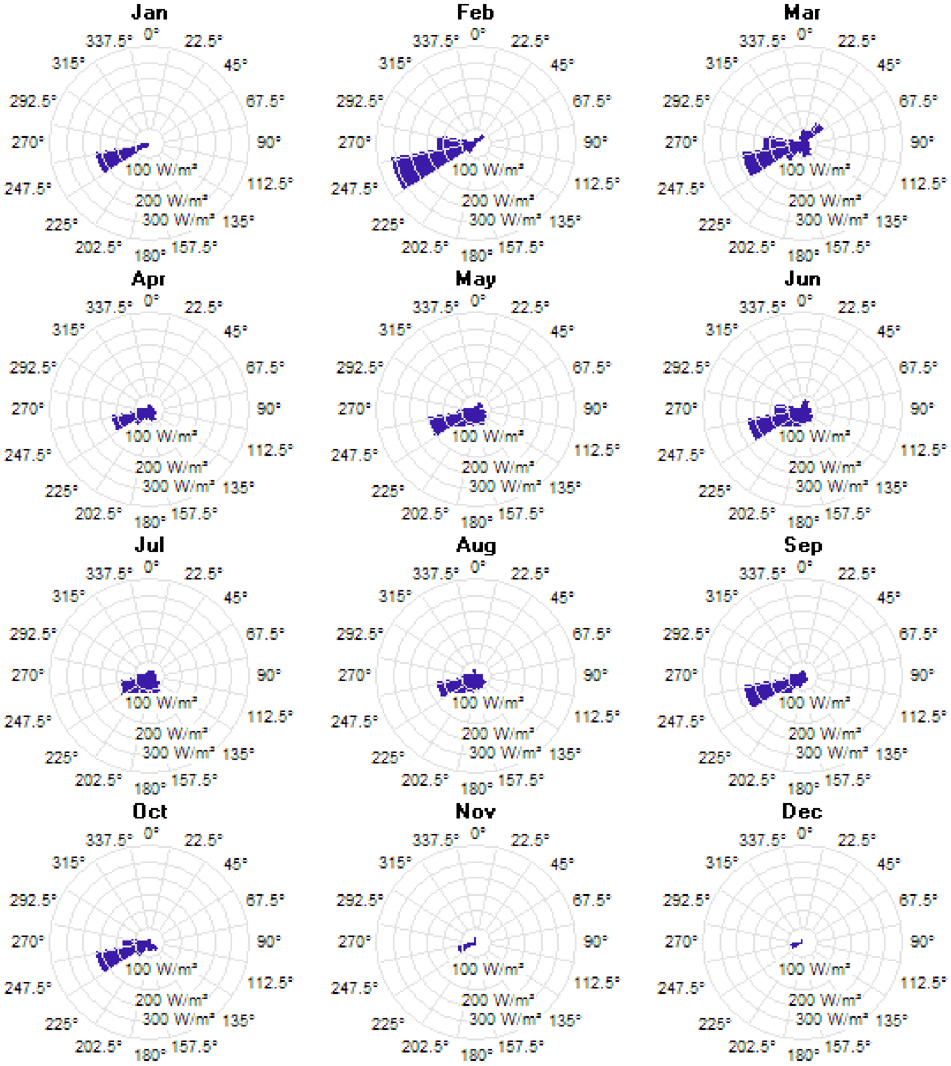

Figure 31: Mean wind energy rose per month – 2 years of data

The wind seasonal variation is shown in figure Figure 31 as a monthly wind power averaged. During November and December the wind is weak while in the first three months and in late summer there is an substantial injection of energy.

April power data are somewhat lower than February's; this is due to a particularly weird meteo of one of the two year observations, it is emphasized that this has no consequences in what follows.

The representative turbulence intensity is defined in the guidelines (IEC 61400-1, 2005) and 2 along with the procedure for its calculation; it is Figure 32 together with the normal turbulence models (curves class A, B, C and SWT) the class A and SWT do overlap due to the parameters definition adopted by the two above mentioned guidelines. Is seen that none of the normal turbulence models wholly describes the turbulence intensity probably because of the interaction between the valley wind and the "Ora del Garda".

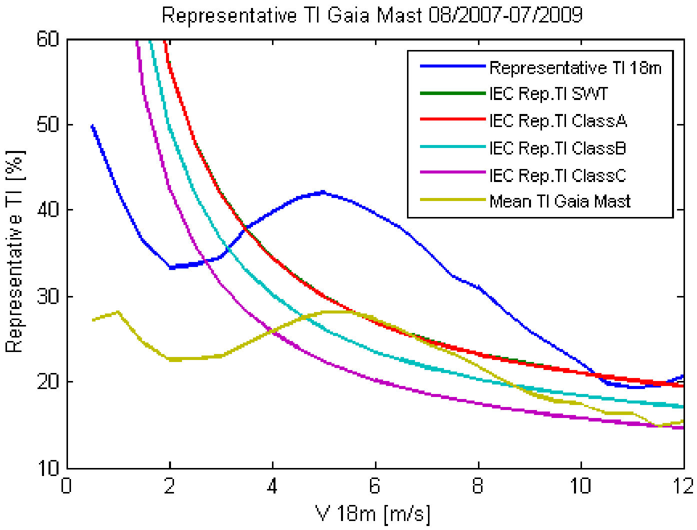

Figure 32: Representative and mean TI at Gaia Mast

4.4 Spectral analysis on Trento test site

In addition to the analysis of ten minutes averaged data and their variance the turbulence at the Trento test site were investigated through the high frequencies time series collected by the ultrasonic anemometer.

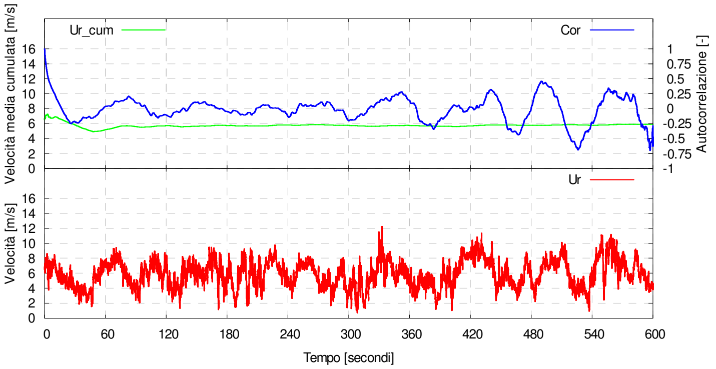

Figure 33: Typical time series for power spectrum assessment on TN site.

The turbulence spectrum was assessed following the (Kaimal, 1994) guidelines and using series of about one hour of data within almost stationary condition.

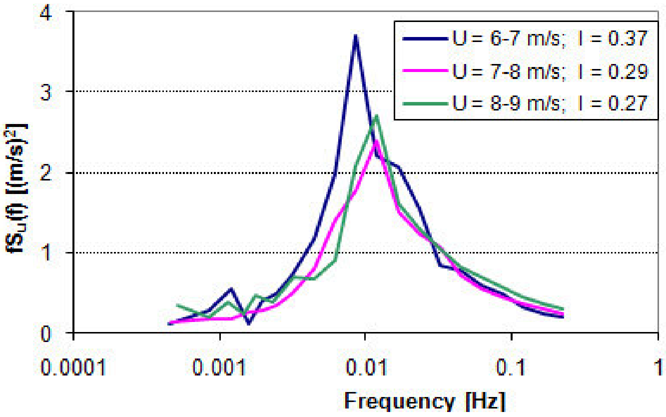

Figure 34:Turbulence Power spectrum weighted in frequency at TN site

The position of the turbulent peak is slightly influenced by the mean wind speed whereas the intensity influences its amplitude.

The high frequency spectrum were matched with the medium frequency and the low frequency power spectrum (each one evaluated in appropriate time series and properly filtered) in order to build the wide frequency range wind speed power spectrum reported in Figure 35.

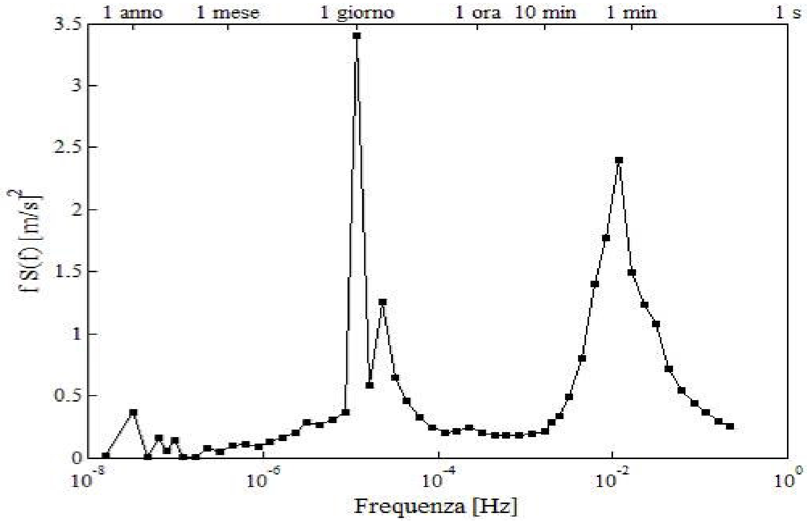

Figure 35: Power spectral density weighted in f for low and high frequency

According to the typical (Van der Hoven, 1957) spectrum there is a spectral gap between 3 hours and 5 minutes. The diurnal peak in the Trento test site is particularly strong due to the presence of thermal promoted wind system like the above mentioned “ora del Garda” which blow regularly in the afternoon and the up-down valley wind system. The turbulent peak is centred on about 1 min and vanishes for periods less then few seconds.

5 MODELLING THE TURBULENCE EFFECT ON POWER CURVES

How discussed in section 2.3, there are several phenomena that interact with the wind turbine, with the anemometer or both and influence the power curves. A lot of these effects are related to the wind turbulence and its interaction on both the machine and the wind measurement. The effects related to the lack of coherence or correlation between the measured wind speed and the effective “driving” wind speed are really of big interest (particularly in high turbulence sites like those in complex terrain or with large distances between anemometer and WT). Unfortunately it is almost impossible to correct the power curve for this kind of effects, only the estimation of the uncertainty on the power curve assessment can be performed to take into account this lack of correlation. This is the reason why great care is given to the anemometers location, the acquisition and averaging time and the site morphology in wind turbine power curve assessment. It is actually the only way to reduce the lack of coherence between the measured wind and the wind that drive the turbine.

This work focuses on the effect of turbulence related to the time averaging operation and the non-linearity of the power curve. An analytical, referred as the Derivative Turbulence Correction model, is proposed and tested on experimental data of the test site of Trento.

5.1 Derivative Turbulence Correction Model – DTCm

In the following dissertation on the derivative turbulence correction model (referred as DTCm for brevity) some hypothesis are made in order to deal only with the effect of turbulence due to the power curve non linearity.

First of all the frozen turbulence is strictly adopted, here we assume that the turbulence structure is unchanged while travelling from the anemometer to the windmill. Furthermore, we will assume that our representative wind speed is somehow measured as an average over an area that is the projection of the area of the rotor onto a plane parallel to the rotor and containing the anemometer. These assumptions practically avoid the above mentioned lack of coherence and rotor extension related issues.

The non linearity of the relationship between the wind speed and the power output of wind turbines is the main analytical cause of the distortion of the power curve in presence of wind speed fluctuation faster than the averaging time.

The Reynolds approach at turbulence is to split the instantaneous *u(t)* velocity in its mean value $\bar{u}$ over a time period *T* and in a fluctuating component *u'*:

$$u(t) = \overline{U} + u'(t) \qquad [5.1.1]$$

As illustrated in chapter 3.3, the variation of the averaging period *T* affects the statistical properties and the meaning of fluctuations. Due to the presence of a spectral gap (Van der Hoven, 1957), a period of several minutes is commonly used in order to separate the wind turbulence from the other low frequency variation.

The turbulent wind speed fluctuations around the mean velocity are not symmetrically transferred in power fluctuations because of the non linearity of the power curve causing variations on the mean power output that depend on the spread of these fluctuations. Let us consider the expression of the power output:

$$P\left(u(t)\right) = \frac{1}{2}\rho A \cdot Cp \cdot u\left(t\right)^3 . \qquad [5.1.2]$$

This expression can be expanded in Taylor series truncated at the second order term around the steady wind speed $\bar{U}$ in order to express the instantaneous power at *u(t)* in function of the fluctuation and the mean wind speed*:*

$$P\left(\overline{U}+u'\right)=P\left(\overline{U}\right)+u'\frac{dP}{du}\left(\overline{U}\right)+\frac{1}{2}u'^2\frac{d^2P}{du^2}\left(\overline{U}\right)+o(u'^2) \qquad [5.1.3]$$

where $P(\bar{U})$ is the power output at the steady wind speed $\bar{U}$. The mean power used for asses the power curve $\overline{P(u)}$ results from the time averaging operation the ten minute period, by applying the average operator on the Taylor expansion we obtain:

$$\overline{P\left(\overline{U}+u'\right)}\cong P\left(\overline{U}\right)+\overline{u'\frac{dP}{du}\left(\overline{U}\right)}+\overline{\frac{1}{2}u'^2\frac{d^2P}{du^2}\left(\overline{U}\right)} \qquad [5.1.4]$$

The second term of the equation is null due to the above definition of the fluctuations whereas the mean of the squared fluctuations $\overline{u'^2}$ is the variance σ_u^2 of the instantaneous wind speed (i.e. equivalent to the variance of the wind fluctuations) in the averaging period *T*. It is important to note that the truncation of the Taylor's series at the second term is particularly efficient considering the Gaussian distribution of the fluctuations over the 10 minute period discussed in section 3.3 (the third moment of a symmetric distribution is zero).

Adjusting the equation[5.1.4], and introducing the expression of the turbulence intensity I_u we obtain the model of the turbulence influence, DTCm:

$$\overline{P\left(u\right)}\cong P\left(\overline{U}\right)\ +\ \frac{1}{2}\ \frac{d^2P}{du^2}\left(\overline{U}\right)\ \left(\overline{U}I_u\right)^2 \qquad [5.1.5]$$

that clearly shows the effect of the turbulence intensity on the power curve.

With this expression it is easy to comprehend the typical distortion effect of the turbulence observed by several authors (Rareshide et al., 2009) (Battisti et al., 2009) (Alberts et al., 2007) (Antoniou et al., 2007) (Kaiser et al., 2007) (Cabezon et al.,

2004) (van Radecke, 2004) (Frandsen et al., 2000) (Albers et al., 1996) (Christensen et al., 1986) and depicted in Figure 36. In fact the power curve has a positive curvature at low – medium speeds and a negative curvature at higher speeds, this lead to a kind of rotating distortion of the power curve in clockwise direction as the turbulence intensity increase. At low wind speed the turbulence increases the power because the positive fluctuations determine a larger amount of instantaneous power than the negatives one. At rated wind speed the positive fluctuation do not vary the instantaneous power output but the negatives one determine a decrease of the mean power output on the averaging period. (Sumner & Masson, 2006) (Sundar & Sullivan, 1983);

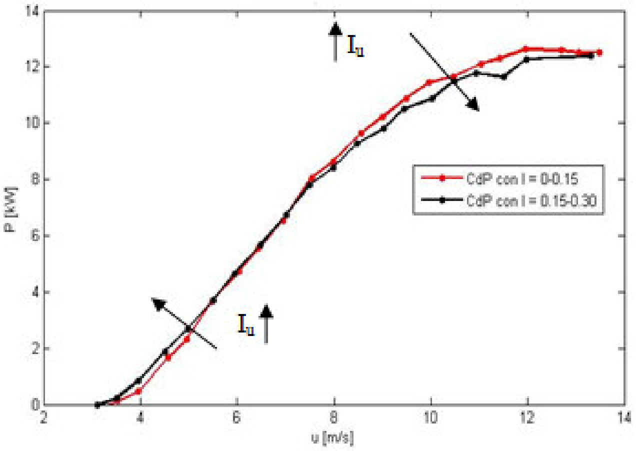

Figure 36: Effect of the turbulence on power curve

The first term of equation[5.1.5] is the mean power output $\overline{P(u)}$ at the velocity *u* in steady condition, without turbulence (and theoretically without all other effects like dynamics, shear, up-flows , etc.). In this situation the instantaneous power and the mean power collapse because the wind speed is constant over the whole period *T*. This kind of steady instantaneous power curve (in the following P_0) can be only assessed by models (with the well known related accuracy issues) or by means of wind tunnel tests. The assessment of the steady power curve in wind tunnel allow the regulation and stabilization of the wind speed and hence is possible to measure the power curve passing by successive steady state and with negligible turbulence intensity. Unfortunately, how pointed out in section 2.1, wind tunnel tests are not always possible, or rather quantitative power curve measurement are difficult.

Going back to the equation[5.1.5], the influence factor of the turbulence intensity for a given mean wind speed $\bar{U}$, on the mean power curve $\overline{P(u)}$ is the second derivative of the steady power curve P_0, so it depends strictly on the (steady) turbine behaviour (rotor aerodynamics, power train efficiency, power control strategy,) and not on the specific site neither on the testing conditions. Summarizing, this model can correct the effect of turbulence by know steady power curve and, obviously, the turbulence intensity. Hence, the estimation of P_0 is a key point on the power curve modelling in turbulent wind.

In the next section a calculation method of P_0 from experimental data is explained whereas in what follow there is a remark on the power coefficient (Cp) curve. Inserting the equation [5.1.2] in equation [5.1.5] we get:

$$\overline{P\left(u\right)} = P_0\left(\bar{u}\right)\cdot\left[1+3I_u^{\ 2}+3\frac{I_u^{\ 2}\bar{U}}{Cp_0}\frac{dCp_0}{du}\left(\bar{U}\right)+\frac{1}{2}\frac{\left(I_u\bar{U}\right)^2}{Cp_0}\frac{d^2Cp_0}{du^2}\left(\bar{U}\right)\right] \quad [5.1.6]$$

where Cp_0 and its derivatives are the power coefficient curve directly related to the zero turbulence power curve (i.e. the P_0 divided by the wind kinetic energy flux through the rotor area for the respective wind speed as in eq. [2.2.3]).

Equation[5.1.6] clearly depicts the importance of the derivatives of Cp_0 curve that determine the well known large error related to the so called u^3 correction (Battisti et al., 2009) (Christensen et al., 1986) that issues from the Cp = constant assumption:

$$\overline{P\left(u\right)} = P_0\left(\bar{u}\right)\cdot\left[1+3I_u^{\ 2}\right] \quad [5.1.7]$$

assumption that is clearly unacceptable for both fixed and variable speed wind turbines, particularly above the rated power where the power coefficient suddenly decrease. The results of Cp constant model is reported in Figure 37 for the data from GaiaWind turbine and compared with the power curves assessed for different turbulence intensity class. It is well rendered the overestimation effect of this model.

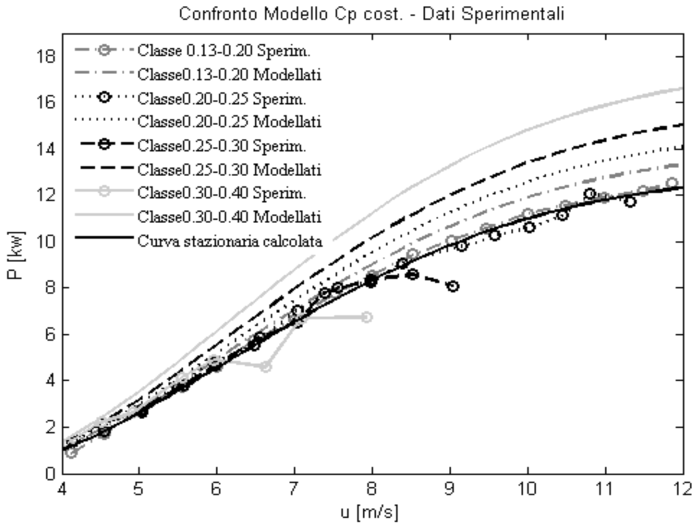

Figure 37: Cp constant model and experimental power curve for different turbulence intensity

5.2 Steady power curve estimation

The computation of the steady power curve from experimental data require almost the same database extension required for the IEC standard procedure, it is also straightforward that the accuracy of the reconstruction grows with the number of samples available for each velocity bin. To obtain an adequate number of data for each turbulence and wind speed class, several weeks or month of acquisition are needed depending on the wind regime of the site.

For small size wind turbines (A < 200m^2), the IEC guideline allows to reduce the averaging time from 10 to 1 minute because of the faster dynamic of the machine and the shorter distance between the anemometer and the turbine.

A remark on the implication of this averaging time reduction is proposed herein: considering the power spectral density diagram (see Figure 35), particular care shall be paid on less than few minute averaging time because of the non stationary of data series (see Figure 38). This, for our analysis, may cause the loss of Gaussianity of wind speed fluctuations on the time interval that is an important assumption of the DTCmodel. Moreover, the turbulence intensity (i.e. the variance) decrease for the effect that the lower frequency turbulences are cut out from the data series (roughly result in mean wind speed variation) and the meaning of the I_u value vanish.

For small wind turbine and standard power curve assessment procedure (i.e. without turbulence correction and following IEC) the power curves at the two different averaging time are more or less equivalent (Battisti et al., 2010). Finally, it is pointed out that the respective wind speed and turbulence intensity data averaged on 1 min are not valid neither for wind speed distribution analysis nor for representative turbulence characterization because the turbulence and the other long time fluctuation are not adequately separated.

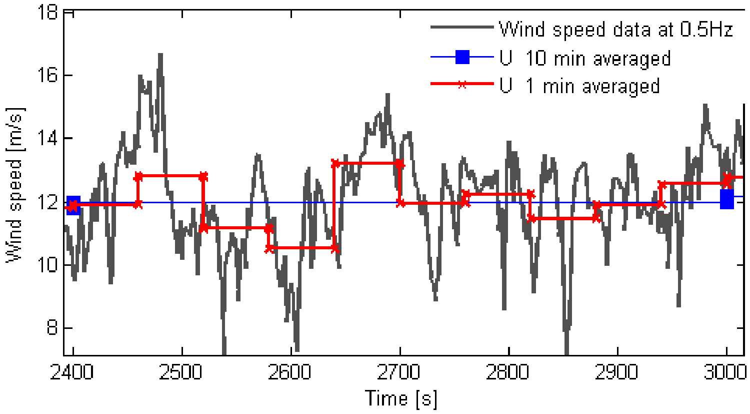

Figure 38: Wind speed time series of 10 minutes and averages

Returning at the steady power curve estimation, the experimental data concerning wind speed, turbulence intensity and power output has to be filtered in order to delete data concerning disturbed sectors, turbine fault and kinematic other compromised data and then has to be normalized according to (IEC 61400-12-1, 2005) guidelines. The turbulence intensity I_u is calculated by its definition eq. [3.3.3]. Hence, at this point, a set of *N* data point of $\overline{P}_i$, $\bar{U}_i$, and $I_{u,i}$ (i=1..*N*) normalized by the appropriate density correction is available.

The steady power curve is estimated by an iterative method starting from the fit of experimental data and, using equation [5.1.5], by converging to a steady stable curve. The initialization stage implies the fitting of the experimental data of power and wind speed (not binned) by a third order polynomial that becomes the first guess for the P_0 curve (i.e. $P_{0,0}$). Kinematic, the data with high turbulence can be excluded from the initialization.

Then, the iterative loop (here indexed with *k*) starts with the analytical computation of the second derivative of the $P_{0,k}$ curve. The correction for the turbulence effect is performed by reversing the equation [5.1.5] for P_0:

$$P_{0,k+1,i}, \left(\overline{U}\right) \cong \overline{P_i} - \frac{1}{2} \frac{d^2 P_{0,k}}{du^2}\left(\overline{U_i}\right) \left(\overline{U_i} I_{u,i}\right)^2 \qquad [5.2.1]$$

each experimental data of $\overline{P_i}$ is corrected using the second derivative of $P_{0,k}$ and the measured turbulence intensity evaluated in $\bar{U}_i$ in order to obtain a set of “steady” power $P_{0,k+1,i}$. This new series of data is fitted by a third order polynomial to evaluate the new guess curve for the steady power curve $P_{0,k+1}$. The successive iteration start deriving this new $P_{0,k}$ curve and goes on. When the difference between the new guess for $P_{0,k+1}$ and the old curve $P_{0,k}$ is small enough, the iterations stop and the new $P_{0,k+1}$ curve is the needed zero turbulence power curve P_0. In Figure 39 the algorithm of the estimation method is outlined.

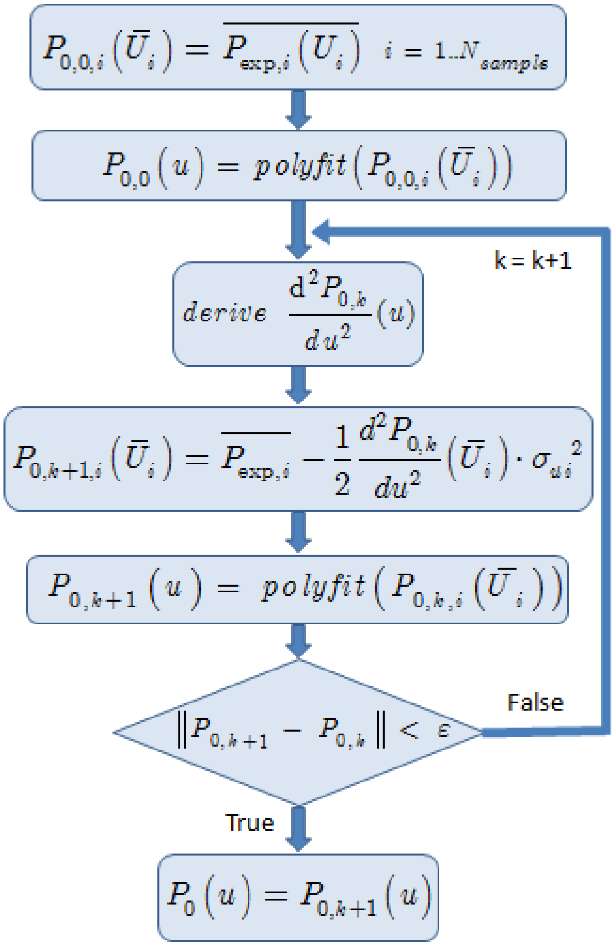

Figure 39: Steady power curve estimation algorithm

The steady power curve is estimated as a polynomial and so is defined for each wind speed and the same goes for the second derivative. The order of the polynomial, as well as the range of speed in which the fit is performed is parameters that influence the steady power curve estimate. The choice of a third order polynomial derives from the theoretical power curves (i.e. a power curve proportional to u^3 if the power coefficient is kept constant) affected by the other three terms for take into account the performance decrease above the rated power and the other variability of the power coefficient in the whole wind speed range. It is expected that the third order polynomial cannot reproduce sharp effects like the cut-in behaviour or the power limitation of an active controlled wind turbine.

However the algorithm proposed can be performed with different order polynomial or with user defined functions. Several opportunities have been investigated during the activity (polynomial, fractional function, exponential, piecewise and discrete function). Some of these options are briefly discussed here in order to evidence possible insight and defect whereas in the next chapter the experimental results are reported and this aspect is treated in depth.

The request of a continuous (and two time derivable) function is due to the second derivative calculation. To obtain a continuous function from a series of disperse data, the fitting procedure is the simplest solution, on the other hand the result is strongly affected by the interval in which the fitting is performed and, obviously, on the function model used.

The application of a narrow wind speed binning of the power curve and the successive computation of the mean power and mean speed inside each bin allow to obtain (for each step of the algorithm) a discrete, high defined, power curve that is not affected by the problem evidenced for the fitting procedure. Unfortunately the application of the finite difference method for the numeric computation of the second derivative lead to an highly irregular curve that is not consistent with the behaviour of the turbine. Moreover, the discretisation coupled with finite difference approach result in a too local representation of the curvature that does not take into account the whole curve.

The most problematic power curve zone to represent is near the cut-in where the discontinuity of the steady power curve, the hysteretic behaviour and the presence of starter systems lead to discontinuous and strongly story dependent behaviour. As will be explained in the next chapter (i.e. with the experimental result), this region of the power curve needs some adjustments. In our approach a local fitting is performed at cut-in and matched with the whole steady curve as will be more clear in the experimental section.

6 EXPERIMENTAL RESULTS

The data acquired at the Trento test site are firstly used for the standard assessment of the power curve and then applied on the steady curve estimation algorithm for achieving the steady power curve. The efficiency of the correction model is then verified and further improvements are suggested. Finally the performances of the correction on energy forecasting are compared with the standards and with the power meter one different period of experimental data of wind and turbulence intensity.

The power curve modelling has been carried out only on the GaiaWind turbine data whereas the standard power curve is presented for both the mini wind turbine on the site. This choice is mainly due to the fact that the Jimp20 turbine installed at TN site showed an unusual behaviour near the rated power due to the pitch actuation that seemed to not work properly as evidenced in power curve and time series analysis.

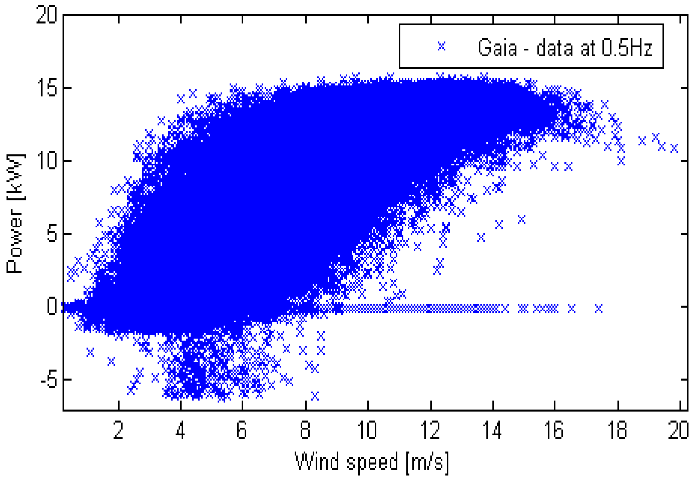

Figure 40: Power VS wind speed raw data at 0.5Hz - GaiaWind - 29 days

6.1 Standard power curve assessment at TN site

The (IEC 61400-12-1, 2005) procedure explained in section 2.2 was applied at experimental data regarding the GaiaWind turbine and the Jimp20. For the first wind turbine only a month (February 2008) of data were available for reason regarding the database and the power calculation whereas for the Jimp20 one year of data were employed (August 2007- August 2008).

In Figure 40 the data of power and wind speed acquired at 0.5Hz are reported in order to evidence the dispersion of those measures. The averaging operation over 1 minute and the following data selection, lead to the data in Figure 41.

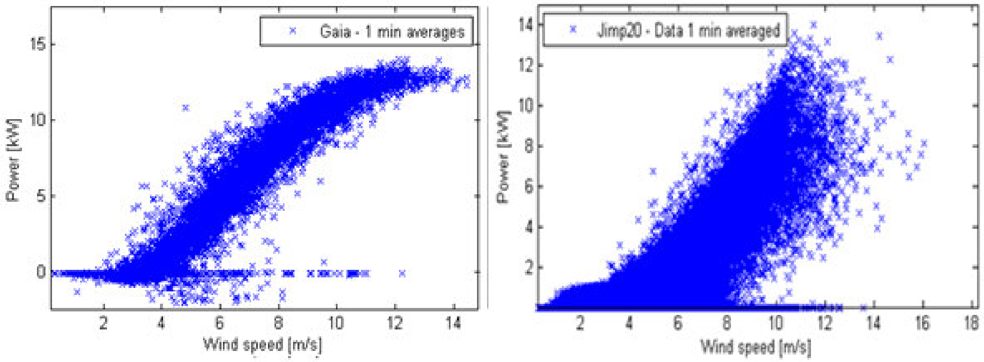

Figure 41: Power VS wind speed normalized data averaged on 1minute - Gaia and Jimp turbines

For both wind turbines the data in which the wind blew from shadowed sector were rejected. Those sectors are respectively from 272° to 346° for GaiaWind mast and from 65° to 139° for the Jimp20 mast.

The selected data were normalized at the standard density following: the power normalization for the GaiaWind turbine (fixed speed stall regulated), and wind speed normalization for the Jimp20 (active power control).

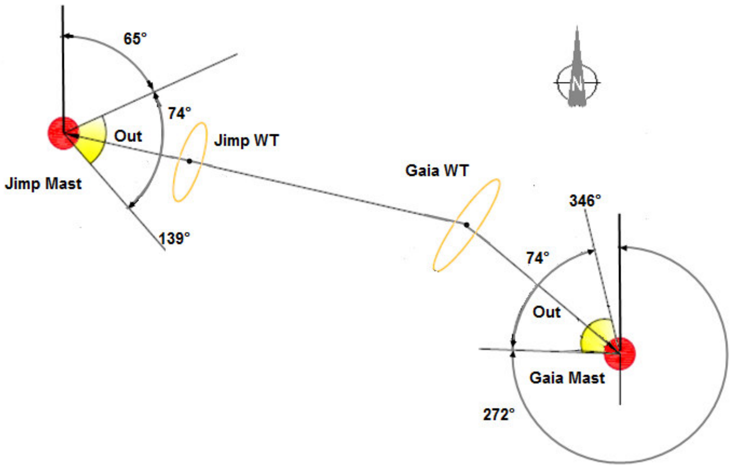

Figure 42: Rejected sector for shadowing effect at TN site

The data were divided in wind speed bin with a range of 0.5 m/s. The mean values of wind speed and power output was computed for each valid bin (i.e. with more than 10 points) obtaining the standard measured power curve.

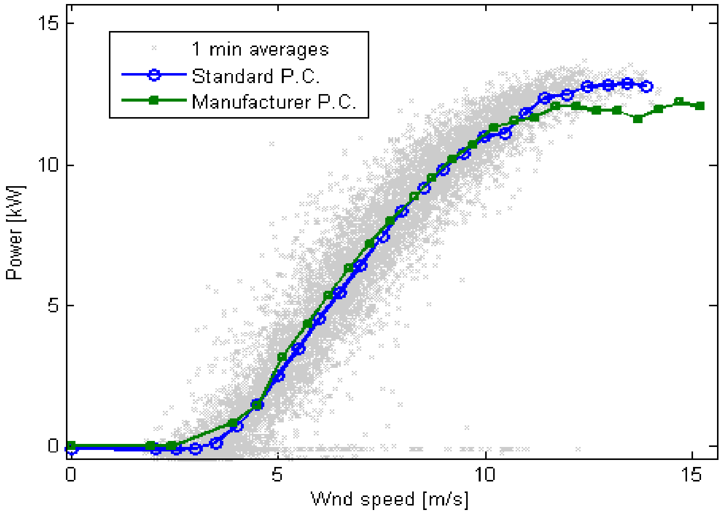

Figure 43: Standard power curve of GaiaWind turbine measured at TN site

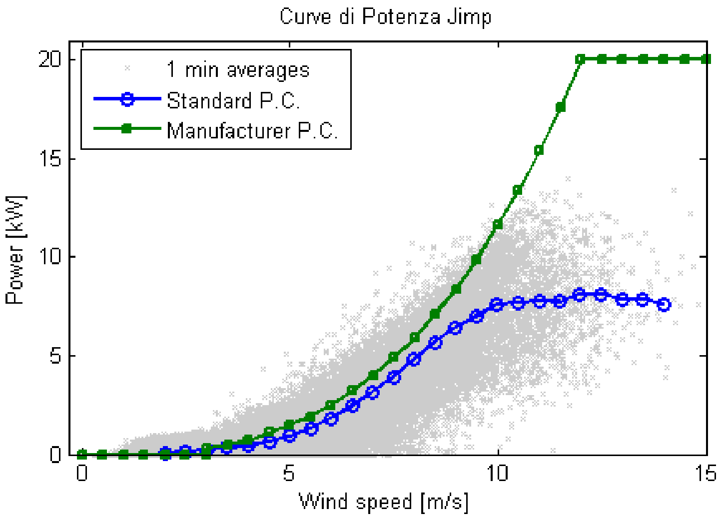

Figure 44: Standard power curve of Jimp20 wind turbine measured at TN site

In Figure 43, the measured standard power curve of the GaiaWind turbine is reported along with the power curve from the manufacturer datasheet. The two curves are only slightly different in the low-medium wind speed. At rated power the measured power curves at TN is higher than the declared power curve whereas for higher velocities there are no data. Considering that the power regulation of this WT is passively determined by the progressive stall of the rotor, the standard power curve seems to stall at a wind speed slightly higher than the claimed one. However, an exhaustive analysis of this behaviour requires more data at higher wind speeds that are not available (furthermore it is not on the aim of this work the investigation of the stall behaviour).

The above power regulation problem mentioned for the Jimp20 wind turbine is clearly shown in Figure 44. The power curve stated by the manufacturer is far from the measured power curve at TN site. Recent analysis on the pitch actuation reveals an over-regulation of the pitch control that rotate the blade very fast in order to regulate at rated power but, when the power decreases and the rotor slow down, it regulates very slow leading to an important loss of power (i.e. energy).

Finally the power coefficient measured for the two wind turbines are reported in Figure 45 along with the stated Cp.

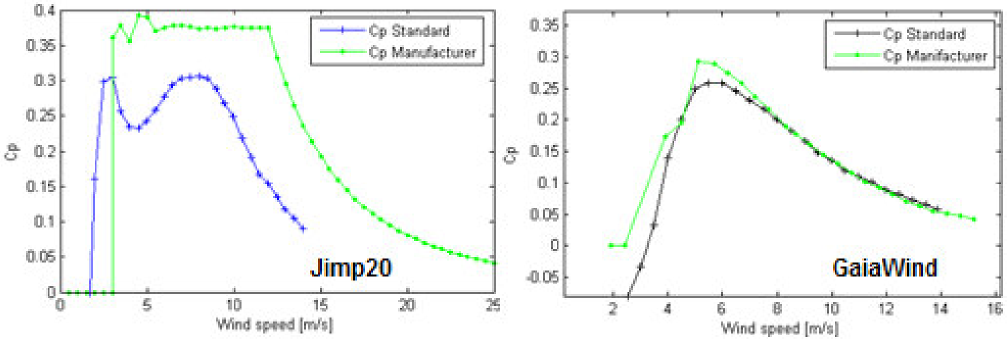

Figure 45: Standard power coefficient measured at TN

The power coefficient is clearly not constant neither for the variable speed pitch regulated WT nor for the fixed speed passive stall WT. Only the variable speed wind turbine, theoretically, works at an almost fixed Cp below the rated power.

In following the power curve of GaiaWind assessed using an averaging time of 10 minute (how indicated for non-small wind turbine) is reported for a comparison with the 1min power curve.

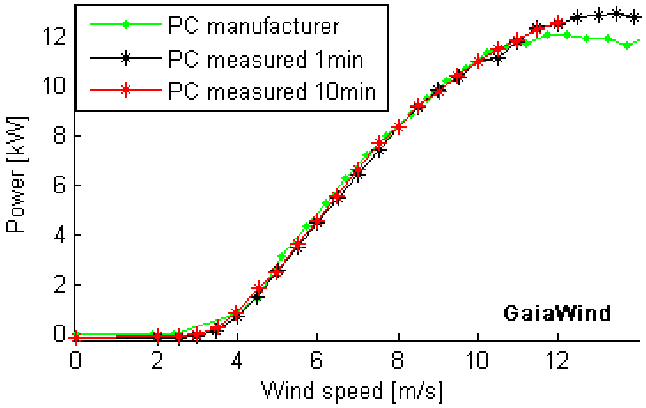

Figure 46: GaiaWind power curve with 1minute and 10 minute averaged data.

The comparison on Figure 46 reveals that the power curves assessed with 1 minute and at 10 minute averages for the GaiaWind turbine are almost equivalent. This is due to the low inertia of the rotor and the power train and to the relatively small distance between anemometer and wind turbine that allow to reduce the averaging time without great lack of correlation problems. However, for low wind speed is perceptible a small difference, evidenced in the Cp graph, probably due to the effect of the turbulence that lead to an overestimation of the power production at lower wind speed (how explained above, a portion of the turbulence peak is considered a power fluctuation on 1minute average whereas for 10 minute all the turbulent fluctuation are occulted on the averaging period).

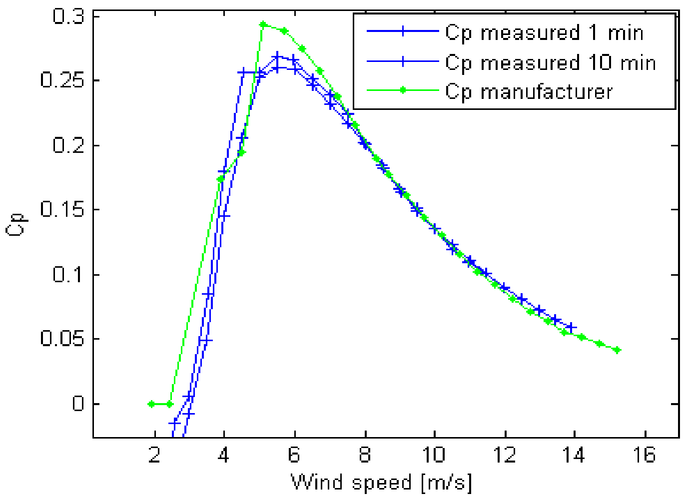

Figure 47: GaiaWind Cp measured with 1 min and 10 min averaged data

6.2 Turbulence modelling via DTCm at TN site

The derivative turbulence correction model discussed in chapter 5 is now applied to the data regarding GaiaWind turbine in order to reconstruct the steady power curve of that machine and to verify the validity of the correction model.

Before starting with the model, a quantitative discussion of the turbulence effects on the power curves of the two turbines present at the Trento site is helpful. The data becoming from both GaiaWind and Jimp20, averaged on 10 minute intervals are divided on turbulence classes and then, the standard power curve are estimated like in standard power curve assessment. For this kind of analysis the time period in which the data are averaged is 10 minute in order to respect the hypothesis of stationarity and considering the width of the spectral gap in the site (see Figure 35). The turbulence intensity is calculated as the ratio between the standard deviation of the 0.5Hz sampled wind speed in the 10 minute period and the mean wind speed. In Figure 48 the power curves of GaiaWind for six class of turbulence intensity are reported. The distortion effect of the turbulence is clearly visible between 8 and 12 m/s where the power curve at increasing turbulence intensity decreases.

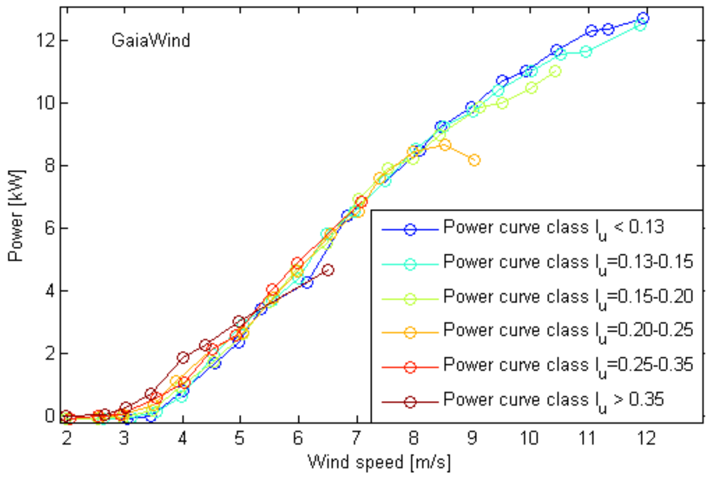

Figure 48: Gaia measured power curve for different class of Turbulence Intensity

Unfortunately the data collected near the rated wind speed are not enough to see this effect for all the turbulence classes. At low wind speed the turbulence determines an improvement of the mean power output as evidenced by the zoom of Figure 49.

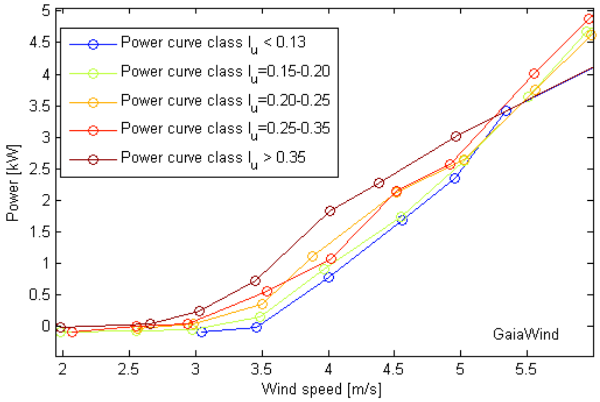

Figure 49: Zoom of the low wind speed region of PC at different I_u

The same intensity class division of the power curve for the turbine Jimp20 is reported in Figure 50, almost the same behaviour can be observed at low wind speed whereas at higher wind speed the interaction of the fluctuations with the anomalous pitch control behaviour leads to a strong decrease of the power output.

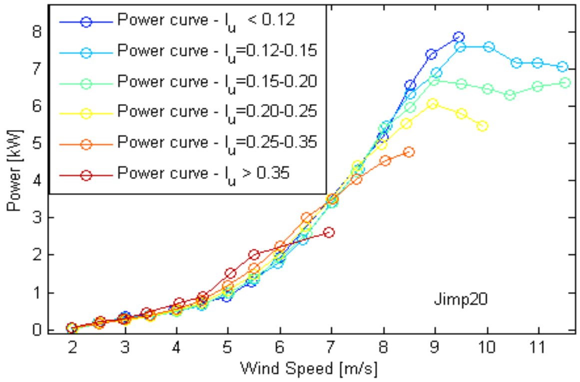

Figure 50: Jimp20 measured power curve for different class of Turbulence Intensity

The steady power curve estimation, performed for GaiaWind turbine, uses the same 10 minute averaged data of the previous elaboration. The wind speed, turbulence intensity and power output are filtered to reject shadowed sectors and invalid data. The first step, reported in the left side of Figure 51 ,is the estimation of a first guess for the steady power curve by fitting the wind speed and power output data through a polynomial. The fit is performed by the least square method in the velocity range between low cut-in and the maximum available wind speed.

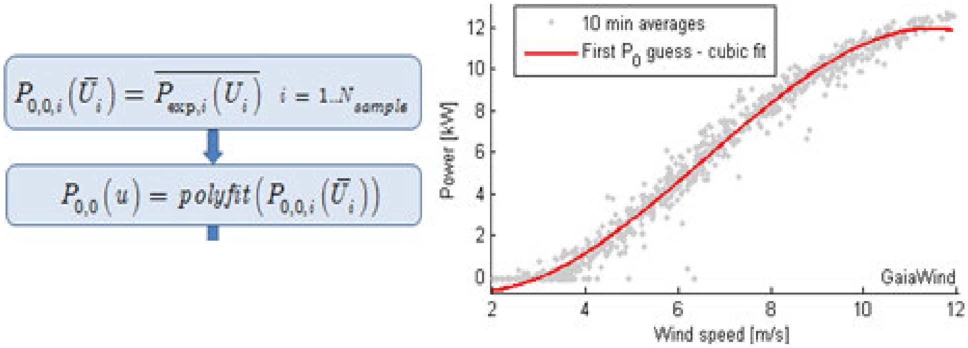

Figure 51: First step - fitting of the experimental data

Naturally the velocity range and the fitting model influence in a strong way the results. The second derivative of the fitted expression can be easily calculated in analytical form obtaining the correction factor for the turbulence correction in function of the wind speed. By applying the [6.2.1] at each 10 minute measured data a new set of power output corrected for turbulence effect is computed. This new set of data represents the new guess for the steady power versus wind data set.

$$P_{0,k+1,i'}\left(\overline{U}\right) \cong \overline{P_i} - \frac{1}{2}\,\frac{d^2P_{0,k}}{du^2}\left(\overline{U_i}\right)\,\left(\overline{U_i}I_{u,i}\right)^2 \qquad [6.2.1]$$

In Figure 52 this new data set for the first iterative step is reported along with the successive fit of the data that is the new guess for the steady power curve.

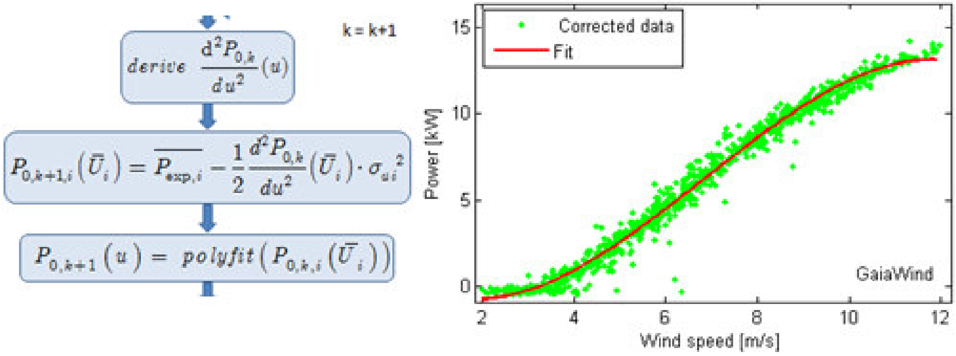

Figure 52: First iteration step result - steady data and steady fit

This new steady power curve is used for a new iteration and the loop continues until the new steady curve converges to a definitive steady power curve. In practice this is valued by the norm of the difference between the new steady curve and the previous one. After a few iterations, typically 3-5, the power curve converges to the steady power curve exposed in Figure 53 along with the standard power curve and the experimental dat

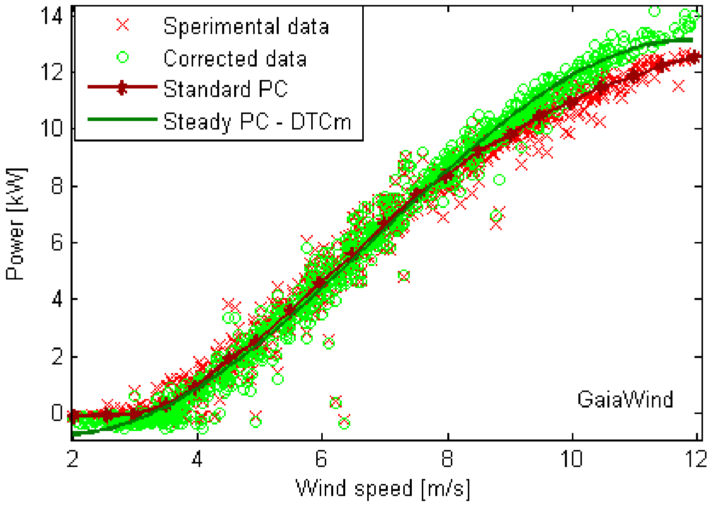

Figure 53: Estimated steady power curve by DTCmodel

So, an estimation of the power curve at zero turbulence intensity is available as a function of the wind speed, in the case just explained it is modelled by a cubic polynomial.

In order to verify the consistence of the turbulence effect modelling through Derivative Turbulence Correction model, the experimental data acquired at the Trento site and separated in different turbulence class are compared with the modelled power curve at the mean turbulence intensity of each class. The results are shown in Figure 54; power curves at increasing turbulence class are shifted down by 1 kW for clarity

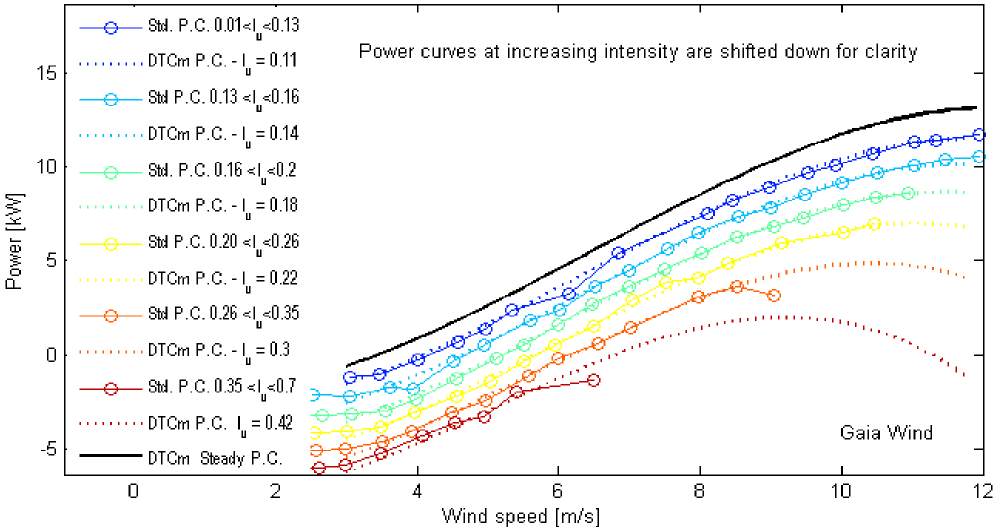

Figure 54: Comparison of DTCm predicted power curves and measured power curves at different turbulence intensity class

For the wind speeds between the cut-in and the velocity where data are available the DTCm nearly overlaps the measured power curve at different turbulence intensity. This results show that the DTCm well represent the effect of turbulence, at least for the velocity and turbulence range available in the steady curve estimation procedure. By observing the correction proposed by the model for high turbulence and medium-high wind speed it is clear that it is maybe a too strong decrease and the same happens for high wind speed. Moreover it is noted that, at near cut in wind speed, the power curve is almost straight and so the second derivative correction is almost null. The cut-in zone that is strongly affected by hysteresis and secondary effects need a particular attention in order to model in a correct way the “mean” performance of the wind turbine at these wind speeds. In this work we propose a local fit of the low turbulence data at near cut-in (cut-in ± 1m/s) with a cubic polynomial that match the overall steady power curve at cut-in plus 1m/s. This local almost steady power curve allows for an effective correction for data near cut-in. It is fundamental to understand that this is not important just for data at cut-in or lower where the power are very low but is very meaningful for higher wind speed. For example at 3.8 m/s, where the locally fitted power curve and the whole steady power curves gives fairly the same power at zero turbulence (about 0.4 kW), the correction effect of the whole steady curve is negligible (the steady curve is almost straight) whereas, considering the curvature of the standard power curve a conspicuous increase of power output may be obtained in turbulent wind because the negative fluctuations of wind speed down to about 3.5 m/s do not determine a decrease of power output, or nothing compared to the effect of the symmetric positive wind fluctuations. This concept is emphasized in Figure 55.

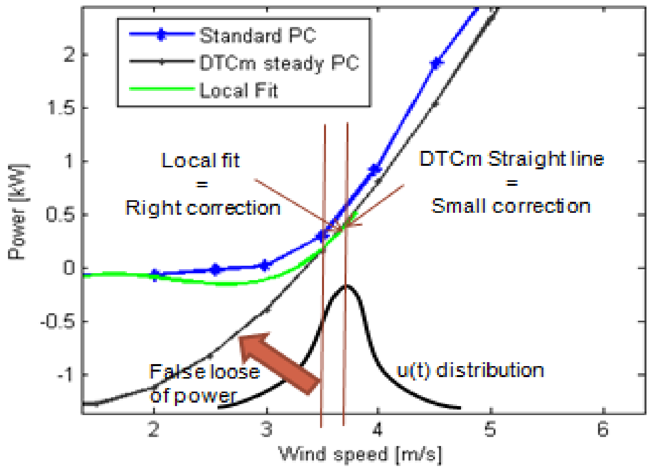

Figure 55: Local fit correction on the DTCm at Cut-in wind speed

Finally, in order to complete the steady power curve between zero and cut –in, the power at this velocity is fixed to the measured power consumption with the machine stopped. The so corrected steady power curve estimated for GaiaWind is reported in Figure 56.

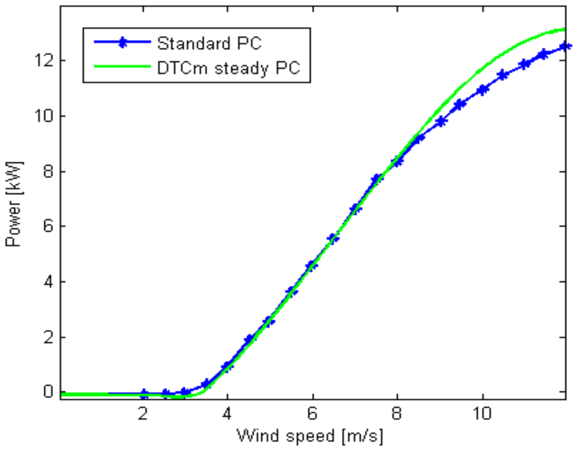

Figure 56: DTCm final steady power curve for GaiaWind turbine

With the aim of verify the performance of the model on energy production estimation another elaboration is explained. The DTCm with the estimated steady power curve is coupled with real wind speed and turbulence intensity data to estimate the energy produced by the turbine. Three long periods of wind data acquired at TN site from the Gaia mast at 18m height are used for the energy estimation choosing period where both the turbine and the anemometer were operating without fault or loss of data. The sets of data are composed by 10 min averaged wind speed, density and wind speed standard deviation that are inserted in the formula of the Derivative Turbulence Correction model along with the estimated steady power curve:

$$\overline{P(u)} \cong P_0\left(\overline{U}\right) + \frac{1}{2}\,\frac{d^2P_0}{du^2}\left(\overline{U}\right)\,\left(\sigma_u\right)^2 \qquad [6.2.2]$$

the mean power output multiplied for the time interval (600s) gives the energy converted by the WECs in the single ten minute period and theirs summation over the whole lapse is the total energy converted. This value is compared with the energy consumption registered on the power meter in the same period. For completeness the predicted value calculated using the standard power curve and the declared power curve are reported.

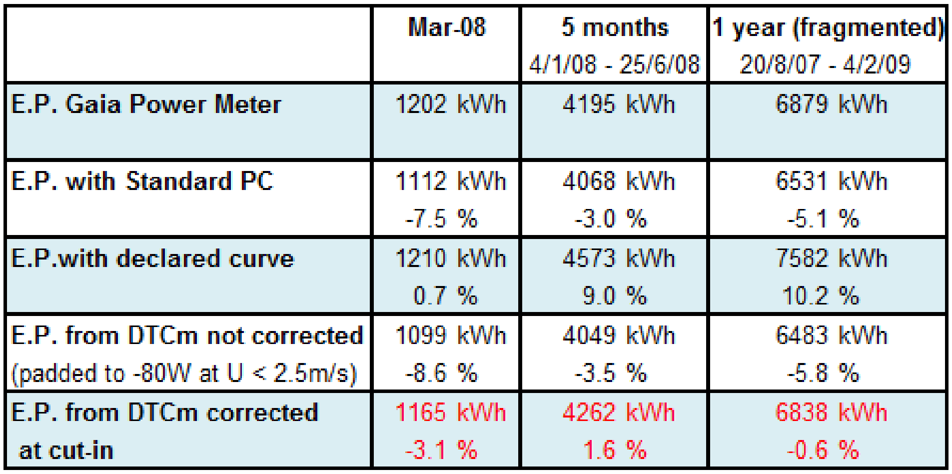

	Mar-08	5 months 4/1/08 - 25/6/08	1 year (fragmented) 20/8/07 - 4/2/09
E.P. Gaia Power Meter	1202 kWh	4195 kWh	6879 kWh
E.P. with Standard PC	1112 kWh -7.5 %	4068 kWh -3.0 %	6531 kWh -5.1 %
E.P.with declared curve	1210 kWh 0.7 %	4573 kWh 9.0 %	7582 kWh 10.2 %
E.P. from DTCm not corrected (padded to -80W at U < 2.5m/s)	1099 kWh -8.6 %	4049 kWh -3.5 %	6483 kWh -5.8 %
E.P. from DTCm corrected at cut-in	1165 kWh -3.1 %	4262 kWh 1.6 %	6838 kWh -0.6 %

Table 2: Comparison of predicted and measured produced energy

In Table 2 the deviations from the measured value of the energy converted by GaiaWind during the period of time reported in the header, are reported along with the absolute value of the active energy estimation. The standard power curve without correction for the turbulence intensity underestimates the energy production for all the three tests reaching a deviation always less than 8%. On the other hand the estimation performed with the power curve declared by the manufacturer overestimate the production reaching a 10.2% error. The estimation performed with the Derivative Turbulence Correction model without correction on the cut-in region but only with the imposition of self-consumption power (-80W) at low wind speed (minor than 2.5m/s) underestimate the production, mainly for the effect explained above. Finally the DTCm with correction on cut-in wind speeds allows to predict the energy production with less the 3.5% error and, more importantly, do not show a systematic under or over estimation of the production and so seems to well represent the behaviour of the wind energy converter in turbulent wind.

It is pointed out that, in energy forecasting, an uncertainty on the annual energy prevision of about 10 per cent points (at 95% percentile) is typical especially in low wind sites mainly because of the uncertainties related to wind speed measurements which are the main sources of error due to the error propagation. A 2% error of the velocity measurements is reflected in a 6% error in the power evaluation, and this appears to be an intrinsic threshold. This poses the question of whether the more and more sophisticated literature techniques are really relevant to obtain more and more accurate power prediction; the increased accuracy lies within the unavoidable experimental error, leading to an apparently fictitious advantage that cannot actually be quantified in a meaningful way.

However, the effort of the turbulence on the energy production is resulted strongly dependent on the mean wind of the site, on the steady power curve and obviously on the turbulence intensity. For small wind turbines located in turbulent condition (low height) and in low wind site the influence of the turbulence intensity may be more conspicuous especially if the curvature of the power curve in the region of the mean wind speed of the site is strong.

Moreover, a correct modelling of the influence of the turbulence on the power curve allows to correct the measured power curve achieving the steady power curve that, as a characteristic of the WT, can be used for comparison with other machine or for a comparison of the same turbine in order to individuate possible malfunctioning.

7 CONCLUSIONS – PART 1

In this first part the modelling of the effect of the atmospheric turbulence on the power curve for wind turbines was carried out. After a discussion on the meaning of power curve and the meaning of virtual wind speed, the standard procedure for power curves assessment was explained.

In section 2.3 the main factors that influence the power curve were discussed to achieve power performance measurements through infield tests. Specific remarks regarding the small wind turbines were also added in these discussions.

In chapter 3 the attention was focused on turbulence and on the atmospheric boundary layer. The turbulent fluctuations were treated by the Reynolds approach and the frozen turbulence assumption was adopted. The mathematical and numerical instruments for turbulence characterization were explained in section 3.4 along with the coherence models useful to evaluate the representativeness of measured wind speeds. The power spectrum is also presented and the importance of the spectral gap for separating wind turbulence from synoptical and diurnal wind speed fluctuations was emphasized. Moreover a discussion of the stationarity and Gaussianity of the wind fluctuations in the 10 minute averaging period is discussed at depth.

In chapter 4 the Trento test site for small wind turbines was described along with the installed turbines and the data acquisition system. The wind regime of the area was characterized. Wind data revealed a low wind site with a mean wind speed of 2.75 m/s and a 24% of representative turbulence intensity.

In chapter 5 the Derivative Turbulence Correction model was developed starting from the Reynolds expression of the instantaneous wind speed and making use of a Taylor expansion around the instantaneous steady power curve. The model is based on the concept of the zero-turbulence steady power curve that allows to evaluate the effect of the turbulence intensity on the power output of the turbine. Then a procedure for estimating this fundamental steady power curve from experimental data was described. The steady power curve estimation is based on a recursive application of the turbulence correction on raw data, capable of converging in 3-4 iterations to the accurate estimation of the steady power curve.

In chapter 6 the data regarding wind speed, wind direction and power output of the GaiaWind turbine collected at the Trento test site were firstly employed for the assessment of the standard power curve and then used for the estimation of the steady power curve for the DTCm. The estimated steady power curve was coupled with the Derivative Turbulence Correction model to calculate the power curve at different turbulence intensity. The comparison of these power curves with the experimental power curves computed for class of turbulence intensity proved the validity of the model. Nevertheless some corrections are required at cut-in wind speeds where the hysteretic behaviour of the machine is not easily captured by the DTCm model.

Finally, the power curves available for the GaiaWind turbine that are: the claimed power curve, the standard power curve computed at the Trento site and the DTCm coupled with the estimated steady power curve were compared in terms of energy production forecasting. The model proposed performed three estimations with errors always less than 3.2% and without systematic errors. The claimed power curves always overestimated the power production (maximum error 10%) whereas the standard power curves performed three underestimations (maximum error -7.5%).

These results confirm the validity of the Derivative Turbulence Correction model to represent the effect of the turbulence on the power curve.

However the role of the turbulence in the annual energy production is not always of real concern but is strongly dependent on the site the turbine operates in and on the power curve of the turbine. For application on small wind turbines operating in low wind sites with turbulent winds, the correction seems to be meaningful.

8 ROUNDNESS MEASUREMENT AND SHAPE RECONSTRUCTION

In cylindrical shapes measurement, when there is the possibility to measure the piece with a Coordinate Measuring Machine, the shape of the body can be reconstructed with high precision and the roundness, the cylindricity and the axis deviation may be evaluated by successive elaboration of the mesh.

For properties like concentricity, coaxiality and run-out, that need a reference element, also the datum feature as to be measure (Gapinski, 2006) (ISO/TS 15530-4:2008, 2008) (ISO 4292-1985, 1985). Unfortunately, this type of measurements can be performed almost only off-line and for mechanical parts with appropriate dimensions. The application of multiple stereo vision systems for shape reconstruction (De Cecco et al., 2010) allows reconstructing the surface of bodies, evenly on movement, by means of couples of high resolution cameras. Despite the great improvements of the performances of this systems during the last few year, the accuracy available and the need of marked (or patterned) surfaces still limits theirs application in industrial mechanics.

Moreover, there are many applications like grinding machines for rolling mill cylinders (Nyberg, 1993), taper turning active spindle error compensation (Fung & Yang, 2001), high density recording media (Okuyama et al., 2007), to mention just a few, where the measurement is part of a control loop and therefore must be performed on-line. Finally, there are applications where the quasi-rotational motion of the cylindrical body is the main interesting object and the external shape is only a disturbance. For these applications, the component must be measured while rotating around an axis imposed by the motion system. One main difference with the static methods is that the piece, while being measured, undergoes a 3D motion. Let us think about a raw steel bar while is rotating on a lathe, driven by the spindle; the bar has an irregular surface and its axis may be not straight, moreover the nominal axis of the cylinder may be different from the rotation axis imposed by the spindle (in orientation and position) and, because of vibration the same rotation axis may has a 3D roto-translation motion on the space. This is the most general situation in which the rough cylinder is rotating and moving in a complex way, usually some of this motion are negligible but, by now, this general situation as to be remembered.

The three-point method for roundness detection (Aoki, 1966) (Kato, 1990) (Mitsui, 1982) (Li & Li, 1996)is commonly used to separate the influence of spindle axis motion in the cross section from shape circularity/roundness. It consists on an evolution of the calliper system that allow to measure simultaneously three radial displacement of the surface (instead of two) (Adamczak et al., 2006)of, theoretically, the same cross section. One of its main requirements is also that each proximity sensor axis lies on the same cross section. Unfortunately this is not the case in reality. Cylinder's motion, shape, probes positioning have a general 3D structure.

This in turn can have a strong effect on the roundness estimation affecting its accuracy and therefore placing strong requirements of geometric precision to the whole mechanical setup. In order to assess accuracy and the error budget for the design, some studies that exploit computer simulation of the measurement chain taking into account influencing factors can be found in the literature. In (Gao et al., 1996) (Gao & Kiyono, 1997) (Tu et al., 1997) (Chin, 2005) only the 2D structure of cylinder/holes cross sections and displacements are taken into consideration. In (Nyberg, 1993) are taken into consideration roundness deviation, moment of inertia distribution, thickness variation, radial error motion, straightness deviation, cylinder shape, sensors inaccuracy in placement and noise. The simulation of the different effects is not described/considered in true 3D form. Sensors' placement inaccuracy is modelled only as a deviation with respect to their nominal position in-plane and along the cylinder axis, but not as a function of the five parameters that an axis in space actually has. The motion of each end of the cylinder is considered only to estimate the effect of the in-plane motion of each cross section along the cylinder axis.

In (Endo, 2003) the general 3D deviations of cylinder motion and sensors axes are taken into consideration to develop a new method that uses five probes on a spiral line across the cylinder. Probes axes deviations are supposed to be small in order to achieve a simpler mathematical form and no simulation method is shown or discussed.

As a matter of fact, none of the above mentioned references show a method able to consider the general 3D structure of the phenomena. The cylinder, while rotating, can bear a combined translational and rotational motion, either periodical or not. Each Probe axis has a nominal displacement on the measurement plane plus a deviation that shall be described by means of three translational parameters and two rotational ones. While the cylinder rotates each sensor measures a distance from the surface that belongs to different cross sections that do not correspond each other. The resulting roundness estimate, although in absence of transducers noise, is different from each section belonging to the cylinder coming out from the contribution of all the cross sections under the probes field of view. This clearly leads to a deviation from the ideal case where each sensor measures distances on the same cross-section, that is generally non negligible.

To assess the effects due to the contribution of all the degrees of freedom participating in the measurement procedure a method able to estimate the sensors' output and comparison criteria for the estimated out-of-roundness shape has been developed (Miori et al., 2009) .

The method makes use of a mathematical description of the cylinder's parameters that describe its shape via DFT decomposition of its cross section and as a function of its nominal axis. The centre of each cross section can deviate from its nominal axis. Each degree of freedom of the sensors' axes describing the actual probes mounting can be defined in a parametric form.

The numerical modelling of the entire system can be divided into three principal parts:

- Surface and Axis Modelling
- Motion Modelling
- Measurement System Modelling

9 PARAMETRIC CYLINDER MODEL

The main actor of a measurement process is obviously the measurand that in this case is the distance between the surface and the reference axis and so the surface modelling is the first task to overcome. In this part the geometrical model of the cylinder is discussed step by step.

Before proceeding, it is worth to explain the notations used in this dissertation. It is important to note that the method proposed to model the cylindrical shape, to simulate the radius measurement and to successively reconstruct the shape from measurement are suitable for different applications whereas for the motion and measurement system modelling I focused on rolling mill cylinders grinding machines.

The cylinder coordinate system $\{O_c\, X_c\, Y_c\, Z_c\}$ is a local coordinate system attached to the cylinder in which the shape of the body is described. The origin O_c is located in the plane of the first cross section of the body of the cylinder along with the X_c and Y_c axes and in the point defined by the intersection of this plane with the line that connects the centres of the two neck's section that is the Z_c axis.

How depicted in Figure 57, the cylinder is hold by four supports on his roll necks while the spindle commands the rotation theta. The supports and the necks near the spindle are referred as front ones and the others as back ones.

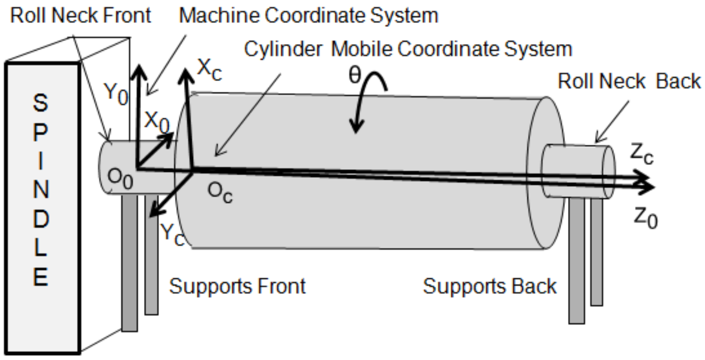

Figure 57: Coordinate Systems and Notations

The machine coordinate system $\{O_0X_0Y_0Z_0\}$ is the absolute reference system. The origin O_0 is exactly on the centre of a circle (with the nominal radius of the neck) lying on the mid section of the front supports. The Z_0 axis point on the same nominal circle putted on the back supports whereas the X_0 axis is defined as an horizontal axis perpendicular to Z_0 and Y_0 is consequently determined. The cross sections in what follow are taken by a point of view placed in the back side of the cylinder (so at the right side of Figure 57) and facing the spindle.

9.1 **Surface and axis modelling**

The surface of the cylinder is described through a series of cross section boundaries and their eccentricity (i.e. the position of the centre of the cross section in the X_cY_c plane). In Figure 58 a generic cross section at $Z_c = z_i$ is reported along with the coordinate that describes the boundary in the cylinder coordinate system. The eccentricity of each cross section represents the straightness deviation of the axis of the cylinder. This axis deviation is expressed in polar coordinate $[C_0, \phi_{c0}]$.

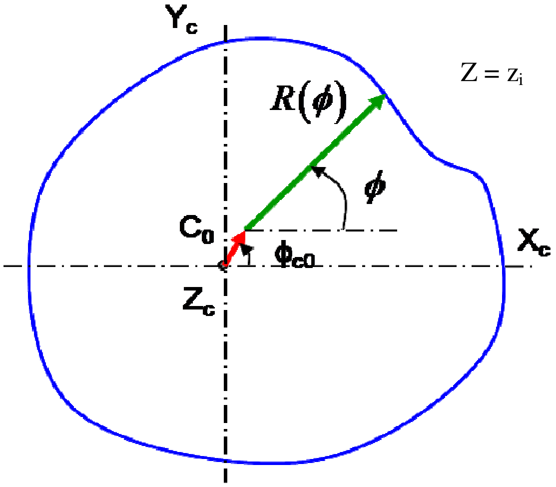

Figure 58: Cross section -shape and axis deviation definition

The boundary of each cross section, abbreviated in cross section in what follows, is also described in polar coordinate [R ,ϕ]. The nature of the problem of describing the radius of a nearly–circular boundary suggests the use of periodic function. Hence, the radius R is modelled by discrete Fourier series in ϕ that is the angle from the X_c axis (see Figure 58). The function $R(\phi)$ in the generic section z_i is expressed by eq. [9.1.1] where the dependence on z will be more clear in the next.

$$R(\phi,z) = R_0(z) + \sum_{a=1}^{n}\left(R_a(z)\cos\left(a\cdot\phi + \phi_a(z)\right)\right) \tag{9.1.1}$$

Here, the mean radius of the section is expressed by R_0 whereas R_a is the amplitude of the a harmonic and ϕ_a is the phase angle of the respective harmonic.

With this formulation, for example, it is possible to describe lobed circles giving a non-zero value only to the correspondent harmonic (R_a). Varying the values given to all the harmonics and their phases it is possible to represent a wide range of circular shapes depending on the number of harmonics inserted n. It is interesting to note that, in order to describe a profile centred on the origin of [R ,ϕ] coordinate system, the first harmonic must be set to zero. So in this work the first harmonic is always null.

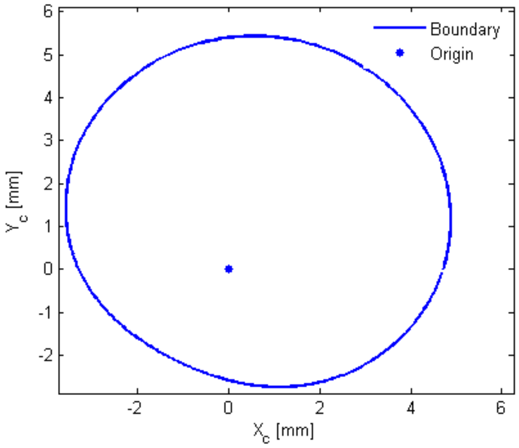

Figure 59: Section modelled with the first harmonic not-null

To completely represent one cross section it is necessary to define two parameters for the axis deviation [C_0 ,ϕ_{c0}], one for the mean radius [R_0] and two parameters for each harmonic [R_1, ϕ_1 , R_2, ϕ_2. . . R_a, ϕ_a , . . . R_n, ϕ_n]. This set of parameters is theoretically required for each cross section in which the cylinder is discretized.

In order to reduce the number of parameters needed to describe the whole cylinder and to easily permit the representation of smooth surfaces, each parameter [C_0 ,ϕ_{c0}, R_0, R_a, ϕ_a] is modelled by an appropriate function of the Z_c coordinate.

The mean radius of the sections is modelled by equation [9.1.2] giving the possibility to easily represent barrel-shaped rolls, or other classic cylinders shape.

$$R_0\left(z\right) = R_N + A_{Ro} \cdot \cos\left(\frac{z}{Z_{tot}} \cdot B_{Ro} \cdot \pi + C_{Ro}\right) \qquad [9.1.2]$$

Where z is the longitudinal position of the section, Z_{tot} is the length of the cylinder and the parameters are the nominal radius R_n, the amplitude of the variation A_{R0} and other two parameters, B_{Ro} and C_{Ro}, that characterize the fluctuation of the function along the longitudinal dimension of the cylinder.

.

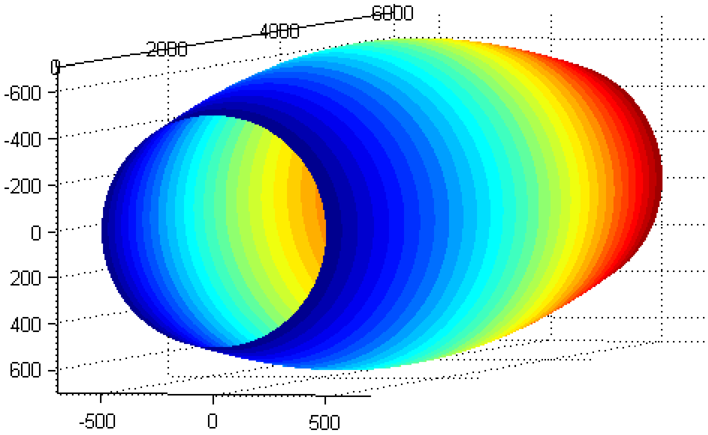

Figure 60: Barrel shaped cylinder surface

The set of harmonics R_a is modelled by equation [9.1.3] by setting the parameters A_{Ra}, B_{Ra}, and C_{Ra} for each of the n harmonic represented.

$$R_a\left(z\right) = A_{Ra} \cdot \left(\cos\left(\frac{z}{Z_{tot}} \cdot B_{Ra} \cdot \pi + C_{Ra}\right)\right)^2 \tag{9.1.3}$$

Where A_{Ra} is the maximum amplitude of the a harmonic and the other two parameters characterize the shape of the function. The square operation is only to avoid negative values that influence the phase of the harmonic by adding 180 degrees. Moreover the phase of each harmonic is modelled by equation [9.1.4] giving the possibility to easily represent, for example, twisted rolls setting only the three parameters D_a, DD_a and E_a for each harmonic.

$$\phi_a\left(z\right)=D_a \cdot \left|2 \cdot \frac{z}{Z_{tot}} - E_a\right| + DD_a \tag{9.1.4}$$

In practice the parameter D_a define the rate of variation of the phase ϕ_a whereas the parameter E_a the inversion point of this variation. In Figure 61 a twisted cylinder with an hexa-lobed section is plotted as an example.

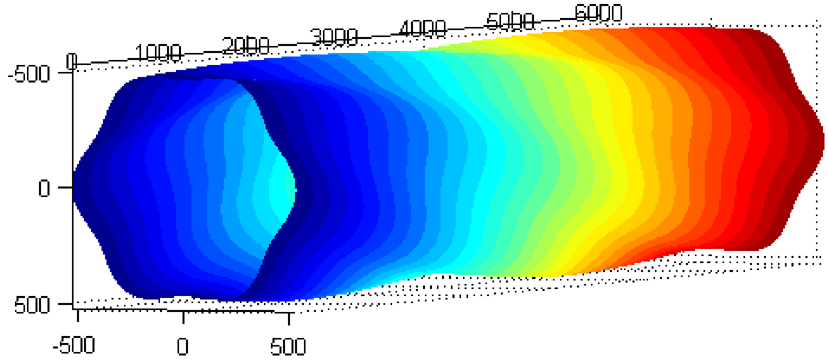

Figure 61: Twisted 6-lobe cylinder surface

The axis of the cylinder, defined as the location of the centres of each cross section, is modelled by expressing C_0 and ϕ_{c0} as functions of *z*-coordinate. In order to represent a real irregular axis, short discrete Fourier series are employed. In equation [9.1.5] *M* is the maximum amplitude of the axis deviation while [*F,G,H,L* and *N,O,P,Q*] are the harmonics of the series.

$$C_0(z) = \frac{M}{4}\left(\sin\left(\frac{z}{Z_{tot}}2\pi F\right)+\sin\left(\frac{z}{Z_{tot}}2\pi G\right)+\cos\left(\frac{z}{Z_{tot}}2\pi H\right)+\cos\left(\frac{z}{Z_{tot}}2\pi L\right)\right)$$

$$\phi_{c0} = \frac{\pi}{2}\left(\sin\left(\frac{z}{Z_{tot}}2\pi N\right)+\sin\left(\frac{z}{Z_{tot}}2\pi O\right)+\cos\left(\frac{z}{Z_{tot}}2\pi P\right)+\cos\left(\frac{z}{Z_{tot}}2\pi Q\right)\right) \quad [9.1.5]$$

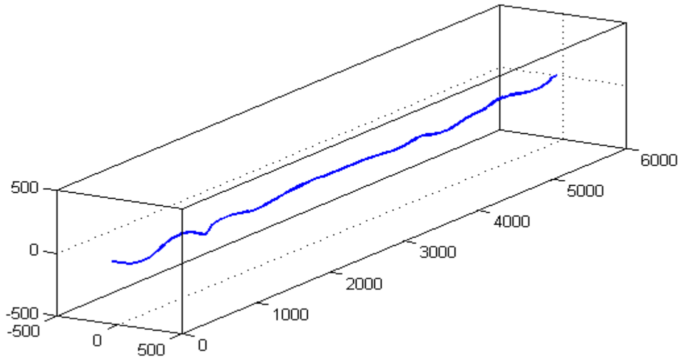

Figure 62: Modelled irregular axis by equation[9.1.5]

At this point all the geometrical characteristics of the lateral surface of the irregular cylinder are modelled. Summarising, it is possible to generate a wide range of cylindrical-like shape by setting:

- Nominal radius and length of the body.
- 12 parameters for mean radius variation and axis deviation.
- 5 parameters for each harmonic desired.

10 MEASUREMENT SYSTEM MODEL

The measurement systems implementable in the model are the multi probes measuring system. Without loss in generality, a three sensors system is represented in what follows that is the minimum set-up necessary to separate the shape from the axis motion by means of a three point reconstruction method.

This method requires three displacement probes around the section under examination to give the distance between the contact point on the cylinder's lateral surface and the ideal intersection point of all three sensors (Z_0 axis). The cylinder under investigation rotates around the Z_0 axis while the displacement sensors measure its surface.

10.1 Cylinder motion modelling

In this section, the rotation of the rolling mill cylinders is taken as the reference for the application of the simulation. For this purpose, the kinematic of the motion of the cylinder over its support is mathematically modelled.

This phase of the simulation can be generalised also to different applications by defining for the actual case the expression of the homogeneous transformation matrix that provides the position of the cylinder as a function of the rotation angle.

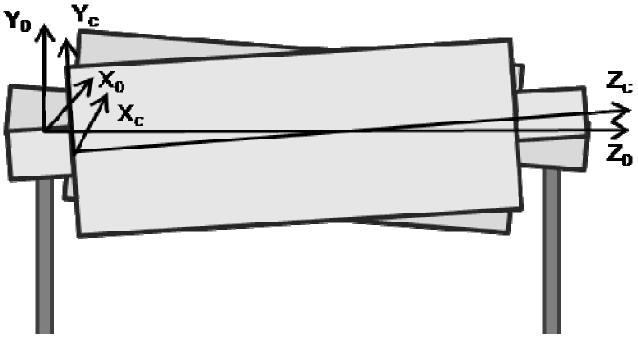

Figure 63: Cylinder motion over supports

10.1.1 Neck and Supports Modelling

In order to simulate the motion over the supports of the rolling cylinder it is necessary to model the shape of the surfaces that roll on the supports. For simplicity, both the supports planes and the necks are supposed rigid and the contact between supports and neck occur in a single cross (bi-dimensional simplification) section for each side of the cylinder. These contact cross sections of the necks are described in the same way as for the section of the cylinder (eq.[9.1.1]) i.e. by means of discrete Fourier series. The Z_c axis of the cylinder coordinate system interpolates the centres of the two necks sections.

$$R_{Front}\left(\phi\right) = R_{0Front} + \sum_{a=1}^{n}\left(R_{aFront} \cdot \cos\left(a \cdot \phi + \phi_{aFront}\right)\right) \tag{10.1.1}$$

The support's planes are defined trough their inclination γ_{dx} and γ_{sx}, whereas their vertical position is defined in a way that the centre of an ideal circular neck with nominal radius R_0 placed over the supports stays on the fixed reference frame Z_0 axis. This concept is showed in Figure 64 where the situation at the front side is depicted.

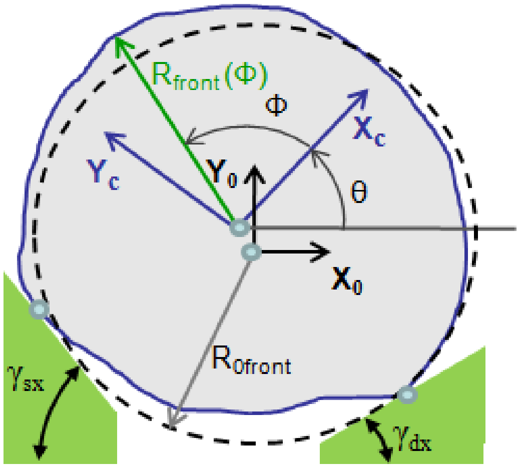

Figure 64: Supports and necks - model

Once the necks and supports are modelled, the position of the cylinder at each rotation angle θ (imposed by the spindle) can be obtained considering the contact constraints among the four supports and the necks surface.

10.1.2 Motion Simulation

The main issue of motion simulation is the individuation of the contact points between the supports and the neck for each imposed angle of rotation θ.

The geometrical relations on which the search method is based are depicted in Figure 65. The strategy is to search the point P^* of the neck profile for which the projection of the radius $R(\phi^*)$ on the perpendicular to the support line $R(\phi^*)\cos\xi$ is maximum. The reported angle ξ is only a combination of the rotation angle θ, the angle of the support γ and ϕ. The P^* search algorithm is divided in two phases. Firstly, the maximum of the projection is searched in a discrete set of angle ϕ equally spaced around the profile. Once the maximum is reached, a recursive research method is employed between the two nearest discrete angles of maximum.

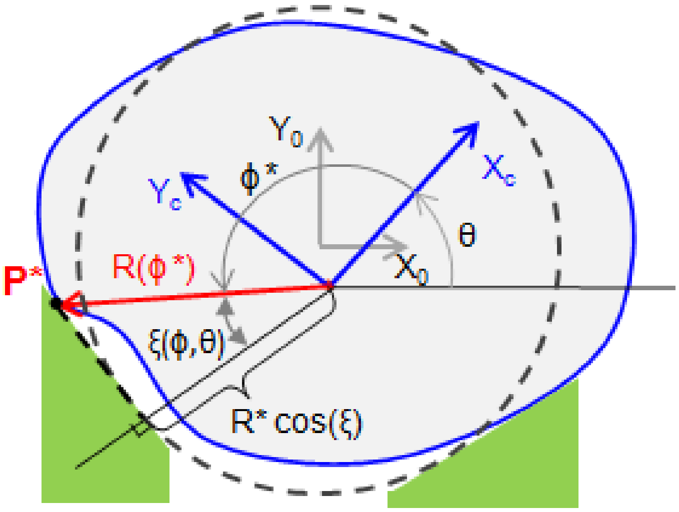

Figure 65: Contact point searching strategy

The method used for this refined search is the well known Golden Section method (Avriel & Wilde, 1966) based on an optimized recursive restriction of the interval. This robust and quite fast method allows finding rapidly the contact point with high precision.

The searching procedure is applied to each support giving the radius $R(\phi^*)$, the projection and the angle ϕ^* of each contact point. Afterwards the position of the centre of the neck is reconstructed by geometrical relations. In Figure 66, the relation between the projections obtained from the search algorithm (P_{sx} and P_{dx}) and the centre position of the neck is represented.

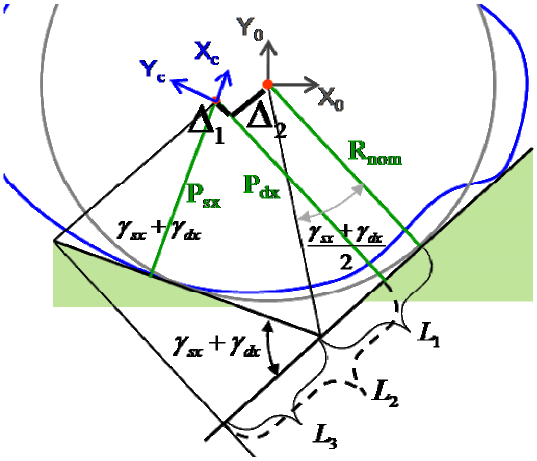

Figure 66: Calculation of the centre position of the neck

It is easy to see that the two distances (Δ_1 and Δ_2) are the component of the translation in parallel and perpendicular direction respect to the right support.

$$L_1 = R_{nom} \tan\left(\frac{\gamma_{sx}+\gamma_{dx}}{2}\right)$$

$$L_2 = \frac{P_{sx}}{\sin\left(\gamma_{sx}+\gamma_{dx}\right)} \qquad L_3 = \frac{P_{dx}}{\tan\left(\gamma_{sx}+\gamma_{dx}\right)}$$

$$\Delta_2 = L_1 - L_2 + L_3 \qquad \Delta_1 = P_{dx} - R_{nom} \qquad [10.1.2]$$

Equation [10.1.2] expresses the geometrical relations that give Δ_1 and Δ_2. These two components can be easily decomposed in the x and y translations of the centre of the neck in the machine coordinate system $\{O_0X_0Y_0Z_0\}$.

Knowing the translations of the rear and front necks and the other geometrical parameters of the cylinder it is possible to build the roto-translation matrix (*RT*) for each angle of rotation representing in this way the cylinder motion. The RT matrix describes the homogeneous coordinate transformation from the cylinder frame to the fixed frame. In order to avoid ambiguity it is better to specify that the RT matrix applied to a point expressed in the cylinder frame gives the coordinate of the same point in the reference frame.

This set of matrices, one for each angle of rotation, is the main output of the motion modelling and, as above mentioned, if another kind of kinematic is employed, the RT matrix that represents the motion has to be calculated consequently.

10.2 **Measurement system**

The three sensors are mounted on a support that can translate along z-axis allowing to measure different cross sections of the cylinder. The support is supposed rigid, no deformation are taken into account.

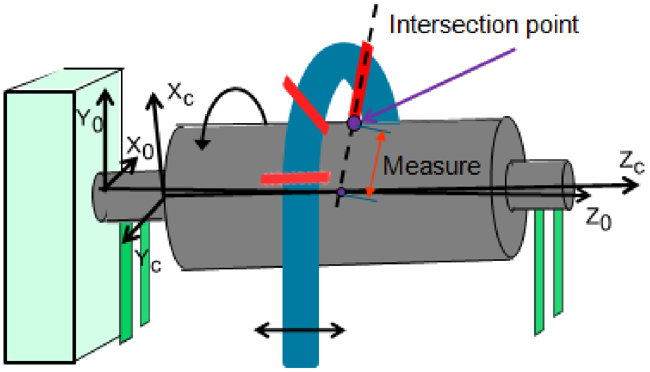

Figure 67: Measurement system for three point method on rolling mill cylinders

In Figure 68 the nominal disposition of the probes and the relative parameters are represented. There are three geometrical parameters of the support: the distances X_{ref} and Y_{ref} of the point Z_{point} where the z-position of the support is measured (e.g. by a linear encoder on the slide) and the radius of the support R_s. Moreover each sensor is placed on the arc of the support by the position angle α_i.

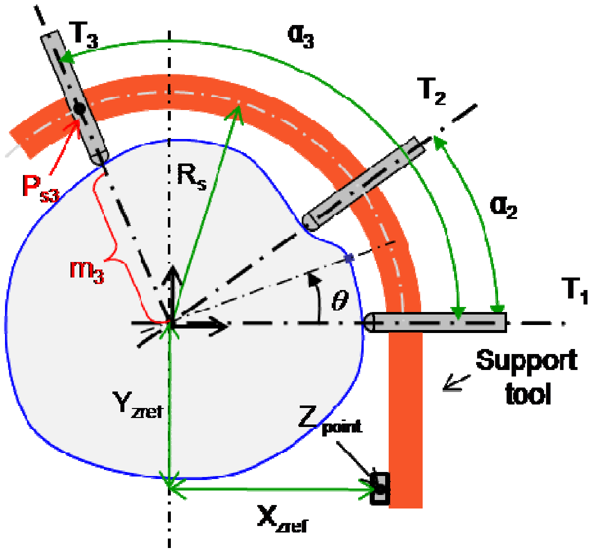

Figure 68: Measurement system – probe location on the cross section

A fundamental task of the simulation of the measurement process is the performance evaluation of both the system and the measures elaboration method in term of accuracy of the section reconstruction. Obviously the measures are strongly affected by the position and orientation errors of the sensors. Hence, in addition to the parameters above mentioned that describe the nominal configuration of the measurement equipment, a number of parameters are inserted.

The alignments errors of the support are introduced and the positioning and alignment errors of each probe on the support are modelled as shown in Figure 69 and Figure 70.

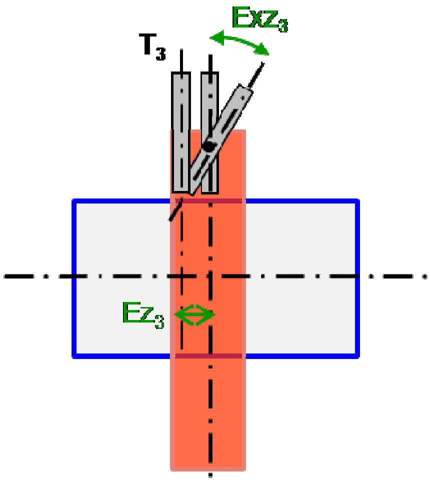

Figure 69: Position and inclination errors - lateral view of sensor 3

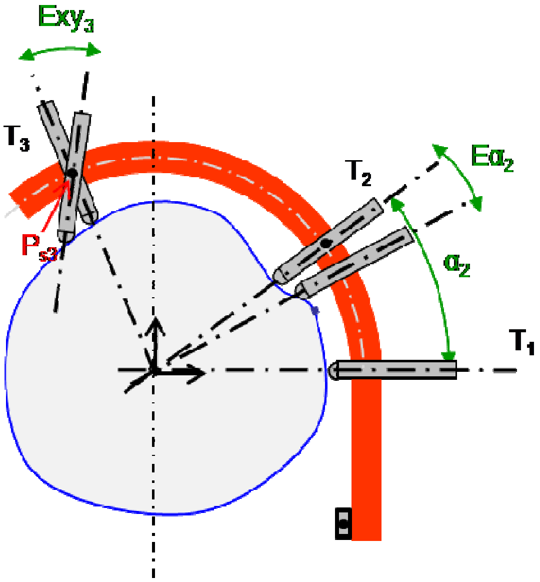

Figure 70: Position and inclination errors - frontal view

It is possible to identify two positioning errors for each sensor. One is the error related to the angular positioning of the probe on the support arc $E\alpha_i$ (i.e. the sensor points to the centre but at a different angle α). The other one is the z positioning error on the support Ez_i. Moreover there are two inclination angles: the xy inclination Exy_i and the xz inclination Exz_i. The first one is an inclination around P_{si} in xy plane whereas the second one is an inclination around Ps out of xy plane (i.e. in the z-sensor axis plane). In an ideal situation this two angles are zero because each sensor axis lies on a X_0Y_0 plane.

The final step is the introduction of the alignment errors of the whole support. The measurement point of the z position of the support represents the centre point of the two rotations. The support is firstly rotated around the vertical axis and then around the horizontal axis passing in Z_{point} (Exz_s and Eyz_s).

Combining the transformation relative to the positioning of the sensor on the support, the errors on position and inclination of the probe and the support inclinations and position, the total transformation matrix is obtained.

Finally the versor and the fixing point of each sensor are obtained and can be used by the measurement algorithm.

10.3 Measure computation

The measure assessed by the displacement sensors is a distance, on the sensor's axis, between the surface of the cylinder and a predefined zero. This zero point, for each sensor in ideal condition, lie on the Z_0 axis. In order to simulate the measures performed by the sensors depending on the cylinder's shape and the motion imposed by interactions with supports, the line of action of the sensors has been intersected with the surface of the cylinder as a function of the rotation θ.

The sensors are attached to the supporting frame (fixed) and therefore their position and direction can be defined in 3D space using versors in the fixed reference frame.

One way to search the intersection between the axis of the displacement sensor and the simulated cylinder is to perform a minimization of the distance of the points describing the cylinder and the line, but evidently this approach is not computationally efficient, as the whole cylinder shall be discretized into points; to reduce uncertainty in the intersection position, the number of points shall be increased, leading to time demanding searches.

An iterative approach has been therefore defined to minimize the number of points that has to be computed. The intersection is performed in two steps: a first attempt intersection with an ideal cylinder, roto-translated according to the imposed motion, is found and then an iterative search on the simulated irregular cylinder within the imposed accuracy is performed.

The intersection of the direction of the sensor with the ideal cylinder having the same base nominal radius R_N of the real cylinder is calculated (*P1*) to identify a first attempt $z = z(P1)$ coordinate. From this z coordinate it is possible to evaluate, by the modelling formulas explained above, the parameters of the section of interest, such as position of the centre of the section C_0 and complete definition of the real profile.

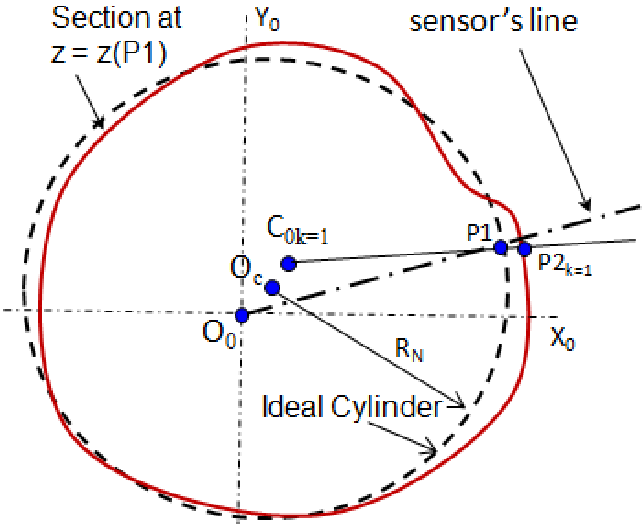

Figure 71: Intersection with the ideal cylinder

From the position of the centre C_{0k} and from the intersection with the ideal cylinder $P1$, it is possible to evaluate the point of the profile aligned with these two points ($P2_k=\{x2,y2,z2\}$). It has to be noted that this point of the real cylinder doesn't lie in the line of the sensor, having a z that doesn't belong to the line equation. After projecting the point $P2_k$ into the line of the sensor ($P3_k=\{x3,y3,z3\}$), a new z coordinate is found and the search can continue iteratively starting from this point until the distance from the real point and the line of the versor is below a defined threshold. The steps of the iteration search algorithm are schematized in Figure 72.

Using the definition of the versor angles, the line of the versor in the plane xy remains the same independently on the z coordinate allowing the iteration described above. The intersection is then repeated for a complete rotation of the cylinder and for all the sensors, allowing thus the assessment of the measures performed by the displacement sensors.

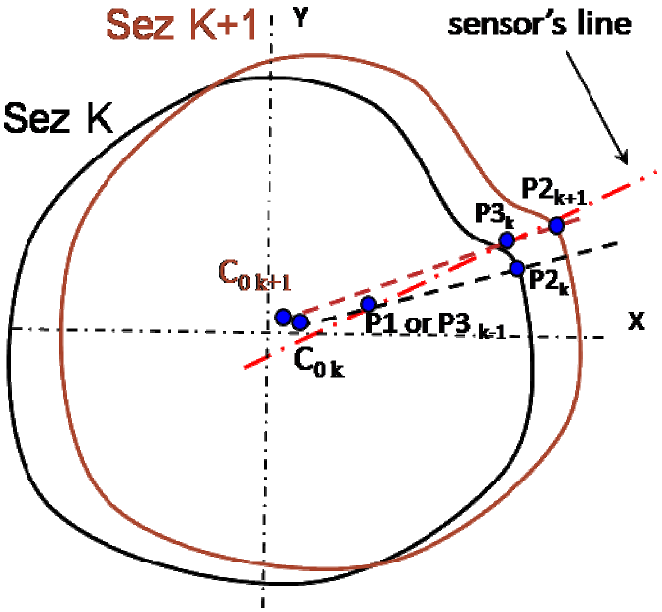

Figure 72: Sequence of the iterative intersection search

11 SIMULATIONS OF THE MEASUREMENT PROCESS

In this chapter, five meaningful simulations of the measurement process are reported with the aim to explain the flexibility of the model proposed and the importance of modelling both the motion and the sensors positioning inaccuracy for a good simulation of the process. For each simulation the main parameters employed are reported for clarity.

In order to use reasonable values, and because of the collaboration with an important producer of roll grinders, harmonics, distances and the others parameters employed are related to the measurement of rolling mill cylinders.

11.1 Simulation 1: shape and axis deviation

In this first simulation, only the shape of the cylinder and its axis deviation are modelled. The necks are ideal so the feed rotation is perfectly around the Z_0 axis, hence, the Z_0 and Z_c axes are always on the same line. Sensors and support tool are in nominal configuration and so each probe measure exactly the same cross section (the same Z_c). Only the axis deviation prevents the radius from being directly measured by the sensors leading to a circular motion of the centre of each cross section.

The following parameters have been used, distances are in mm, probes angles are in degree and the harmonics phases are in radiant:

Cylinder parameters:

A_{ra}	0	0.1	0.1	0.1	0.1	0.1	0.1	0.05	0.05	0.05	0.01	0.01	0.01	0.01	0.01
B_{ra}	0	5	6	10	12	10	7	10	20	10	10	20	10	5	0
C_{ra}	0	0	$\pi/4$	π	0	$\pi/4$	0	π	0	0	0	π	0	$\pi/4$	0
D_{ra}	0	π	π	0	$\pi/2$	π	0	0	$\pi/2$	0	0	0	π	0	0
E_{ra}	0	1	3	1	2	1	0	1	0	1	2	0	3	1	1

$DD_{ra}=0$; $R_n = 400$; $L_{cil} = 1000$; $L_{colli} = 100$; $A_{r0} = 1$; $B_{r0} = 1$; $C_{r0} = -\pi/2$

Axis deviation model:

F = 1; G = 2; H = 2; L = 0; M = 0.5; N = 1; O = 3; P = 1; Q = 1

Measurement Model:

$\alpha_{1,2,3}$ = [0 45 81]; z_s = [50 500 950]; θ_{step} = 1°

Where z_s are the position along the Z_0 axis in which the section are measured and θ_{step} is the angular resolution of the measurement process. Necks harmonics and positioning errors are set to zero.

Figure 73 reports the measures simulated versus angle of rotation for the three probes in the section at z_s = 500 mm. It is easy to see that the measures from the same section are identical but shifted by the sensor angular distance. This is due to the complete ideality of the model. In fact the sensors are perfectly mounted on the support that is perpendicular to the cylinder axis. Moreover there is no movement of the cylinder except the rotation around the Z_0-axis. The axis deviation changes the form of the measure but in the same way for each sensor.

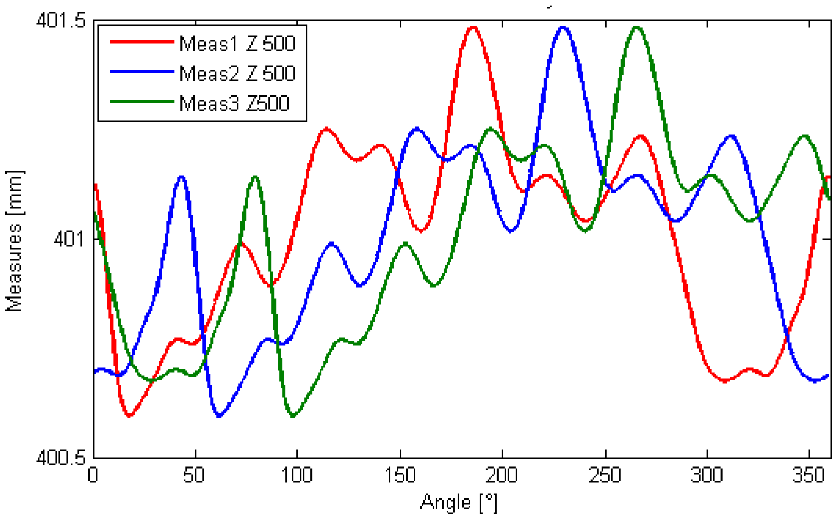

Figure 73: Simulation1 - Measures from different probes in the same cross section

In Figure 74 measures from the same sensor in three different cross sections are reported. There are no correlations between measures from different section because of the different harmonic composition modelled by the equations [9.1.3] and [9.1.4], and because of the different axis deviation of each section.

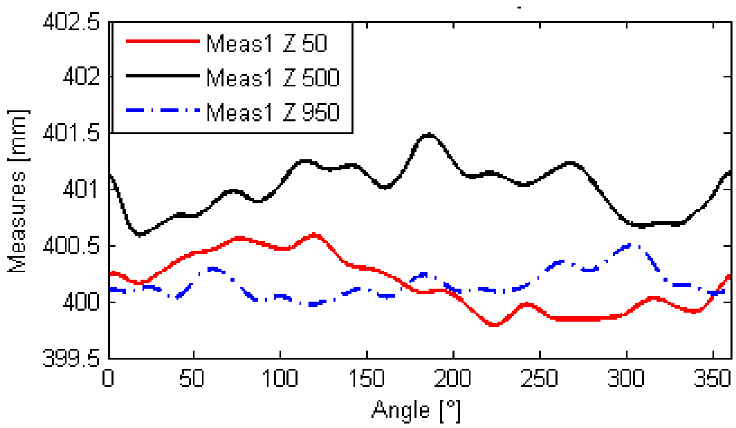

Figure 74:Simulation1 – Measures in different cross section

11.2 **Simulation 2: support tool inclination**

In order to show the importance of a precise modelling of the measurement system, only the orientation errors of the support tool are introduced in this simulation. The cylinder employed for the simulation is almost the same as for simulation1 but without axis deviation. The motion is still ideal and the sensors positioning and alignment too. Only the support is inclined. The parameters changed from simulation1 are reported below.

Cylinder Model:

$B_{r0} = 10$; $E_{ra} = [0\ 0\ 3\ 1\ 0\ 1\ 0\ 1\ 0\ 0\ 0\ 0\ 3\ 1\ 0]$

Axis Model:

$M = 0$ (i.e. straight cylinder's axis)

Measurement Model:

$Y_{zref} = 1000$; $X_{zref} = 1000$; $R_s = 1200$; $Exz_s = 1$; $Eyz_s = 1$

In Figure 75 the measures of two probes in the central cross section of the cylinder are represented in continuous line. The same measures (i.e. at the same z_s) ,but with an ideal support tool are reported in dot line for comparison. Observing the two groups of measures the effect of the inclination of the support is evident. The mean values of the measures are very different, the mean differences between ideal and biased measures on the reported section are 1.1 mm for probe2 and 0.85 mm for probe3. Considering the maximum amplitude of the imposed harmonics, a mean difference of ten times this value is registered. The main cause of this difference is due to the kinematic of the support tool. In particular the distance between the Z_{point} and the sensors imply relevant changing in position with relatively small inclination angles of the support, determining the sensors to measure at different cross sections.

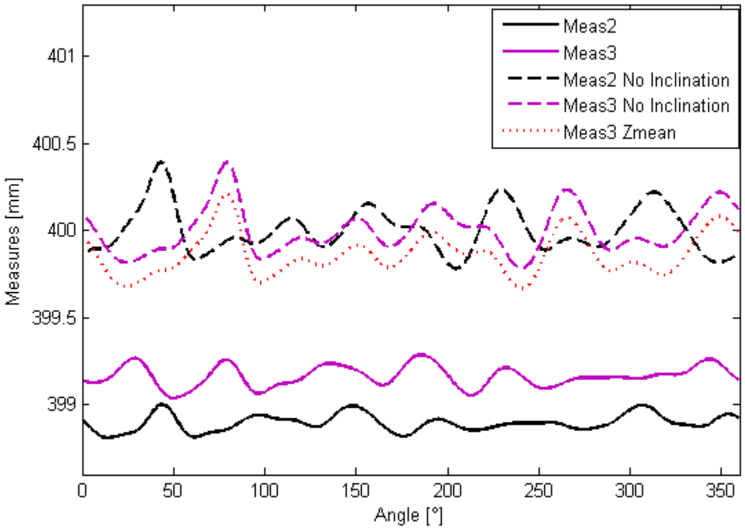

Figure 75: Simulation2 - Measures with support tool inclination

With the aim of splitting this effect from the others, the measure of probe3 with the distances X_{zref} and Y_{zref} sets to zero are reported in small dot line. It represent a situation in which the measurement system is still inclined by the errors introduced but the base point of this rotation lies on $Z_0 \equiv Z_c$ axis at z_s. The offset is clearly reduced but the measured section is still different from the nominal one.

In Figure 76 the difference between the two situations exposed above and the ideal situation are represented. It is evident that there is not only an offset effect but there is difference in the form of the measures between the ideal situation and the other two exposed previously. This is mainly due to the fact that, due to the inclination of the support, a different section is measured by the sensors. Moreover each of the three sensor act on a different section with an axis that is not parallel neither to the X_0Y_0 nor to the X_cY_c planes. It's easy to deduce that it is very important to take into account this effect to reach a good representation of the process, the mean difference measured between the ideal situation and the one in the Zmean is about 270µm whereas a spread of about 70 µm evidence that also the effect on the shape of the measure (i.e. the harmonics) is not negligible for accurate measurements.

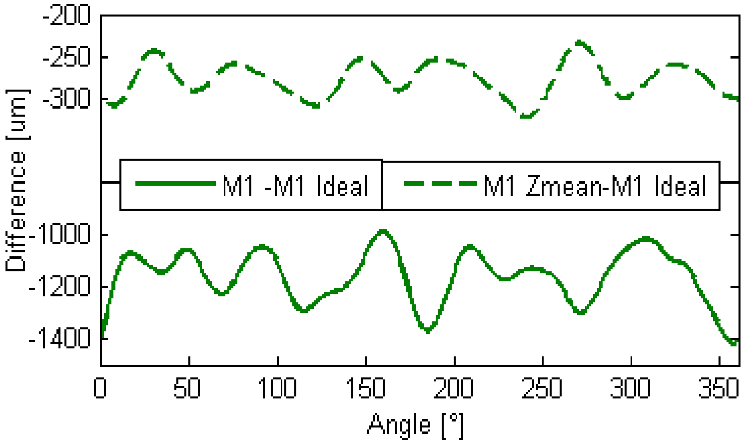

Figure 76: Simulation2 - comparison with ideal measure

11.3 Simulation 3: sensor's position and alignment errors

In this simulation only the position and alignment errors of the probes are implemented. No inclinations of the support tool neither motion are introduced. The same cylinder of the simulation2 is used whereas the axis deviation is reintroduced as in simulation1. The parameters changed from simulation2 are reported below.

Axis deviation model:

$F = 1;\ G = 2;\ H = 2;\ L = 0;\ M = 0.5;\ N = 1;\ O = 3;\ P = 1;\ Q = 1$

Measurement Model:

$E\alpha_{1,2,3} = [\ -0.1\ 0.1\ 0.1\ ]$; $Ez_{1,2,3} = [\ 0.1\ -0.1\ 0.1\ ]$

$Exy_{1,2,3} = [\ 0.1\ -0.1\ 0.1\ ]$; $Exz_{1,2,3} = [\ -0.1\ 0.1\ -0.1\ ]$

$Exz_s = 0$; $Eyz_s = 0$; $z_s = [$ 1000 section between 50 and 950 $]$;

In Figure 77 the difference between the measure simulated introducing the above position and alignment errors and the ideal measure (i.e. without mounting errors) to scansion angle is shown for three cross section. The magnitude of the difference, if compared with the effect of the support inclination, is small but is still important particularly for the harmonics, in which the reconstruction algorithm is more sensible.

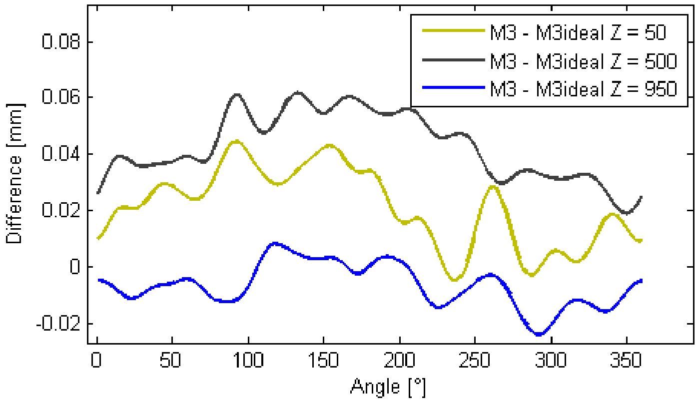

Figure 77: Simulation3 - difference ideal measure and measure with position errors

Obviously, the effect of the position and alignment error on the measures strongly depends on the surface and hence on the section measured. In order to better represent the difference between a simulation that take into account the mounting errors and an ideal one, the measures from sensor2, in 100 cross section with 360 point for section are compared for these two simulations. The histogram of these differences i plotted in Figure 78.

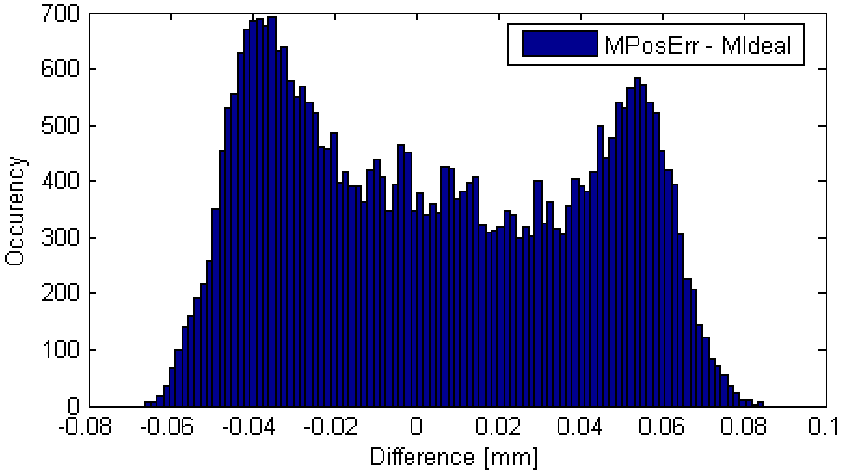

Figure 78: Simulation3 - histogram of the differences

The histogram comprehends 36000 values from the second sensor. The distribution of the differences is neither symmetric nor sharp but covers almost uniformly a wide range of values. This behaviour let us think that, the influence of this positioning inaccuracy, on the measure, is mainly dependent on the surface that is under analysis and probably on the other aspects (i.e 3D motion and support inclination). The deep investigation of the effects of the four parameters of the position and alignment errors, that are clearly strongly correlated, requires analysis involving Monte Carlo simulation coupled with DOE techniques in which shape, axis are casually generated. This is not the case of this section where quantitative behaviours are important.

11.4 Simulation 4: irregular motion

In this session the three dimensional motion of the irregular cylinder over its supports is introduced in the simulation. The cylinder employed is the same as the one used for simulation2, hence, its axis is straight. Supports and sensors are in the ideal configuration and the support has the parameters in following.

Support Model:

$\gamma_{FrontSX} = 60$; $\gamma_{FrontDX} = 20$; $\gamma_{BackSX} = 60$; $\gamma_{BackDX} = 20$

$R0_{Front} = 200$; $R0_{Back} = 200$

$Ra_{Front} = Ra_{Back} = [0\ 0.1\ 0.1\ 0.1\ 0.05\ 0.05\ 0.05\ 0.01\ 0.01]$

$\phi a_{Front} = [\ 0\ \ 0\ \ \pi/4\ \ 0\ \ \pi/3\ 0\ \ \pi\ \ 0\ \ \pi/7]$

$\phi a_{Back} = [\ 0\ \pi/2\ \ \pi\ \ \pi/5\ \ \pi/5\ \ \pi\ \ \pi/3\ \ pi/7\ \ 0]$

In Figure 79 measures from probe 2 and 3 of z_s=950 cross-section are reported. The effect of motion is to deform the whole profile of the measure; there are not offsets because the motion is finally centred on the absolute Z_0 axis. This is due to de definition of the position of the neck-supports explained in 10.1.1, but it is easy to introduce an offset on rotation axis if needed.

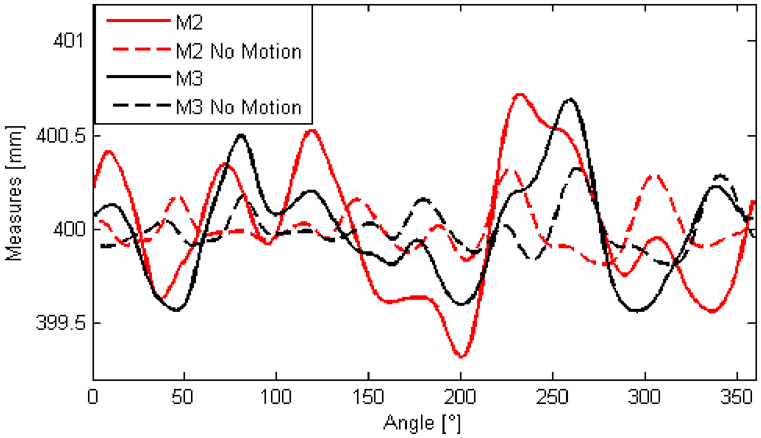

Figure 79:Simulation4 - measures with and without motion

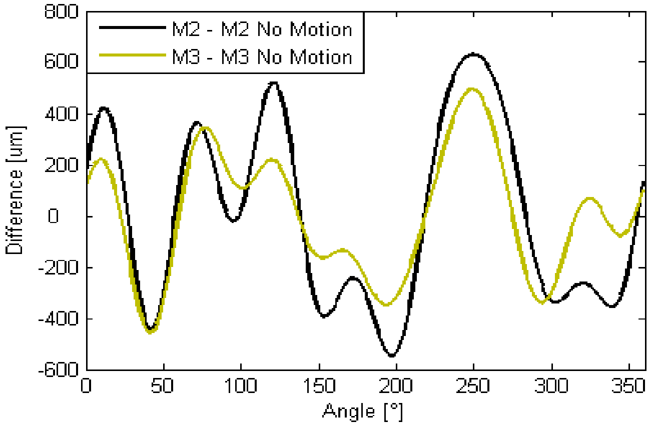

Figure 80: Simulation4 – differences on the measures

Motion simulation is one of the most important characteristics that should be modelled and Figure 80 clearly shows that. A difference of 500 µm between the measures considering motion and the measures without motion, reveals that if the motion is not taken into account than the measures simulated are quite meaningless. In Figure 81 the histogram of the differences for all the sensors in the whole measurement points is shown.

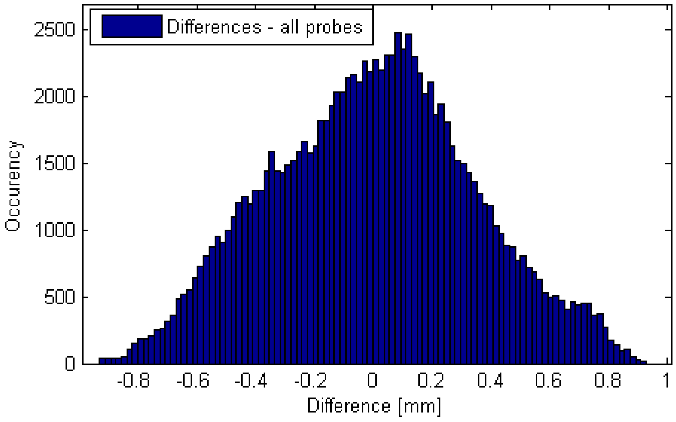

Figure 81: Simulation4 - differences histogram for all probes

With the neck's harmonic imposed, differences of nearly one millimetre can be reached. In order to evaluate the performance of reconstruction method based on three point method, that try to split the profile and the motion, it's fundamental the implementation of the cylinder motion that interacts with the axis deviation giving the true cross section boundary motion.

11.5 Simulation 5: complete simulation

This final simulation, regarding the measurement process, has the aim to emulate a real measurement system for rolling mill cylinders. For this purpose all the parameters are introduced in the simulation taking into account an almost realistic condition. The cylinder employed is the same of simulation 4 but with axis deviation modelled like in simulation 1. Both supports and necks are the same as simulation 4. New parameters inserted are reported hereafter:

Measurement Model:

$Exz_s = 0.5$; $Eyz_s = -0.4$ $E\alpha_{1,2,3} = [\ -0.2\ 0.1\ 0.2\ ]$; $Ez_{1,2,3} = [\ 0.1\ -0.2\ 0.1\ ]$

$Exy_{1,2,3} = [\ 0.05\ -0.05\ -0.07\ ]$; $Exz_{1,2,3} = [\ -0.04\ -0.08\ 0.1\ ]$

In Figure 82 the comparison among measures from probe3 are represented.

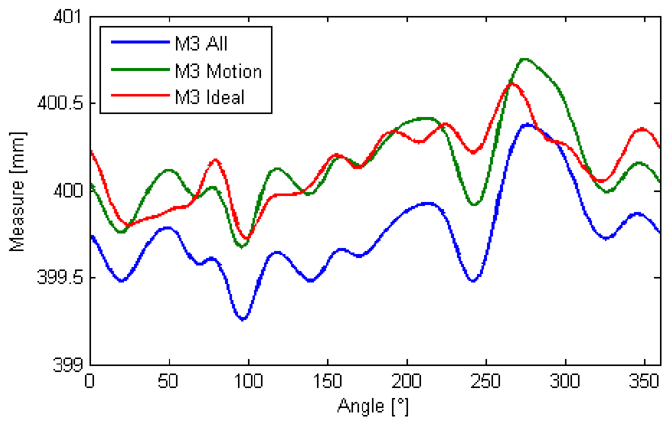

Figure 82: Simulation5 - measures

M3all is the measure with all the disturbance implemented whereas M3motion is the measure with only the shape, the axis deviation and the motion over irregular supports. M3 Ideal is the measure without disturbances. It is clear that the three measures are significantly different, so the effect of all the factors described previous is conspicuous. Both the motion and the mounting errors strongly affect the measures assessed by the displacement sensor. In particular the positioning errors (mainly the inclination of the support) lead to a conspicuous difference on the mean measure of the section whereas the motion seems to nearly introduce a fluctuation around the ideal measure.

In order to evidence these effects a simulation on 100 sections with all the disturbances and without motion is performed. The results are compared with the ideal measures (i.e. only shape and axis deviation) and the differences of the probe1 are calculated. In Figure 83 the difference for all the section at two scansion angle (1° and 80°) are plotted in dot lines whereas the in continuous lines there are the differences on the measures at which the mean value on the section was subtracted. It is evident that a trend is present along the section for the differences whereas the second elaboration shows that this trend affect only the mean value of the measures. In fact, subtracting in each section the mean value of the respective measure from both the ideal and the biased ones, this trend vanish.

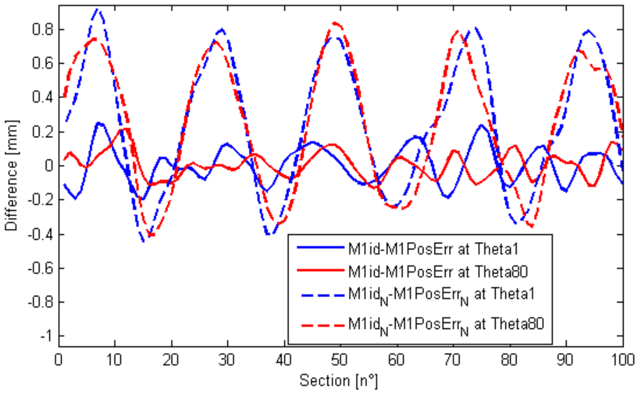

Figure 83: macro-effect of probe errors

Similar phenomena can be observed for the motion but in the opposite way. In fact the motion introduces an effect with a trend on the angle as can be deduced thinking on the rigidity of that motion.

In Figure 84 the histogram of the differences among ideal and biased measures is plotted.

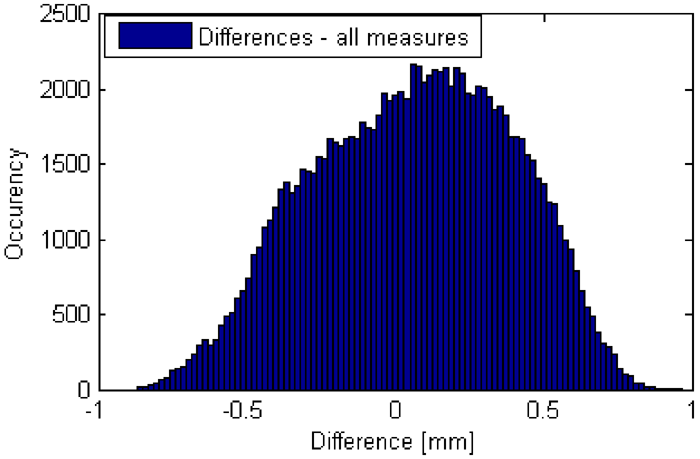

Figure 84: Simulation5 – differences histogram for all probes

Comparing this histogram with the one in Figure 81, the differences range is almost the same but there are more data far from zero in the last simulation. This behaviour is clearly due to the presence of the mounting errors.

Finally, other two important disturbances can be simply added to each measure. The first one is the sensor's zero offset. In fact there can be an error on the zeroing of the sensor and hence the measure may be affected by a constant bias. The other aspect is the noise on measures that is modelled as a white noise and added to the single measure of the probe. Obviously, these two aspects directly influence the value of the measure and so there are no simulations now to show that. However in the next, this two bias will be used for the simulation of the process and reconstruction task.

12 MULTI-POINT RECONSTRUCTION METHOD

In this chapter the development of a three point method for the reconstruction of shape and motion of a cross section of the cylinder is explained (Zhang et al., 1997).

12.1 Three point method

The architecture of the measurement system is well depicted on the above chapter so let us focus on a single cross section to derive the relation between an ideal measure and the geometrical parameters of the section, the indices relative to the specific cross section and the dependence on z of the variables will be omitted in what follow for clarity. In Figure 85 the measure of the *i* probe, positioned at angle α_i, at the scansion angle θ_j is schematized. The ideal measure $m_i(\theta_j)$ is a composition of the radius of the section $R(\phi)$ and its centre position $[C_0, \phi_{c0}]$ that are the unknowns we searching for. The axis origin is placed on the Z_0 axis and is the converging point of the sensors.

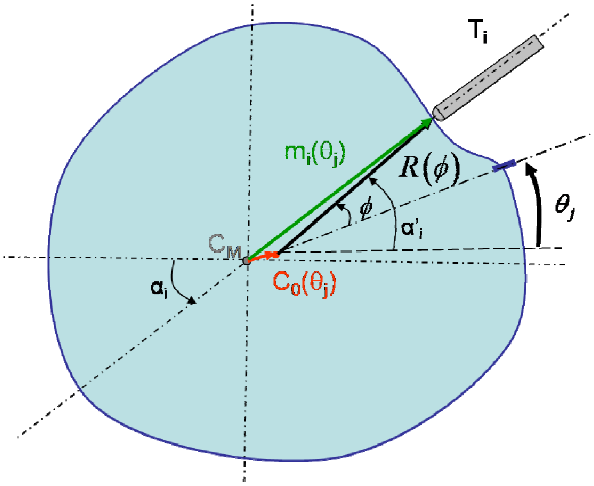

Figure 85: Measure on a cross section

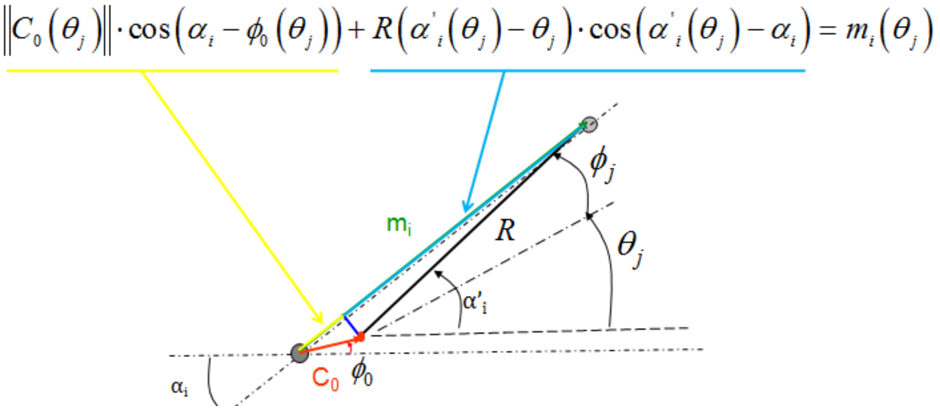

Figure 86: Decomposition of the measure

The relation outsourced in Figure 86 introduce the angle α'_i that depend on the centre position (unknowns), on the measure and obviously on the sensor angle. This relation is not explicit and an analytical solution is not possible. An approximation is commonly introduced (Gao et al., 1997) (Muralikrishnan et al., 2005) (Jeong et al., 2005)that is admissible when the centre deviation C_0 is very small respect to the radius that is the case of most practical application. Hence we assume that the sensor angle α_i and the α'_i are almost equal and so:

$$\alpha'_i \cong \alpha_i \quad \cos\left(\alpha'_i-\alpha_i\right)\cong 1 \quad R\left(\phi_j\right)=R\left(\alpha'_i-\theta_j\right)\cong R\left(\alpha_i-\theta_j\right) \qquad [12.1.1]$$

and the relation between the measure and the unknowns' radius and center position becomes:

$$C_0\left(\theta_j\right)\cdot\cos\left(\alpha_i-\phi_{c0}\left(\theta_j\right)\right)+R\left(\alpha_i-\theta_j\right)=m_i\left(\theta_j\right) \qquad [12.1.2]$$

In equation [12.1.2] there are three unknowns: C_0, ϕ_{c0} *and* $R(\phi)$ therefore more equation are necessary to solve that problem. Adding the others sensor lead to an increment of both the equation and the unknown variables because the radius measured by each sensor is phase-shifted by the sensor angle.

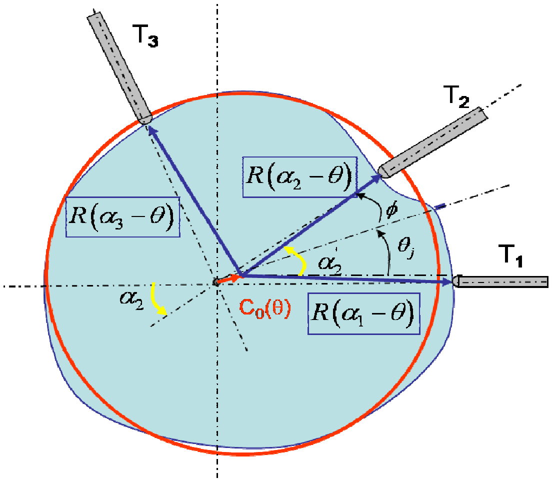

Figure 87: Three point method configuration

The key point of the three point method is the introduction of the Fourier transforms on the measure expression in [12.1.2]. The phase shift of the radius becomes a multiplication of the Fourier transform of the radius by an exponential term involving the angle of the sensor. In what follows, the centre position is expressed in Cartesian coordinates for convenience in mathematical manipulations. The coordinate X_{c0} and Y_{c0} are the Fourier transform of the Cartesian coordinate of the section centre easily derived from the previous polar expression.

$$R(-\omega)\cdot e^{-I\omega\alpha_i}+X_{c0}(\omega)\cos(\alpha_i)+Y_{c0}(\omega)\sin(\alpha_i)=M_i(\omega) \quad [12.1.3]$$

By applying this transformation at the measures of the three sensors a well-behaved system can be generally obtained:

$$\begin{aligned}
R(-\omega)\cdot e^{-I\omega\alpha_1}+X_{c0}(\omega)\cos(\alpha_1)+Y_{c0}(\omega)\sin(\alpha_1)&=M_1(\omega)\\
R(-\omega)\cdot e^{-I\omega\alpha_2}+X_{c0}(\omega)\cos(\alpha_2)+Y_{c0}(\omega)\sin(\alpha_2)&=M_2(\omega) \quad [12.1.4]\\
R(-\omega)\cdot e^{-I\omega\alpha_3}+X_{c0}(\omega)\cos(\alpha_3)+Y_{c0}(\omega)\sin(\alpha_3)&=M_3(\omega)
\end{aligned}$$

This system can be solved analytically for the radius and the centre position:

$$R\left(-\omega\right)=\frac{M1\sin\left(\alpha_2-\alpha_3\right)+M2\cdot\sin\left(\alpha_3\right)-M3\cdot\sin\left(\alpha_2\right)}{\sin\left(\alpha_2-\alpha_3\right)+\sin\left(\alpha_3\right)\cdot e^{-I\cdot\omega\cdot\alpha_2}-\sin\left(\alpha_2\right)\cdot e^{-I\cdot\omega\cdot\alpha_3}}$$

$$X_{c0}\left(\omega\right)=\frac{M1\left(e^{-I\cdot\omega\cdot\alpha_2}\cdot\sin\left(\alpha_3\right)-e^{-I\cdot\omega\cdot\alpha_3}\cdot\sin\left(\alpha_2\right)\right)-M2\cdot\sin\left(\alpha_3\right)+M3\cdot\sin\left(\alpha_2\right)}{\sin\left(\alpha_2-\alpha_3\right)+\sin\left(\alpha_3\right)\cdot e^{-I\cdot\omega\cdot\alpha_2}-\sin\left(\alpha_2\right)\cdot e^{-I\cdot\omega\cdot\alpha_3}}$$

$$Y_{c0}\left(\omega\right)=\frac{M1\left(e^{-I\omega\alpha_3}\cos\left(\alpha_2\right)-e^{-I\omega\alpha_2}\cos\alpha_3\right)+M2\left(-e^{-I\omega\alpha_3}+\cos\alpha_3\right)-M3\left(e^{-I\omega\alpha_2}+\cos\alpha_2\right)}{\sin\left(\alpha_2-\alpha_3\right)+\sin\left(\alpha_3\right)\cdot e^{-I\cdot\omega\cdot\alpha_2}-\sin\left(\alpha_2\right)\cdot e^{-I\cdot\omega\cdot\alpha_3}}$$

[12.1.5]

obviously the measures are discrete and so the discrete Fourier transforms are used. In practice the Fast Fourier Transform is utilized to convert the sets of measures in angular domain into their discrete transform in harmonics domain.

$$R\left(a\right)=\frac{M1\left(a\right)\cdot\sin\left(\alpha_2-\alpha_3\right)+M2\left(a\right)\cdot\sin\left(\alpha_3\right)-M3\left(a\right)\cdot\sin\left(\alpha_2\right)}{\sin\left(\alpha_2-\alpha_3\right)+\sin\left(\alpha_3\right)\cdot e^{-I\cdot\frac{2\pi\cdot a}{N}\cdot\alpha_2}-\sin\left(\alpha_2\right)\cdot e^{-I\cdot\frac{2\pi\cdot a}{N}\cdot\alpha_3}}$$

$$X\left(a\right)=\frac{M1\left(a\right)\left(e^{-I\cdot\frac{2\pi\cdot a}{N}\cdot\alpha_2}\sin\left(\alpha_3\right)-e^{-I\cdot\frac{2\pi\cdot a}{N}\cdot\alpha_3}\sin\left(\alpha_2\right)\right)-M2\left(a\right)\sin\left(\alpha_3\right)+M3\left(a\right)\sin\left(\alpha_2\right)}{\sin\left(\alpha_2-\alpha_3\right)+\sin\left(\alpha_3\right)\cdot e^{-I\cdot\frac{2\pi\cdot a}{N}\cdot\alpha_2}-\sin\left(\alpha_2\right)\cdot e^{-I\cdot\frac{2\pi\cdot a}{N}\cdot\alpha_3}}$$

$$Y=\frac{M1\left(e^{-I\frac{2\pi a}{N}\alpha_3}\cos\left(\alpha_2\right)-e^{-I\frac{2\pi a}{N}\alpha_2}\cos\alpha_3\right)+M2\left(-e^{-I\frac{2\pi a}{N}\alpha_3}+\cos\alpha_3\right)-M3\left(e^{-I\frac{2\pi a}{N}\alpha_2}+\cos\alpha_2\right)}{\sin\left(\alpha_2-\alpha_3\right)+\sin\left(\alpha_3\right)\cdot e^{-I\cdot\frac{2\pi\cdot a}{N}\cdot\alpha_2}-\sin\left(\alpha_2\right)\cdot e^{-I\cdot\frac{2\pi\cdot a}{N}\cdot\alpha_3}}$$

[12.1.6]

Where *a* is the harmonic considered and the transform are in harmonic domain computed by the FFT algorithm.

Obtained the radius and the barycentre position in harmonics domain it is possible to apply the inverse discrete Fourier transform to calculate the desired values in angular domain.

$$R\left(\phi_j\right)=\frac{1}{N}\sum_{a=0}^{N-1}R\left(a\right)\cdot e^{I\cdot\frac{2\pi}{N}a\cdot\phi_j}\qquad j=0,1,\ldots359$$

$$X\left(\theta_j\right)=\frac{1}{N}\sum_{a=0}^{N-1}X\left(a\right)\cdot e^{I\cdot\frac{2\pi}{N}a\cdot\theta_j}\qquad j=0,1,\ldots359 \qquad [12.1.7]$$

$$Y\left(\theta_j\right)=\frac{1}{N}\sum_{a=0}^{N-1}Y\left(a\right)\cdot e^{I\cdot\frac{2\pi}{N}a\cdot\theta_j}\qquad j=0,1,\ldots359$$

By this method, the angular series of radius and center position for the analyzed cross section are computed obtaining a reconstruction of the single cross section. In Figure 88 the result of a reconstruction in ideal condition is plotted as radius values and reconstruction error of the radius.

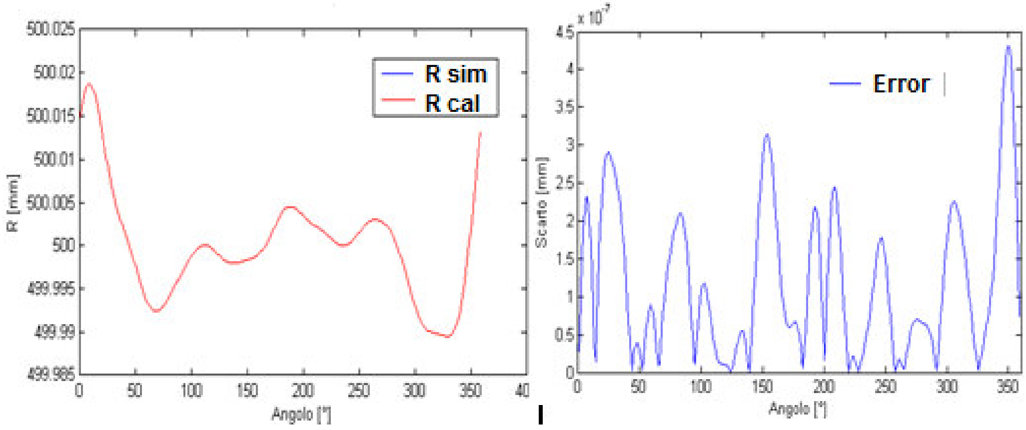

Figure 88: Reconstruction by three point method in ideal condition - Radius and Error on radius

Note that the reconstruction error, computed as the difference between the simulated and the reconstructed radius for each angle θ, is of about 10^{-7} mm on a mean radius of 500 mm and harmonics of both the barycentre motion and the surface of 0.01 mm.

13 SIMULATIONS OF THE MEASUREMENT AND RECONSTRUCTION PROCESS

The three point method developed in the previous section can be tested for performance evaluation, sensitivity analysis or error budget estimation by means of the measurement system model explained in the above chapters. Firstly some particular simulations are reported in order to evidence important aspects and to discuss them. Then, in order to evidence the influences of some features in the reconstruction performance, a Monte Carlo simulation method is implemented firstly only on the cross section simulation and finally on the whole measurement system model and some simulation are reported. It is worth to note that it's not the aim of this dissertation the investigation of uncertainties propagation in the reconstruction process or the assessment of the error budget for the measurement system (that are in any case strongly related with the specific case investigated) or some other deep analysis but only a discussion on the model and on the reconstruction algorithm are of interest.

13.1 Three point method simulations on the cross section – 2D

In the last section, a reconstruction of the radius with the 3P method was depicted and an error on the order of 10^{-7}mm was reached. Unfortunately this accuracy is only theoretically achievable (in relation to the harmonics and the mean radius reported) because the performance was carried on ideal condition i.e. without errors on the measures and without motion of the centre. The reconstruction error reported is the result of the approximation introduced in the formulation and of the numerical errors related to the discrete Fourier transform computation.

The first simulation reveal a key point of the 3P method: the choice of the sensor's positioning angles. In Figure 89 the reconstruction results of a 500 mm circle with the first five harmonics 0.01 mm are reported. Both in the radius and in the motion reconstruction the error is huge, in the plot axes we can see an order of 10^{11}mm. This is due to the particular tern of sensor angle used, in this case [0 54 159] deg.

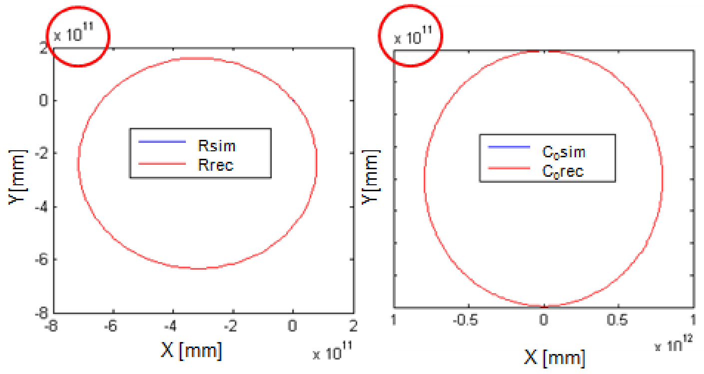

Figure 89: Radius and motion reconstruction - effects of probe angle

Analyzing the reconstruction formulas in harmonics domain eq.[12.1.6], it is noticeable that the denominator depends only on the harmonics and on the tern of angles:

$$Den = \sin\left(\alpha_2\text{-}\alpha_3\right) + \sin\left(\alpha_3\right)\cdot e^{-I\cdot\frac{2\pi\cdot a}{N}\cdot\alpha_2} - \sin\left(\alpha_2\right)\cdot e^{-I\cdot\frac{2\pi\cdot a}{N}\cdot\alpha_3} \quad [13.1.1]$$

Obviously, when this denominator is null the reconstruction is precluded and, as common in numerical computation, when this denominator is small enough numeric error explode. The denominator of the utilized tern is plotted to the harmonics:

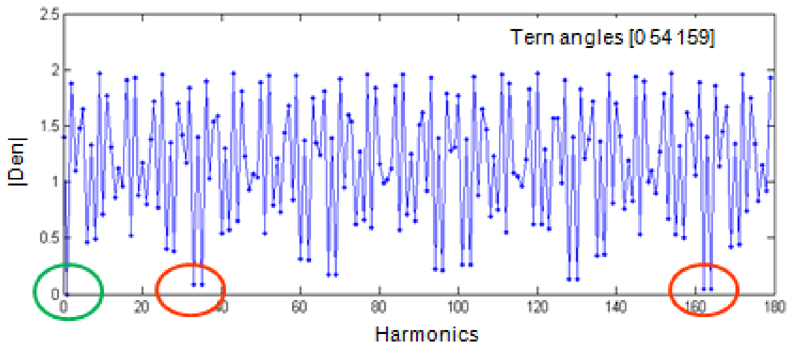

Figure 90: Denominator of reconstruction formulas to harmonics - [0 54 159]

It is clearly visible that this choice of angles determines the denominator to fall down in the harmonics evidenced with red circle. The denominator in the first frequency, in green circle, it is always null, for all angle terns. Fortunately this is not a problem because the first harmonic of the radius is definitely null for definition and thus the first harmonic of the measures can be easily decompose in the two components of the centre motion.

For the above reason the choice of the tern of position angles of the centre is fundamental for a good reconstruction. An optimization of these parameters was carried out during the research activity based on a cost function on the denominator values weighted on the harmonic. The resulting bests choice was tested in Monte Carlo simulation in order to assess the robustness to positioning errors and the others disturbance. Moreover this aspect of the reconstruction method suggests the introduction of another probe in the section (4 point method) in order to utilize the best of the four resulting terns for each harmonic. This solution, investigated in the research activity, leads to a noticeable improvement of the accuracy on the reconstruction. However this part is not reported in this dissertation because the modelling and simulation activity is the key point of interest (that can be carried out with the three point method without loss in importance) and for reason of industrial secrets agreement.

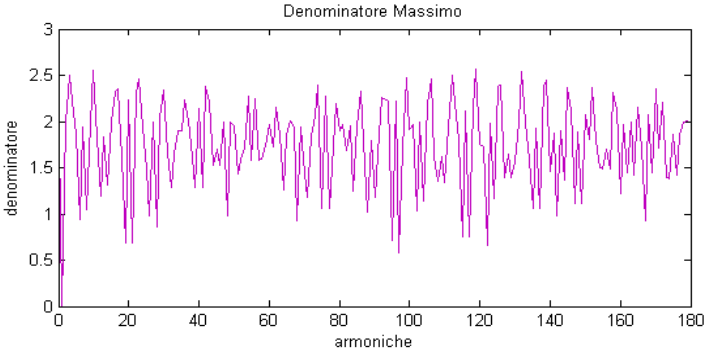

Figure 91: Example of denominator matching result on a four point method

With the aim of demonstrate the importance of the modelling of positioning error of the probes to achieving a meaningful performance evaluation of a multi point reconstruction method a brief simulation campaign are carried out.

To avoid the influence of the shape and the motion chosen for the simulation these features are generated pseudo randomly, practically a Monte Carlo method on the measurand is implemented. The measurement system model developed in this work is well suited to this kind of simulation because of the low computational cost of the model and because the parameters of interest can be first generated by an dedicated extraction algorithm an then can be easily introduced in the model.

These first simulations are carried out in two-dimensional situation for simplicity, therefore positioning errors relating to the z-dimension are not involved and the motion is considered only in the cross section plane (as if the two supports and necks are identical). The Monte Carlo method, as described in the supplement of the GUM (ISO - GUM, 1995), (GUM, 2004) is schematized on Figure 92.

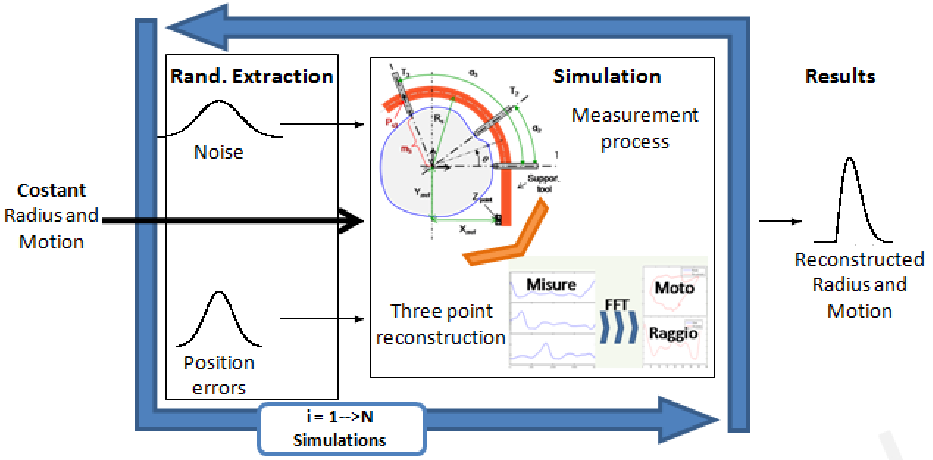

Figure 92: Monte Carlo method for uncertainty calculation - Original

The measurand in this case is the section and its axis motion and has to be maintained constant during the *N* simulations. The others disturbances under investigation has to be characterized by theirs probability distribution. At each simulation a value of each input quantity is extracted according to its probability density function and the simulation is performed. The results, in this case the reconstructed values, represent an estimation of the same model (the radius and motion assigned) and so the distribution of the output can be evaluated.

The procedure proposed here is slightly different and is explained in Figure 93.

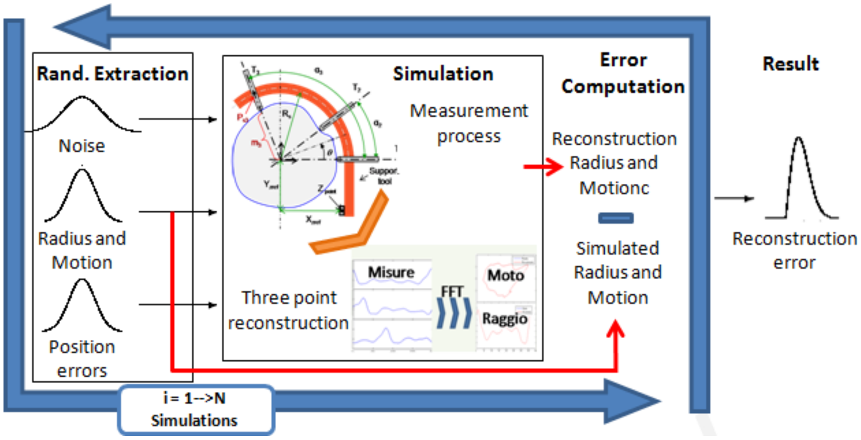

Figure 93: Monte Carlo method modified for random measurand

In the modified version also the radius and the motion of the section is randomly generate according to an assigned distribution. In particular the distributions assigned to the harmonics are uniform in a range plausible for our application. The phases of the harmonics are also uniformly distributed whereas the motion derives from the distributions of neck's harmonics and axis deviation. These parameters are also modelled as uniformly distributed.

For each simulation, these pseudo-random drawn shape and motion, along with the position errors and the other disturbance (pseudo random generated as in classic Monte Carlo), are used and the radius and motion are reconstructed. The new output variable is not the reconstructed values that obviously change for each simulation, but the reconstruction errors. These reconstruction errors are computed comparing the simulated values of radius and motion. Finally the statics of errors are analyzed for the whole Monte Carlo session. The considered values for the reconstruction error can be the maximum value for each simulation, the mean value (or mean of square) or the whole set of errors. In what follows the maximum errors are taken as characteristic values and the Monte Carlo session involve 2000 simulation. The results of three meaningful modified Monte Carlo simulations are reported.

13.1.1 2D Monte Carlo – Ideal condition

The mean radius of the cross section is fixed to 500mm, the position and inclination error of the probes are zero for all the simulations. Only the motion and the profile are modelled and are drawn from uniform distribution. Considering the 2D situation, the z dependency is suppressed and hence only the values A_{ra} and DD_{ra} are used for the description of the section, the axis is considered straight and so the motion is fully determined by the neck's profile. The harmonics of the necks, as well as their phases, are equal on front and back necks in order to determine only translation in X_0Y_0 plane while rotating around Z_0.

The ranges values of the uniform distribution for the harmonics, the phases of both section and necks are as follows. Lengths are in μm and angles in deg°.

A_{ra}	0÷0	0÷4	0÷4	0÷2	0÷2	0÷1.5	0÷1.5	0÷1.5	0÷1	0÷1
DD_{ra}	0÷2Pi	0÷2Pi	0÷2Pi	0÷2Pi	0÷2Pi	0÷2Pi	0÷2Pi	0÷2Pi	0÷2Pi	0÷2Pi
Ra_{Front}	0	0÷10	0÷4	0÷4	0÷2	0÷2	0÷2	0÷2	0÷1.5	0÷1.5
Ra_{back}	0	0÷10	0÷4	0÷4	0÷2	0÷2	0÷2	0÷2	0÷1.5	0÷1.5
ϕa_{Front}	0÷2Pi	0÷2Pi	0÷2Pi	0÷2Pi	0÷2Pi	0÷2Pi	0÷2Pi	0÷2Pi	0÷2Pi	0÷2Pi
Φa_{back}	0÷2Pi	0÷2Pi	0÷2Pi	0÷2Pi	0÷2Pi	0÷2Pi	0÷2Pi	0÷2Pi	0÷2Pi	0÷2Pi

R_n = 500mm; $R0_{Front}$ = 200mm; $R0_{Back}$ = 200mm;

In Figure 94 the histograms of the maximum reconstruction errors for each single simulation are reported both for radius and motion. There are only the maximum values for each simulation, this is the reason why there are no values near zero. As expected the reconstruction is accurate both for radius and for motion. The error is due only to the numerical FFT computation and to the approximation in eq. [12.1.1]

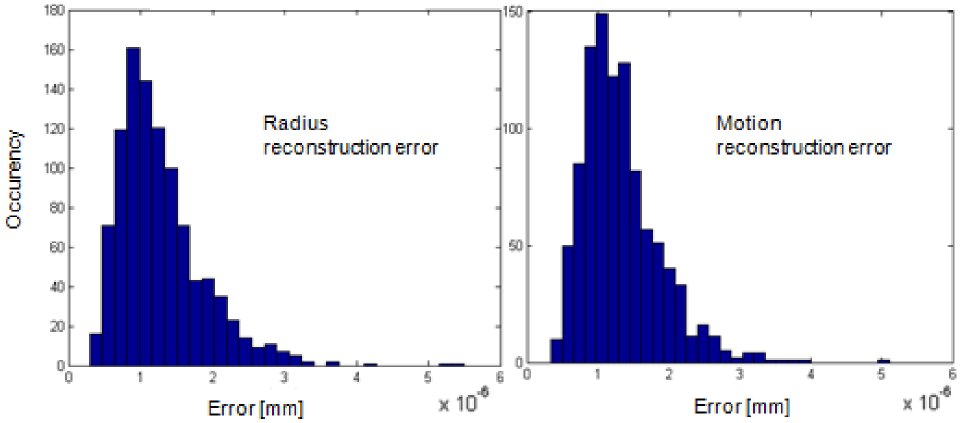

Figure 94: Histogram of the maximum reconstruction error - ideal condition

13.1.2 2D Monte Carlo – Sensors position error

In this simulation the position errors $E_{\alpha i}$ of the sensors over the portal are introduced. The shape and the motion of the section are modelled as in the previous Monte Carlo simulation whereas the position errors are modelled with a normal distribution with zero mean and a standard deviation of 1 deg°. The result is in Figure 95.

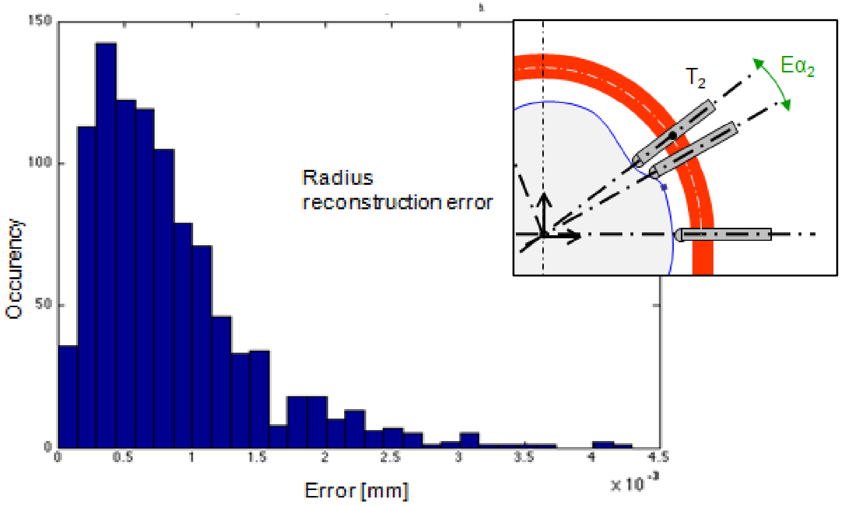

Figure 95: Histogram of the maximum reconstruction error – position error

The maximum error is frequently less than 1µm that, considering the harmonics of the order of some (0-4) micron it is not negligible and thus, the modelling of this parameter on measurement system simulations is of real concern for a good performance analysis of the reconstruction method. The same error result in the motion error (not reported for brevity).

13.1.3 2D Monte Carlo – Misalignment error

In this simulation the misalignment errors Exy_i of the probes are introduced. The shape and the motion of the section are modelled as in the previous Monte Carlo simulation whereas the position errors are modelled with a normal distribution with zero mean and a standard deviation of 0.2 deg°. The result is in Figure 96. The maximum errors are less than 0.5 micron on the radius reconstruction leading to the conclusion that this alignment error has a perceptible effect on the reconstruction but it not so restrictive as others. Note that the standard deviation on the parameter is smaller than for the positioning error where a linear small position error on the support can lead to a conspicuous error in position angle.

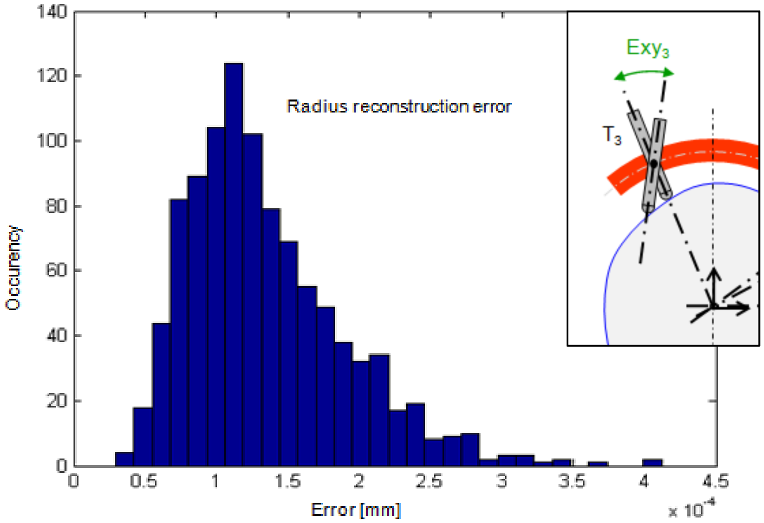

Figure 96: Histogram of the maximum reconstruction error – misalignment error

Obviously, these conclusions are related to the simulated situation with this diameter, this measurement system parameters and the errors distribution employed. This is the reason why, at a first attempt, all the effect of both motion and position errors on the shape reconstruction shall be investigated.

13.1.4 2D Monte Carlo – Offset error

The offset error directly affects the measure by adding a constant value for each measure of a single sensor. It is in practice an error on the zeroing of the sensor axis. It is modelled with a normal distribution with zero mean and a standard deviation of 1mm. The result is in Figure 96. The maximum errors in radius reconstruction are of the order of millimetres that are clearly unacceptable with harmonics of the order of few microns. Analysing the reconstructed and simulated radius the plot on the right of Figure 97 describes an error of more than 1 mm on the mean radius reconstruction. Hence, the error shown in the histogram is mainly on the mean value of the radius whereas the error on the successive harmonics is of the order of micron. In a wide range of application the precision on the mean radius reconstruction is of less interest respect to harmonics reconstruction. However, the offset error is an important parameter to be modelled also for harmonics.

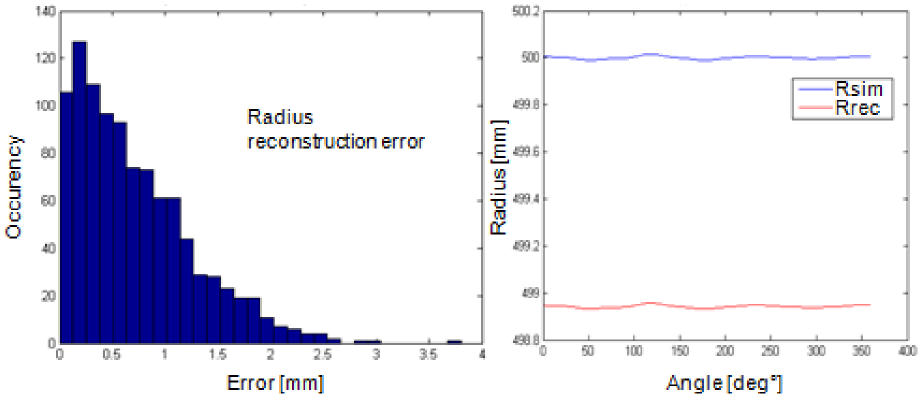

Figure 97: Histogram of the maximum reconstruction error – offset

13.1.5 2D Monte Carlo – Noise on measurement

The displacement sensor, the electronic equipment and the acquisition system are affected by noise as is common in measurement system. This noise appears as fluctuations on the measures that not represent a real variation on the measured distance. The noise is modelled as a white noise (zero mean and constant spectrum) whit a standard deviation of 1μm. The result is in Figure 98.

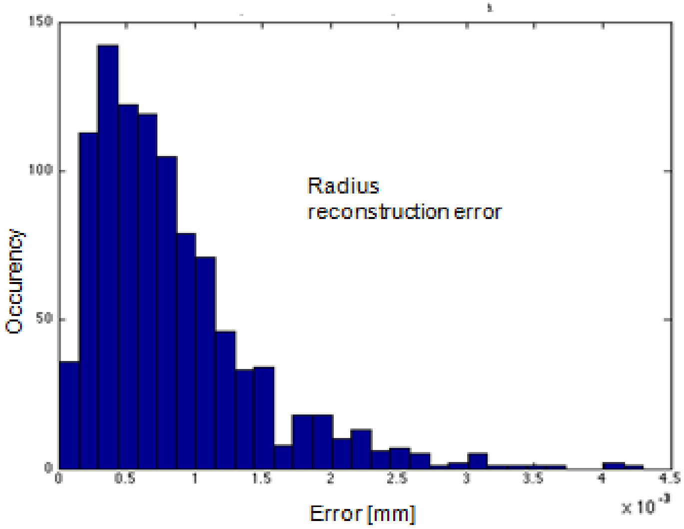

Figure 98: Histogram of the maximum reconstruction error – white noise

The noise on the measures, if not opportunely filtered, introduces an error of several micron particularly on the harmonics. The use of discrete transform, allow us to simply ignore the higher frequencies (in that case the angular frequencies) operating like a digital low-pass filter on the reconstruction algorithm. However, it is worth to note that the error on the measures, always present in real measures, is an important disturbance that has to be modelled.

In conclusion of this campaign of simulations the importance of the modelling of 2D mounting errors and measure noise is evident. In particular, if the noise, the misalignment and the positioning errors affects principally the harmonics, the offset on the measure strongly affect the mean radius (and motion) reconstruction.

13.2 Three point method on the cylinder simulations in 3D model

First of all the three point method is applied to the measure of the simulation5 showed in section 11.5. The reconstruction is performed in the central section of the cylinder and the reconstruction errors are reported in Figure 99. In this simulation all the position and alignment errors of the probes are modelled and the irregular motion over supports is implemented. The reconstruction errors are computed only on the radius for brevity and are plotted to the angle of rotation. It is worth to remember that the harmonics modelled are of the order of 0.1 mm an less whereas the mean radius is 400 mm.

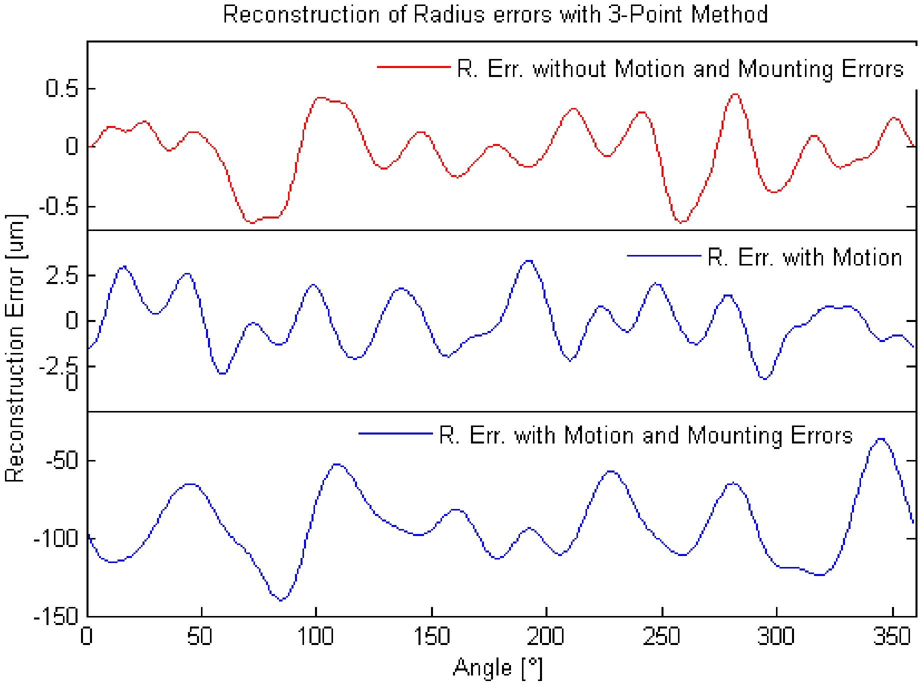

Figure 99: Reconstruction errors on radius from 3D simulated measures

In the first graph the reconstruction errors with ideal condition are reported, the error due to approximation and numeric FFT computation determines an error that is of the order of 0.5 micron. The second graph shows the errors with only the irregular motion implemented. The error reaches a spread of 2.5 micron because the irregular motion, even though is separated by the three point method, causes the sensors to measure on different sections. The last graph show the results obtained by utilizing the measures coming for the complete simulation5. In this simulation all the disturbance are modelled (except offset and white noise) and a systematic effect on the radius errors can be seen. The mean error is about 100 micron whereas a spread of 50 micron is reached. The mean error (that is an error on the mean radius evaluation) is mainly due to the inclinations of the support that lead to an offset on the measures that is almost constant on the section and varies longitudinally along the cylinder as posted in section 11.5. The spread is due to the interaction of the irregular motion of the cylinder with all the position and alignment errors and the inclination errors. The three dimensional modelling of the whole measurement system turns out to be fundamental if the performance of a reconstruction method would be investigated.

Naturally, with the aim of investigating the effect of each parameter on the reconstruction performance, a great number of simulations are required. Monte Carlo simulations can be easily implemented in this framework due to the parametric form of the model and velocity of execution.

In Figure 100 a scheme of Monte Carlo test structure suitable for uncertainties propagation assessment is reported. The measurand (i.e. the surface of the cylinder) and its necks are modelled by casually extracting the parameters described in chapter 9 from assigned distribution. This operation is performed once with the aim of generate a pseudo-casual shape and motion. The measurand and motion obtained are used by the Monte Carlo simulations in which the disturbances (i.e. misalignment errors, position errors, inclinations of the support and offsets) are randomly extracted from the assigned distribution for each single measurement simulation *i*. A white noise is added to the measures obtained for each simulation and then the reconstruction by three point method is performed. The reconstructed radius and the simulated radius are compared for each section, each angle and obviously, for each iteration giving the errors distribution. Depending on the needs, the mean or maximum errors over the section for each measuring section or else over each rotation angle are of interest and can be easily computed in the uncertainty estimation frame.

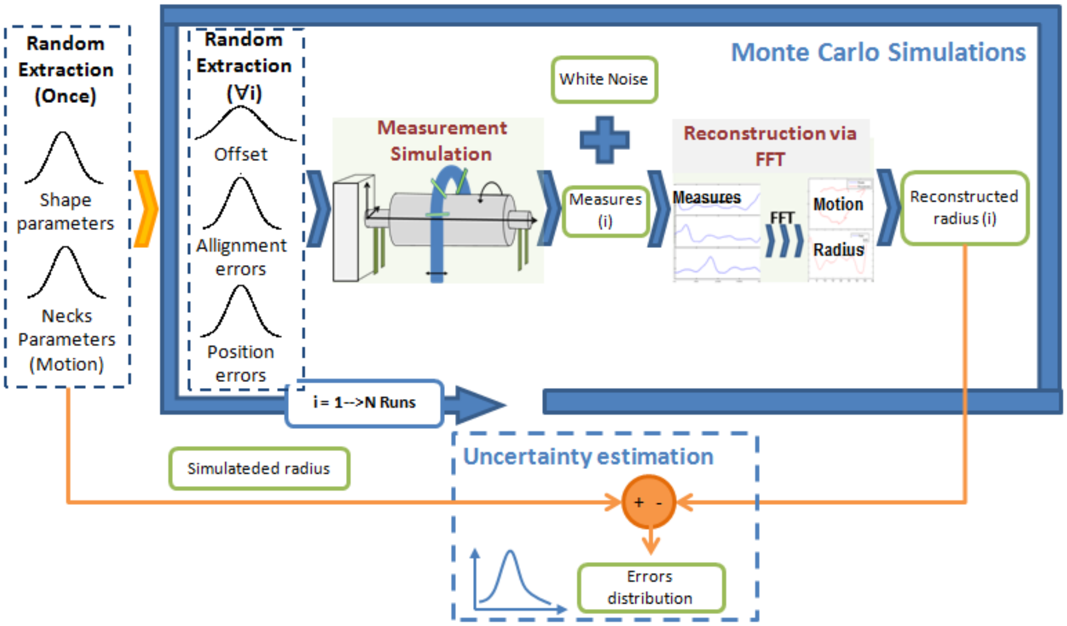

Figure 100: Layout of 3D Monte Carlo simulations for uncertainty estimation

In what follows some meaningful results of the application of this simulations architecture are reported and discussed.

Firstly the system in ideal conditions is simulated for comparison. In this simulation only the shape and the motion are implemented and casually extracted (once) from uniform distributions. Obviously, only one simulation is performed because the parameters varied in Monte Carlo are always zero. The main parameters utilized in the simulation are as follows:

Ara	0	6.2	9.4	6.9	4.5	5.6	6.3	4.7	3.7	3.5	1	0.6	0.2	1	0.6	µm
RaFront	0	9	3.1	9.6	2.6	µm		Raback		0	7.4	4.1	6.9	3.8	µm	
ϕaFront	0	3.3	3.5	2.6	4.5	rad		Φaback		0	3.7	5.4	2.8	4.1	rad	

$R_n = 400mm$; $L_{cil} = 1m$; $A_{r0} = 51\ \mu m$; $B_{r0} = 0.2$; $C_{r0} = -\pi/2$; $M = 21\ \mu m$;
$R0_{Front} = R0_{Back} = 200mm$; $\alpha_{1,2,3} = [\ 0° \ 53° \ 159°\ ]$;

The histogram of the reconstruction errors for 100 section and 360 degrees is shown in Figure 101. Differently from the 2D histogram there are all the errors not only the maximum value of each section. The irregular motion itself introduces an error with a standard deviation of $3x10^{-5}$mm (the approximation and numerical error in this case it's of the order of 10^{-7} mm. The mean of the errors is two orders of magnitude less than the standard deviation and hence the systematic error is negligible. Intuitively, the irregular motion itself forces the sensors to measure a section that is slightly different from the ideal one because of the inclination of the cylinder, obviously if the cylinder is very long this effect is small and only the translation on XY is important.

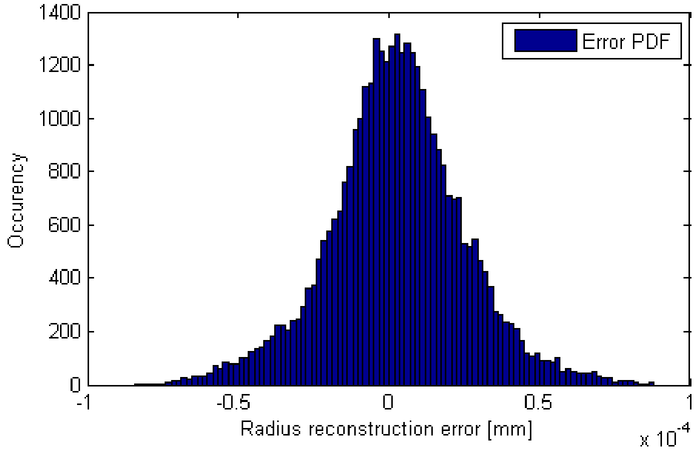

Figure 101: Ideal conditions - errors histogram

The next simulation is aimed to show the effect of the position and alignment errors of the sensors. The cylinder is modelled starting from the same parameters distribution of the previous simulation whereas the motion is ideal (only rotation around Z). The position and inclination errors are generated for each simulation according to normal distributions with zero mean and the standard deviation specified as follows:

A_{ra}	0	6.3	0.9	2.7	5.4	9.5	4.8	0.7	4.8	4.7	0.4	0.8	0.1	0.4	0.9	µm

$R_n = 400$ mm; $L_{cil} = 1$ m; $A_{r0} = 8.1$ µm; $B_{r0} = 9$; $C_{r0} = \pi/6$; $M = 0$ µm;

$R0_{Front} = R0_{Back} = 200$ mm; $\alpha_{1,2,3} = [\ 0° \ 53° \ 159°\ ]$; $N_{simulations} = 1000$;

$\sigma E\alpha_{1,2,3} = 0.02°$; $\sigma Ez_{1,2,3} = 0.02$ mm

$\sigma Exy_{1,2,3} = 0.02°$; $\sigma Exz_{1,2,3} = 0.02°$; $\sigma offset = 0.002$ mm;

The results, in term of errors on the radius reconstruction, are depicted by the histogram in Figure 102. The distribution appears scattered and quite dispersed. The maximum error reach about 4 micron. Zooming on a portion of the histogram the reason of this spread is deductible. The position errors, and particularly the offset, different for each single simulation. This fact determines the presence of several distributions with different mean that generate the discussed histogram.

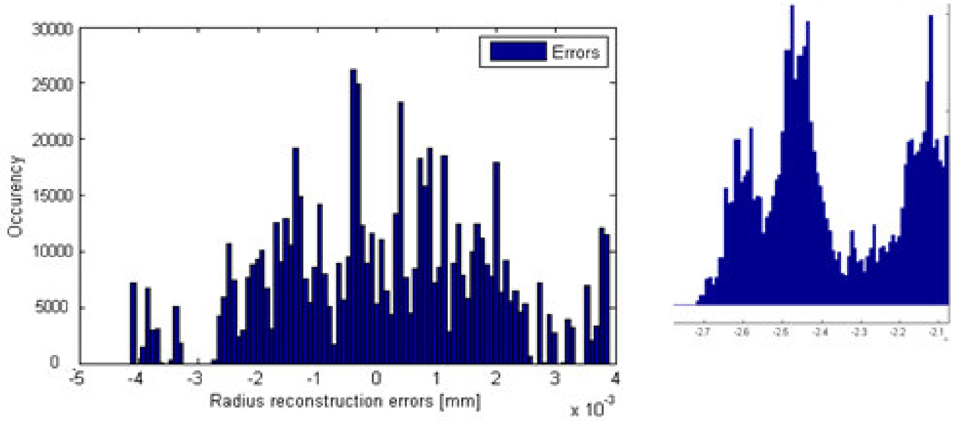

Figure 102: 3D position and alignment errors – errors histogram

Finally, a conclusive simulation with almost all the features implementable in the model is reported. The cylinder and motion are extracted as in the ideal simulation. The position and alignment errors are randomly generated for each simulation according to normal distribution with the reported standard deviation. Also the white noise is added over the measures in this simulation. The parameters imposed are as follows:

A_{ra}	0	8.2	8.7	0.8	4	2.6	4	2.2	4.6	0.9	0.3	0.1	0.1	0.9	0.6	µm
Ra_{Front}	0	9.2	4.3	1.8	9	µm		Ra_{back}		0	4.4	1.1	2.6	4.1	µm	
ϕa_{Front}	0	1.64	3.78	4.46	1.39	rad		Φa_{back}		0	1.86	2.00	2.66	3.19	rad	

R_n = 400mm; L_{cil} = 1m; A_{r0} = 1.1 µm; B_{r0} = 9.6; $C_{r0} = \pi/5$; M = 1.9 µm;

$R0_{Front}$=$R0_{Back}$ = 200mm; $\alpha_{1,2,3}$ = [0° 53° 159°]; $N_{simulations}$ = 1000;

$\sigma E\alpha_{1,2,3}$ =0.02° ; $\sigma Ez_{1,2,3}$ = 0.02 mm; σExz_s = 0.01°; σEyz_s = 0.01°;

$\sigma Exy_{1,2,3}$ = 0.02°; $\sigma Exz_{1,2,3}$ = 0.02°; σoffset = 0.002mm; σ_{noise}= 2 µm.

In Figure 103 the histogram of all the errors reached on each section, on each scansion angle and from each simulation is reported. The distribution is almost symmetrical with a standard deviation of 50 µm and a mean value of less the 1 µm. This results for the combination of all the disturbance, generated pseudo-randomly in each run.

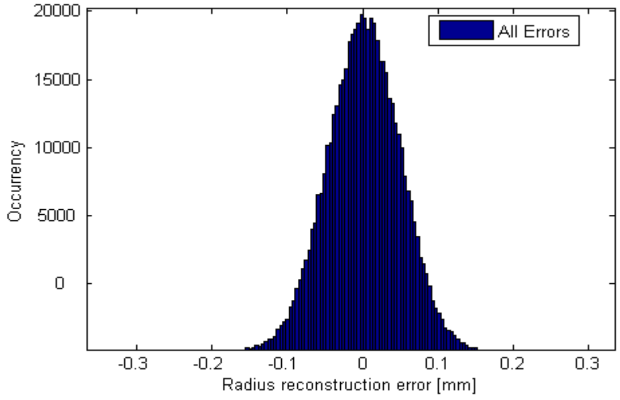

Figure 103: Final simulation - errors histogram

If the histogram on the single run is computed the situation is more clear and a systematic error is observed. In Figure 104 the histogram of the errors for run100 and run900 show a systematic error. The presence of offset on the measures, misalignment of the support seems to be the most responsible of this error whereas the spread is particularly related to the motion, the position and alignment errors of the probes and, obviously, to the white noise on the measures.

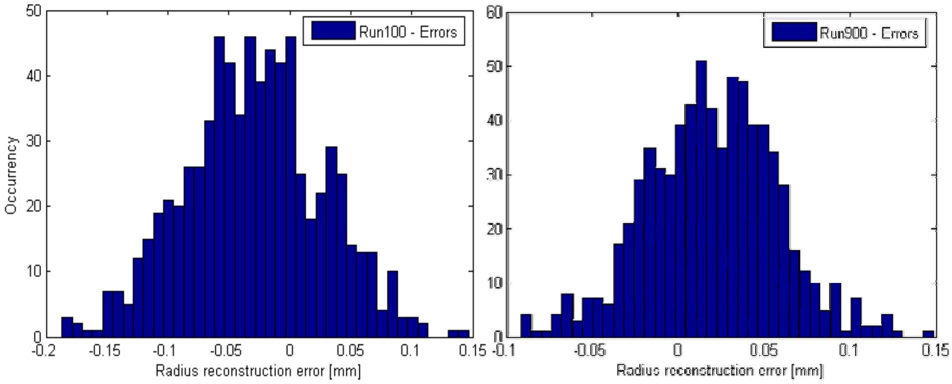

Figure 104: Final simulation - errors histogram for run 100 and run 900

After these simulation on the three dimensional model of the measurement system coupled with the three point method the importance of a complete modelling of the three dimensional features of the measurement system, as well as mounting errors of the probes and noise on the measure, is demonstrated. The understanding of the mutual interaction among these effects or the influence of these effects in function of the geometrical parameters requires focused campaigns of simulations that are not the aim of this dissertation. Nevertheless it is demonstrated that the developed model can be easily suited for Monte Carlo or similar simulations in which all the parameters that control the model can be drawn at random from the respective hypotised distribution.

14 CONCLUSIONS – PART 2

In this second part of the work, the numerical modelling of systems for rotating cylinders measurement has been analyzed. After a brief introduction on the problem of the surface measurement of cylindrical components and the state of the art illustration, the development of a new numerical model was performed.

The modelling, as explained in section 9, started with the main actors of the measurement process: the shape and axis of the cylinder. A mathematical parametric model of the shape and the axis of a generic cylinder had been realized. This parametric model gives the possibility to easily model a wide range of cylinders with a limited number of parameters. The key points of this modelling are the use of discrete Fourier series for the description of the cylinder cross section and the implementation of appropriate continuous function to model the variation of the cross section along the cylinder.

The modelling of the multi point measurement system was then carried out by the description of both the motion of the cylinder and the sensors position. The cylinder motion was modelled on a classical grinding machine for big cylinder where the rotation is feed by a spindle and four plain columns supports the cylinder on his necks. For these reason first, the necks cross section were modelled and then an algorithm was developed to reconstruct the position of the centre of each neck while the cylinder is rotating. In particular the contact points between the two necks and the four supports are individuated and from these the centres of the necks are easily derived. The positions of the necks fully determine the axis position of the cylinder respect to the fixed frame while the measurement process runs.

The sensor layout was defined by the kinematic of the measurement system taking in to account positioning errors, alignment errors and misalignments of the probe's support. Furthermore, the algorithm that computes the measure was explained, the main point of this algorithm is the 3-D recursive search of the contact point between sensor and surface of the moving cylinder by numerical methods.

Once the model was completely explained, some simulations were showed demonstrating the importance of modelling both the motion, the kinematics of the support tool and the mounting errors of the probes. Comparing the measures obtained with and without these three dimensional aspects clearly shows that conspicuous errors are encountered, even with small deviations from ideal case. The presence of misalignment errors of the support on the order of 1 degree led to differences on the measure of about ten times the value of the harmonics modelled respect to the ideal situation. The position errors of the probes led to differences of about the 30% of the harmonics whereas the motion, with the parameters used in that simulation determined differences of about 8 times the harmonics. These results well demonstrate the importance of a complete modelling of the three dimensional effects.

Moreover a three point reconstruction method was implemented and some improvements were investigated like the sensor angle layout optimization and the introduction of the fourth sensor.

The measurement system model was then utilized to evaluate the performance of the reconstruction algorithm in presence of the various disturbs. Firstly some two dimensional investigations through modified Monte Carlo simulations were carried out. The effect of sensors positioning and inclination error in the cross-sectional plane were introduced showing that errors of the order of the simulated harmonics can be reached in the reconstruction of the radius. The white noise on the measures and a zeroing error of the sensors are also simulated and the importance of consider these aspects was demonstrated showing their great influence on the reconstruction errors.

Finally the Monte Carlo simulations were carried out using the model in three dimensional configuration. The structure of the MC simulations was explained and the suitability of the model in Monte Carlo and similar design of simulation was evidenced. The velocity of execution and the parametric nature of the model allow to easily performing this kind of procedures. The three MC simulations demonstrated once again that the positioning errors, the irregular motion and the noise on the measures have a great influence on the reconstruction performance.

In conclusion the importance of model the three dimensional aspects of the measurement system is demonstrated as well as the quality of the model developed.

15 CONCLUSIONS – GENERAL

The modelling process has been successfully applied to both the application studied. The research activity on the wind energy converters led to the development of a model suitable to correct the power curves of wind turbine to take into account the effect of the rapid wind speed fluctuation due to the turbulence always present in natural wind. The model, along with the procedure to extract the parameter (i.e. the steady power curve) was validated on experimental data from the test site of Trento giving positive results.

The research activity on cylinder measurement led to the development of a parametric numerical model of a three point measurement system. Such model considers the irregular motion of the cylinder during the measurement process and the alignment and position errors of the sensors. The cylinder and the other aspects of the model are described by a set of parameters. The model was employed to demonstrate the effect of the 3D motion and position errors on the measures. Furthermore a three point reconstruction method was implemented in the model and some Monte Carlo simulations are performed for double purpose: to show the importance of a complete modellation of the 3D aspects of the system and to illustrate de suitability of the parametric model in Monte Carlo simulation.

16 BIBLIOGRAPHY

1. Adamczak, S., Janecki, D. & Stepien, K., 2006. An analysis of errors of v-block cylindricity measurement with regard to the method parameters. In *XVIII IMEKO world congress Metrology for a Sustainable Development*. Rio de Janeiro, Brazil, 2006.
2. Albers, A., Hinsch, C. & Dewi, 1996. Influence of Different Meteorological Conditions on the Power Performance of Large WEC's. *DEWI Magazin Nr. 9*, pp.41-49.
3. Alberts, A., Jakobi, T., Rohden, R. & Stoltenjohannes, J., 2007. Influence of metereologica variables on measuredi in wind turbines power curves. pp.1-7.
4. Antoniou, I. et al., 2007. Influence of wind characteristics on turbine performance. In *European Wind*., 2007.
5. Aoki, Y..O.S., 1966. On a new method of roundness measurement based on the three point method. *ournal fo JSPE*, 32(12), pp.831-36.
6. Avgoustinov, N., 2007. *Modelling in mechanical engineering and mechatronics*. London: Springer.
7. Avriel, M. & Wilde, D.J., 1966. Optimality proof for the symmetric Fibonacci search tecnique. *Fibonacci quarterly*, pp.265-69.
8. Battisti, L..F.R..D.S.S..G.A., 2005. Influence of wind turbine's type and size on anti-icing thermal power requirement. In *EUROMECH 2005 Wind Energy Colloquium*. Oldenburd, Germany., 2005.
9. Battisti, L., 2008. *Ice prevention systems design*. Classes notes - Master on Wind energy. Copenhagen: DTU.
10. Battisti, L., Miori, G., Zanne, L. & Dell'Anna, S., 2009. Effetto dei fattori che influenzano la costruzione della curva di potenza di turbine eoliche. In *64° Congresso nazionale A.T.I., Associazione Termotecnica Italiana*. L'Aquila, 2009.

11. Battisti, L., Miori, G., Zanne, L. & Dell'Anna, S., 2010. Effetti dinamici nella costruzione sperimentale della curva di potenza per turbine eoliche di piccola taglia. In *65° Congresso Nazionale A.T.I.* Cagliari, 2010.
12. Bottcher, F., Barth, S. & Peinke, J., 2007. Small and Large Scale Fluctuations in Atmospheric. *Stoch. Environ. Res. Ris. Assess.*, (21), pp.299-308.
13. Burton, T., Sharpe, D., Jenkins, N. & Bossanyi, E., 2002. *Wind energy handbook*. Wiley & Sons.
14. Busch, N.E. & Kristensen, L., 1976. Cup Anemometer Overspeeding. *Journal of applied meteorology*, Dec.
15. Cabezon, D., Marti, I., Jesus San Isidro, M. & Jesus San Isidro, I., 2004. Comparison of methods for power curves modeling. In *Global wind power 2004*. Chicago, Illinois (USA), 2004.
16. Chin, D.H..Y.M.C..S.S.B., 2005. Roundness modelling in BTA deep hole drilling. *Precision eng.*, (29), pp.176-88.
17. Christensen, C.J. et al., 1986. Accuracy of Power Curve Measurements. *Riso National Laboratory, ECN*, pp.1-146.
18. D.Bianchi, F., De Battista, H. & J. Mantz, R., 2006. *Wind Turbine Control Systems Principles,Modelling and Gain Scheduling Design*. Lavoisier.
19. De Cecco, M. et al., 2010. A Unified Framework for Uncertainty, Compatibility Analysis, and Data Fusion for Multi-Stereo 3-D Shape Estimation. *IEEE Trans. on instrumentation and measurement*, VOL. 59, pp.2834-42.
20. De Franceschi, M., 2004. *Investigation of Atmospheric Boundary Layer Dynamics in Alpine Valleys*. Ph.D. Thesis. Trento.
21. de Vries, O., 1979. Fluid Dynamic Aspects of Wind Energy Conversion. *AGARD Fluid Dynamic Aspects of Wind Energy Conversion*, (No. 243).
22. Elliot, D.L., Cadogan, J. & B., 1990. Effects of wind shear and turbulence on wind turbine power curve. In *European Community Wind Energy Conference and Exhibition*. Madrid, 1990.

23. Endo, K..G.W..K.S., 2003. A new multi probe arrangement for surface profile measurement of cylinders. *JSME*, 46(4), pp.1531-37.
24. Frandsen, S. et al., 2000. Redefinition Power Curve for More Accurate Performance Assessment of Wind Farms. *Wind Energy*, pp.81-111.
25. Fung, E. & Yang, S.M., 2001. A New Method for Roundness Control in Taper Turning Using FCC Techniques. *Journal of Manufacturing Science and Engineering*, pp.567-75.
26. Gao, W. & Kiyono, S., 1997. On-machine roundness measurement of cylindrical workpieces by the combined three-point method. *Measurement Vol. 21, No. 4, Elsevier*, pp.147-56.
27. Gao, W., Kiyono, S. & Nomura, T., 1996. A new multiprobe method of roundness measurements. *Precision Engineering 19*, pp.37-45.
28. Gao, W., Kiyono, S. & Sugawara, T., 1997. High-accuracy roundness measurement by a new error separation method. *Precision Engineering 21*, pp.123-33.
29. Gapinski, M..G.M..R.M., 2006. The accuracy analysis of the roundness measurement with coordinate measurement machines. In *XVIII IMEKO world congress*. Rio de Janeiro, Brazil., 2006.
30. GL Wind, 2005. *Guideline for the Certification of Wind Turbines, Part 1.* par. 4.4.5, pp.4-26. GL Wind.
31. Gottschall, J., 2009. *Modelling the variability of complex systems by means of Langevin processes On the application of a dynamical approach to experimental data*. Oldenburg: Fakult at f ur Mathematik und Naturwissenschaften der Carl von Ossietzky Universit at Oldenburg.
32. Gottschall, J. & Peinke, J., 2008. How to improve the estimation of power curves for wind turbines. *ENVIRONMENTAL RESEARCH LETTERS*, pp.1-7.
33. GUM, 2004. Supplemento1 - Numerical Methods for the Propagation of Distributions.
34. Hannah, P., 1997. *Investigation of upflow on escarpments*. Harwell (UK): Energy Technology Support Unit (ETSU).

35. Hojstrup, J., 1999. Spectral coherence in wind turbine wakes. *Journal of Wind Engineering and Industrial Aerodynamics 80, Elsevier*, pp.137-46.
36. IEC 61400-1, 2005. Wind Turbines - Part 1: Design requirements. Augustus.
37. IEC 61400-12-1, 2005. Wind Turbines - Part 12-1: Power performance measurement of electricity producing wind turbines. December.
38. IEC 61400-2, 2006. Wind Turbines - Part 2: Design requirements for small wind turbines. March.
39. ISO - GUM, 1995. Guide to the expression of uncertainty in measurement.
40. ISO 4292-1985, 1985. *Methods for the assessment of departure from roundness - Measurement by two and three point methods.*
41. ISO/TS 12181-1:2003, 2003. *(GPS) Geometrical Product Specifications - Roundness- Part 1: Terms, definitions and parameters of roundness*.
42. ISO/TS 15530-4:2008, 2008. *(GPS) Geometrical product specifications- Coordinate measuring machine (CMM): Tecnique for determining the uncertainty of measurement - Part4: Evaluating task specific measurement uncertainty using simulation.*
43. Jeong, G.B., Kim, D.H. & Jang, D.Y., 2005. Real time monitoring and diagnosis system development in turning through measuring a roundness error based on three-point method. *International Journal of Machine Tools & Manufacture 45, Elsevier*, p.1494–1503.
44. Kaimal, J.C.F.J.J., 1994. *Atmospheric boundary layer flows*. New York: Oxford university press.
45. Kaiser, K., Langreder, W., Hohlen, H. & Hojstrup, J., 2007. Turbulence correction for power curves. In Peinke, J., Schaumann, P. & Barth, S. *Wind Energy Proceedings of the Euromech Colloquium*. Springer. pp.159-62.
46. Kàrmàn, T.v., 1948. Progress in the statistichal teory of turbulence. *PHYSICS*, vol.34, pp.530-39.
47. Kato, H..Y.., 1990. Development of in situ measuring system of circularity in precision cylindrical grinding. *Bull of Japan Soc. Prec. Eng.*, 24, pp.130-35.

48. Li, C.J. & Li, S.Y., 1996. To improve workpiece roundness in precision diamond turning by in situ measurement and repetitive control. *Mechatronics* , Vol. 6(No. 5), pp.523-35.
49. MEASNET, 2009. *Evaluation of site specific wind conditions*. version 1.
50. Miller, N.W., Price, W.W. & Sanchez-Gasca, J.J., 2003. *Dynamic Modeling of GE 1.5 and 3.6 Wind Turbine-Generators*. Schenectady, NY.: GE-Power Systems Energy Consulting.
51. Miori, G. et al., 2009. A new method for Numerical Simulation of 3D motion effects on Motion and Roundness reconstruction based upon Parametric Mathematical Modelling. Palma de Mllorca, 2009.
52. Mitsui, K., 1982. Development of a new measuring method for spindle rotation accuracy estimation by three points method. In *Proc. 23 MTDR Conference*. Manchester, U.K., 1982.
53. Monin, A.S. & Obukhov, A.M., 1954. Basic laws of turbulent mixing in the surface layer of the atmosphere. *Tr. Akad. Nauk SSSR Geophiz. Inst. 24*, pp.163-87.
54. Muralikrishnan, B., Venkatachalam, S., Raja, J. & Malburg, M., 2005. A note on the three-point method for roundness measurement. *Precision Engineering 29 , Elsevier*, pp.257-60.
55. Negrente, S., 2009/2010. *Energia eolica nel paesaggio ad alta quota: un progetto per l'Altopiano della Paganella*. Thesis. Trento: Univesità degli Studi di Trento, Facoltà di Ingegneria.
56. Nyberg, T.R., 1993. *Dynamic macro topography of large slowly rotating cylinders*. no 108. Acta polytechnica scandinavica.
57. Okuyama, E., Nosaka, N. & Aoki, J., 2007. Radial motion measurement of a high-revolution spindle motor. *Measurement 40, Elsevier ed.*, pp.64-74.
58. Peinke, J. et al., 2008. *Turbulence a Challenging Issue for the Wind Energy Conversion*. Oldenburg, Germany: EWEC.
59. Peinke, J. et al., 2004. Turbulence, a challenging problem for wind energy. *Physica A 338, Elsevier*, pp.187-93.

60. Rareshide, E. et al., 2009. Effects of complex wind regimes on turbine performance. In *AWEA Windpower Conference*. Chicago, 2009.
61. Rosen, A. & Sheinman, Y., 1994. The average output power of a wind turbine in a turbulent wind. *J. Wind Eng. Ind. Aerodyn. 51, Elsevier*, pp.287-302.
62. Rozenn, W., S. Michael, C., Torben, L.J. & Uwe, P.S., 2010. *Simulation of shear and turbulence impact on wind turbine performance*. Roskilde, Denmark: Risø National Laboratory for Sustainable Energy Technical University of Denmark.
63. Saranyasoontorn, K. & Manuel, L., 2004. A Comparison of Standard Coherence Models for Inflow Field Measurements. *Journal of solar engineering trans. ASME*.
64. Schlez, W. & Infield, D., 1998. horizontal two point coherence for separations greater than measurement height. *Boundary-Layer Meteorology 87*, pp.459-80.
65. Sicot, C., Devinant, P. & Laver, T., 2006. Experimental Study of the Effect of Turbulence on Horizontal Axis Wind turbine aerodynamics. *WIND ENERGY*, pp.361-70.
66. Sumner, J. & Masson, C., 2006. Influence of Atmospheric Stability on Wind Turbine Power Performance Curves. *Journal of Solar Energy Engineering*, pp.531-38.
67. Sundar, R.M. & Sullivan, J.P., 1983. Performance of wind turbines in a turbulent atmosphere. *Solar Energy Vok 31, No. 6*, pp.pp. 567-575.
68. Tammelin, B..C.M..H.H..M.C..S.H., 2000. *Wind Energy in Cold Climate - WECO Final Report*. Helsinki, Finland. : Finnish Meteorological Institute.
69. Tindal, A. et al., 2008. Site specific adjustement to wind turbine power curves. In *AWEA Windpower Conference*. Houston, 2008.
70. Tindal, A. et al., June 2008. Site specific adjustments to wind turbine power curves. In *AWEA WINDPOWER Conference*. Houston, June 2008.

71. Tu, J.F., Bossmanns, B. & Hung, C.C., 1997. Modeling and error analysis for assessing spindle radial error motions. *Precision Engineering 21*, pp.90-101.
72. Van der Hoven, I., 1957. Power spectrum of horizontal wind speed in the frequency range from 0.0007 to 900 cycles per hour. *Journal of meteorology*, pp.160-64.
73. van Radecke, H., 2004. Turbulence Correction of Power Curves. *DEWI Magazin Nr. 24*, pp.56-62.
74. Wagner, R., 2010. *Accounting for the speed shear in wind turbine power performance measurement*. Roskilde; Denmark: RisøNational Laboratory for Sustainable Energy Technical University of Denmark.
75. Wagner, R. et al., 2009. The Influence of the Wind Speed Profile on Wind Turbine Performance Measurements. *Wind Energy*, pp.348-62.
76. Wharton, S. & Lundquist, J.K., 2010. *Atmospheric Stability Impacts on Power Curves of Tall Wind Turbines - An Analysis of a West Coast North American Wind Farm*. Livermore, CA: U.S. Department of Energy by Lawrence Livermore National Laboratory.
77. Yoshida, S., 2006. Superiority of downwind turbines in complex terrains. In *European Wind Energy Conference*. Athens, 2006.
78. Zhang, G.X., Zhang, Y.H., Zhang, S.M. & Li, Z., 1997. A Multipoint Method for Spindle Error Motion Measurement. *Annals of the ClRP Vol. 46*, pp.441-45.